

P. 128

SatCon Report R05-90

SBIR - 08.01-0540A  
release date - 5/02/92

MAGNETIC BEARINGS FOR A HIGH-PERFORMANCE  
OPTICAL DISK BUFFER

11-27

VOLUME I

by

Richard Hockney  
Karen Adler  
George Anastas, Jr.  
James Downer  
Frederick Flynn  
James Goldie  
Vijay Gondhalekar  
Timothy Hawkey  
Bruce Johnson

SatCon Technology Corporation  
12 Emily Street  
Cambridge, MA 02139

Contract No. NAS5-30309  
Final Report For Period May 1988 to April 1990

May 1990

Prepared for

Goddard Space Flight Center  
Greenbelt, Maryland 20771

(NASA-CR-190873) MAGNETIC BEARINGS  
FOR A HIGH-PERFORMANCE OPTICAL DISK  
BUFFER, VOLUME 1 Final Report, May  
1988 - Apr. 1990 (SatCon  
Technology Corp.) 128 p

N93-13706

Unclas

G3/37 0121193



FINAL REPORT

**MAGNETIC BEARINGS FOR A HIGH-PERFORMANCE  
OPTICAL DISK BUFFER**

by

Richard Hockney  
Karen Adler  
George Anastas, Jr.  
James Downer  
Frederick Flynn  
James Goldie  
Vijay Gondhalekar  
Timothy Hawkey  
Bruce Johnson

SatCon Technology Corporation  
12 Emily Street  
Cambridge, MA 02139

Approved by: *Richard Hockney*

Principal Investigator

Approved by: *David B. Eisenbaum*

President

Prepared for

Goddard Space Flight Center  
Greenbelt, Maryland 20771

Contract No. NAS5-30309

SBIR RIGHTS NOTICE (JUNE 1987)

These SBIR data are furnished with SBIR rights under Contract No. NAS5-30309. For a period of 2 years after acceptance of all items to be delivered under this contract, the Government agrees to use these data for Government purposes only, and they shall not be disclosed outside the Government (including disclosure for procurement purposes) during such period without permission of the Contractor, except that, subject to the foregoing use and disclosure prohibitions, such data may be disclosed for use by support Contractors. After the aforesaid 2-year period the Government has a royalty-free license to use, and to authorize others to use on its behalf, these data for Government purposes, but is relieved of all disclosure prohibitions and assumes no liability for unauthorized use of these data by third parties. This Notice shall be affixed to any reproductions of these data, in whole or in part.

## ACKNOWLEDGEMENT

The research presented in this final report was conducted by SatCon Technology Corporation under Phase II SBIR Contract NAS5-30309 with Goddard Space Flight Center for NASA. On behalf of SatCon, the authors would like to acknowledge the guidance provided by John Sudey and Mike Hagopian of Goddard SFC.

Any opinions, findings, and conclusions or recommendations expressed in this publication are those of the authors and do not necessarily reflect the views of NASA.

## PREFACE

The innovation investigated in this project was the application of magnetic bearing technology to the translator head of an optical-disk data storage device. Both the capability for space-based applications and improved performance are expected to result. The Phase I effort produced: (1) detailed specifications for both the translator-head and rotary-spindle bearings, (2) candidate hardware configurations for both bearings with detail definition for the translator head, (3) required characteristics for the magnetic bearing control loops, (4) position sensor selection, and (5) definition of the required electronic functions. The principal objective of Phase II was the design, fabrication, assembly, and test of the magnetic bearing system for the translator head. The scope of work included: (1) mechanical design of each of the required components, (2) electrical design of the required circuitry, (3) fabrication of the component parts and bread-board electronics, (4) generation of a test plan, and (5) integration of the prototype unit and performance testing.

The project has confirmed the applicability of magnetic bearing technology to suspension of the translator head of the optical disk device, and demonstrated the achievement of all performance objectives. The magnetic bearing control loops perform well, achieving 100 Hz nominal bandwidth with phase margins between 37 and 63 degrees. The worst-case position resolution is  $0.02 \mu$  in the displacement loops and  $1 \mu$  rad in the rotation loops. The system is very robust to shock disturbances, recovering smoothly even when collisions occur between the translator and frame. The unique start-up/shut-down circuit has proven very effective.

The potential problem which exists is the sensitivity of the Z position loop to disturbance from the linear motor. Lack of knowledge of the current waveform in the linear motor during a slew transient makes the severity of this problem impossible to assess.

The predominant shortcoming of the present system design is the gross mismatch between the center-of-mass of the translator and the center-of-effort of the magnetic actuators. This mismatch means that, in order to decouple the rotation loops from the displacement loops, some of the actuators must produce virtually no force. This restriction severely limits both the gain and the total force capability of the displacement loops.

The possibilities for future work which builds upon the success of this program are threefold. First, and most obvious, is the integration of this magnetic bearing retrofit into the existing optical disk system test-bed. The second possibility for future work is the application of this magnetic bearing

configuration to other linear motion applications such as interferometers, cryo-coolers, etc. Finally, while magnetic bearings have been developed by NASA for many various applications, no magnetic bearing has ever been flown in space by the United States. The availability of GAS-cans aboard the STS as a vehicle for space experimentation presents a unique opportunity to gain valuable experience and data from a magnetic bearing in the space environment.

## TABLE OF CONTENTS

1.	INTRODUCTION . . . . .	1-1
	1.1 Background . . . . .	1-1
	1.2 Organization . . . . .	1-1
2.	SYSTEM SPECIFICATIONS . . . . .	2-1
3.	MAGNETIC DESIGN . . . . .	3-1
	3.1 Design Constraints . . . . .	3-1
	3.2 Material Selection . . . . .	3-3
	3.3 Control Coil Design . . . . .	3-4
	3.3.1 Voltage Analysis . . . . .	3-4
	3.3.2 Thermal Analysis . . . . .	3-7
4	MECHANICAL DESIGN . . . . .	4-1
	4.1 Actuator Design . . . . .	4-1
	4.2 System Modifications . . . . .	4-1
	4.3 Holding Fixture . . . . .	4-5
5.	CONTROLLER DESIGN . . . . .	5-1
	5.1 Bearing Model . . . . .	5-1
	5.1.1 Magnetic Circuit Model . . . . .	5-2
	5.1.2 Nonlinear Force Model . . . . .	5-7
	5.1.3 Linear Force Model . . . . .	5-8
	5.1.4 Eddy Current Model . . . . .	5-9
	5.1.5 Amplifier Model . . . . .	5-9
	5.1.6 Sensor Model . . . . .	5-9
	5.1.7 Disturbance Model . . . . .	5-10
	5.2 Linear Design and Analysis . . . . .	5-10
	5.2.1 Compensator Design . . . . .	5-12
	5.3 Non-Linear Dynamic Simulation . . . . .	5-16
	5.4 Start-Up/Shut-Down Procedure . . . . .	5-18
6.	POSITION SENSOR . . . . .	6-1
	6.1 Preliminary Sensor Testing . . . . .	6-1
	6.2 Interface Circuit Design . . . . .	6-1
	6.3 Interferometer Tests . . . . .	6-3
	6.4 Sensor Electronics Noise . . . . .	6-6
7.	ELECTRONIC DESIGN . . . . .	7-1
	7.1 Loop Decoupling . . . . .	7-1
	7.2 Control Electronics . . . . .	7-1
	7.3 Start-Up Circuit . . . . .	7-5
8.	FABRICATION AND ASSEMBLY . . . . .	8-1
9.	INTEGRATION AND TEST . . . . .	9-1
	9.1 Center-of-Mass Location . . . . .	9-1
	9.2 Force Test Fixture Design . . . . .	9-1

9.3	Test Plan . . . . .	9-2
9.4	Test Results . . . . .	9-10
9.4.1	Open Loop Testing . . . . .	9-10
9.4.2	Closed Loop Testing . . . . .	9-16
9.4.3	Disturbance Sensitivity . . . . .	9-16
10.	CONCLUSIONS AND RECOMMENDATIONS . . . . .	10-1
10.1	Performance Summary . . . . .	10-1
10.2	Problem Areas . . . . .	10-1
10.3	Areas for Improvement . . . . .	10-2
10.4	Future Work . . . . .	10-3
Appendix A.	Finite Element Model . . . . .	A-1
Appendix B.	Eddy-Current Analysis and Testing . . . . .	B-1
Appendix C.	Collision Modelling . . . . .	C-1

REFERENCES

## List of Illustrations

2-1	Force disturbance sensitivity	2-2
2-2	Acceleration disturbance sensitivity	2-3
3-1	Final Bearing Concept	3-1
3-2	Permeance Magnitude	3-4
3-3	Permeance Phase	3-5
3-4	Current-to-Flux Transfer Function	3-6
3-5	Main Thermal Paths for Winding Losses	3-8
3-6	Thermal Model	3-8
4-1	Magnetic Bearing Shaft Assembly	4-2
4-2	Magnetic Bearing Assembly	4-3
4-3	Cross-Section of Magnetic Actuators and Translator Assemblies	4-4
4-4	Test Fixture Layout	4-6
5-1	Nomenclature Used for Identifying Bearing Locations	5-2
5-2	Magnetic Circuit Model	5-4
5-3	Block Schematic of the Power Amplifier Model	5-10
5-4	Torque Profile Used to Model Motor Disturbance	5-11
5-5	Block Schematic of the Compensation for the x Degree of Freedom	5-13
5-6	Open Loop Transfer Function for loop X	5-14
5-7	Shift in Openloop Crossover Frequency of X Loop	5-15
5-8	Shift in Openloop Crossover Frequency of Z loop	5-16
6-1	Sensor Position Error	6-2
6-2	Sensor Interface Block Diagram	6-3
6-3	Capacitor Sensor	6-4
6-4	4-Pole Butterworth Amplitude Response	6-5
6-5	4-Pole Butterworth Phase Response	6-5
6-6	Capacitor Sensor Test Setup	6-6
6-7	Capacitor Sensor Output vs Position	6-7
6-8	Capacitor Sensor Electronics Linearity Error	6-8
7-1	ODB Control/Power Electronics (2 pages)	7-2
7-2	Sensor Orientation; Coil Orientation	7-4
7-3	Current Driver Amplitude and Phase Response	7-6
7-4	Start-Up Circuit	7-7
9-1	Measured center-of-mass location	9-2
9-2	Bearing Test Fixture Layout	9-3
9-3	X Axis Force versus Current	9-12
9-4	Z Axis Force versus Current	9-13
9-5	X-Z Axis Cross Coupling	9-14
9-6	Z-X Axis Cross Coupling	9-15
9-7	Z Axis Field versus Current	9-17
9-8	X Axis Loop Response	9-18
9-9	Z Axis Loop Response	9-19
9-10	$\theta_x$ Loop Response	9-20

9-11	$\theta_y$ Loop Response	9-21
9-12	$\theta_z$ Loop Response	9-22
9-13	X Step Response	9-23
9-14	Z Step Response	9-24
9-15	$\theta_x$ Step Response	9-25
9-16	$\theta_y$ Step Response	9-26
9-17	$\theta_z$ Step Response	9-27
9-18	Displacement Sensitivity	9-28
9-19	Rotation Sensitivity	9-30
9-20	$\theta_z$ Rotation and Effort Sensitivity	9-31
9-21	Bench-top "Bang" Transients	9-32
9-22	Bench-top "Bang" Transients	9-33
9-23	Bench-top "Bang" Transients	9-34
9-24	Bench-top "Bang" Transients	9-35
A-1	Finite Element Model	A-1
A-2	Finite Element Mesh	A-2
A-3	X Axis Coil Solution	A-2
A-4	Z Axis Coil Solution	A-3
B-1	Toroid and Cross-Section	B-2
B-2	Boundary Conditions	B-4
B-3	Equivalent Permeances	B-8
B-4	Equivalent Circuit	B-9

## List of Tables

Table 2-1	System Specification	2-1
Table 2-2	Free-Travel Specification	2-4
Table 3-1	Magnetic Design Parameter	3-2
Table 3-2	Test Specimen Data	3-4
Table 3-3	Coil Parameters	3-7
Table 5-1	Open-Loop Eigenvalues	5-12

## **1. INTRODUCTION**

This final report documents the design, fabrication, integration, and testing of two magnetic bearings for the read/write head of an optical-disk data recorder. The feasibility study and preliminary design were performed under the first phase of this program and have been reported separately<sup>1</sup>. This introductory section provides a brief background of the application, and outlines the organization of the remainder of the report.

### **1.1 Background**

Optical-disk data recording technology is being developed by NASA for space applications. This technology has made possible devices which provide capacities of tens of gigabits, and hundreds of megabits-per-second data rates through the use of arrays of solid-state lasers applied to a magneto-optic disk. Bearings are an area where improvements are needed to allow these systems to be utilized in space applications. The porous-graphite air bearings used for the linear translator of the read/write head in the prototype unit, as well as the bearings used in the rotary spindle would be replaced by either magnetic bearings or mechanical (ball or roller) bearings. Based upon past experience, roller or ball bearings are not feasible for the translation stage. Unsatisfactory, although limited, experience exists with ball bearing spindles also. Magnetic bearings are an excellent alternative for both the translational and rotational stages of the devices.

The use of magnetic bearings is advantageous in optical-disk data recorders because of the absence of physical contact between the moving and stationary parts. This frictionless operation eliminates the position noise associated with mechanical bearings and provides extended life and reduced drag. The manufacturing tolerances that are required to fabricate magnetic bearings are also more relaxed than those required for precision ball and gas bearings. Since magnetic bearings require no lubricant, they are inherently compatible with a space (vacuum) environment. Magnetic bearings make this technology feasible for space applications and offer improved performance and reliability for terrestrial use.

### **1.2 Organization**

Each section of this report presents the effort and results of a major task of the program. Section 2 reiterates the specifications for the magnetic bearing system determined during Phase I, and describes revisions or additions which occurred during Phase I, and describes revisions or additions which occurred during development. Section 3 presents the magnetic design including the analysis performed and the control coil

design method. Section 4 discusses the mechanical design including modifications to the existing translator design to allow a form-fit-function installation. In Section 5, the design of the control algorithm is developed, including both linear and non-linear analyses, and the philosophy and strategy for system start-up. Section 6 presents the testing performed on the capacitive position sensor and describes the design of the sensor interface circuitry. In Section 7, the design of each electronic support circuit is discussed including the controller for the linear motor. Section 8 describes the processes involved in fabrication of the piece parts and assembly of the prototype unit, including problems encountered. In Section 9, the integration of the magnetic bearing system is discussed, and the test plan is presented along with the results of open-loop and closed-loop testing. Finally, Section 10 discusses the conclusions which are drawn from this development program, and the recommendations for potential improvements and future work.

## 2. SYSTEM SPECIFICATIONS

The specifications for the magnetic bearing system which were established during Phase I of this program are reiterated here in Table 2.1. The maximum force capability was determined by the requirement to provide 2g of acceleration along the two axes of suspension. During the course of the development, it was found that the translator carriage actually has a mass over 0.9 kgram. Therefore, the maximum force capability was increased to 18 Newtons.

**Table 2.1 System Specifications**

<b>STIFFNESS:</b>	
Parallel to disk	14 x 10 <sup>6</sup> N/M
Normal to disk	9 x 10 <sup>6</sup> N/m
SUSPENDED MASS	0.45 kgram
MAXIMUM FORCE	10 N
POSITION ACCURACY	2.5 micron
FIRST-MODE FREQUENCY	2000 Hz
<b>MAXIMUM STRAY FIELD:</b>	
At read-write head	0.003 T
At disk surface	0.2 T
<b>MAXIMUM ENVELOPE:</b>	
Length	2.9 cm
Width	3.8 cm
Height	3.2 cm

Another discrepancy which occurred during the course of the program was in the stiffness specification. A system requirements analysis performed by GE<sup>2</sup> indicated that the stiffness specification should be increased to 53x10<sup>6</sup> N/m in both axes. Since this specification is interpreted as static or "DC" stiffness, the use of integrators in the control loops will easily satisfy the increased requirements. Of more concern is the design bandwidth of the magnetic-bearing control loops, specified as 100 Hz. This is significantly lower than the natural frequency of the specified stiffness and the translator mass (1200 Hz). In order to illustrate the effect of the 100 Hz loop bandwidth, the plots of disturbance sensitivity as a function of disturbance frequency shown in Figures 2.1 and 2.2 were generated from estimated performance parameters. Figure 2.1

shows the single-frequency peak force applied directly to the translator carriage which will produce  $2.5\mu$  peak motion, whereas Figure 2.2 shows the single-frequency peak acceleration applied to the entire support structure which will result in a  $2.5\mu$  peak following error.

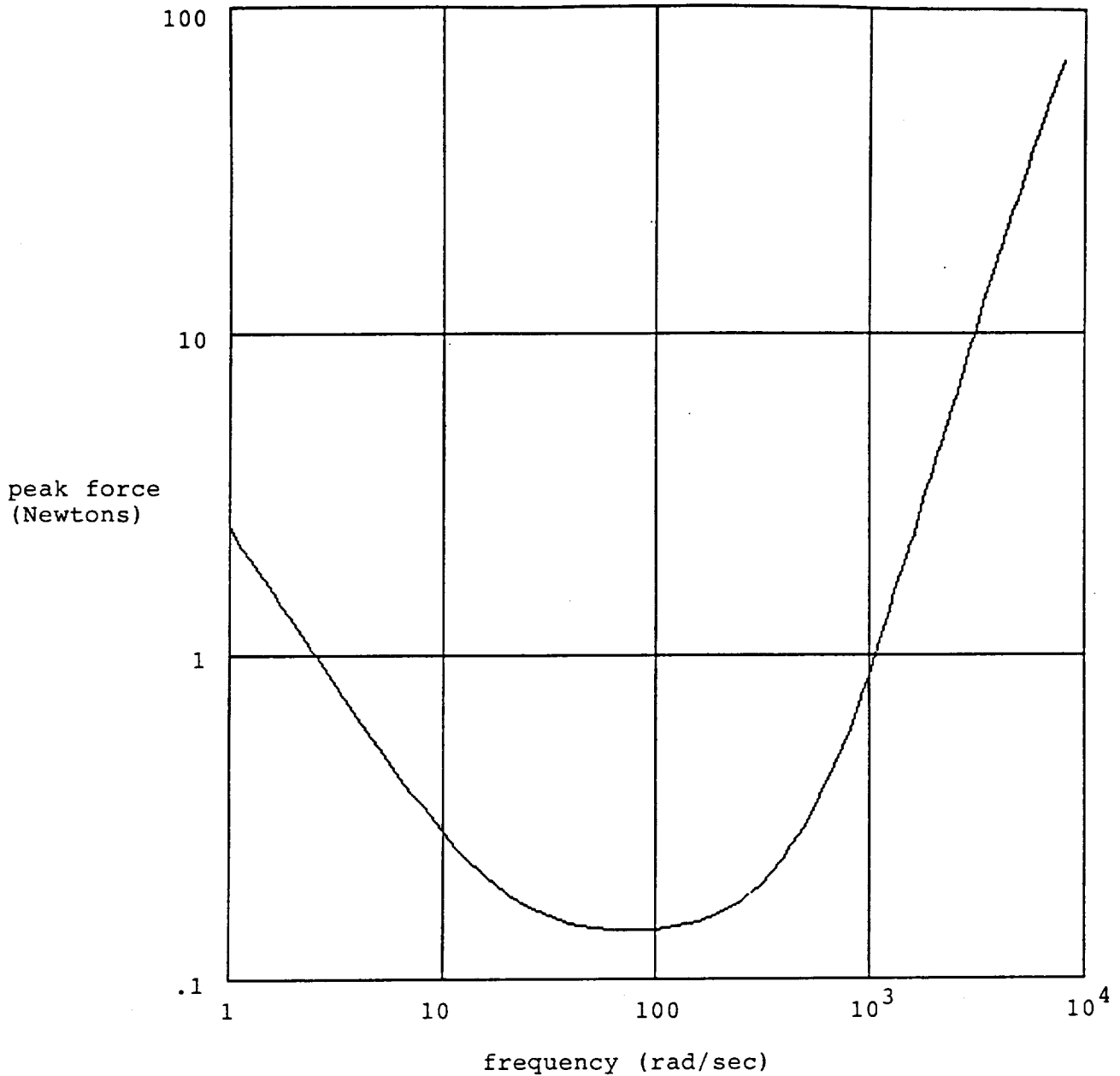


**Figure 2-1. Force Disturbance Sensitivity**

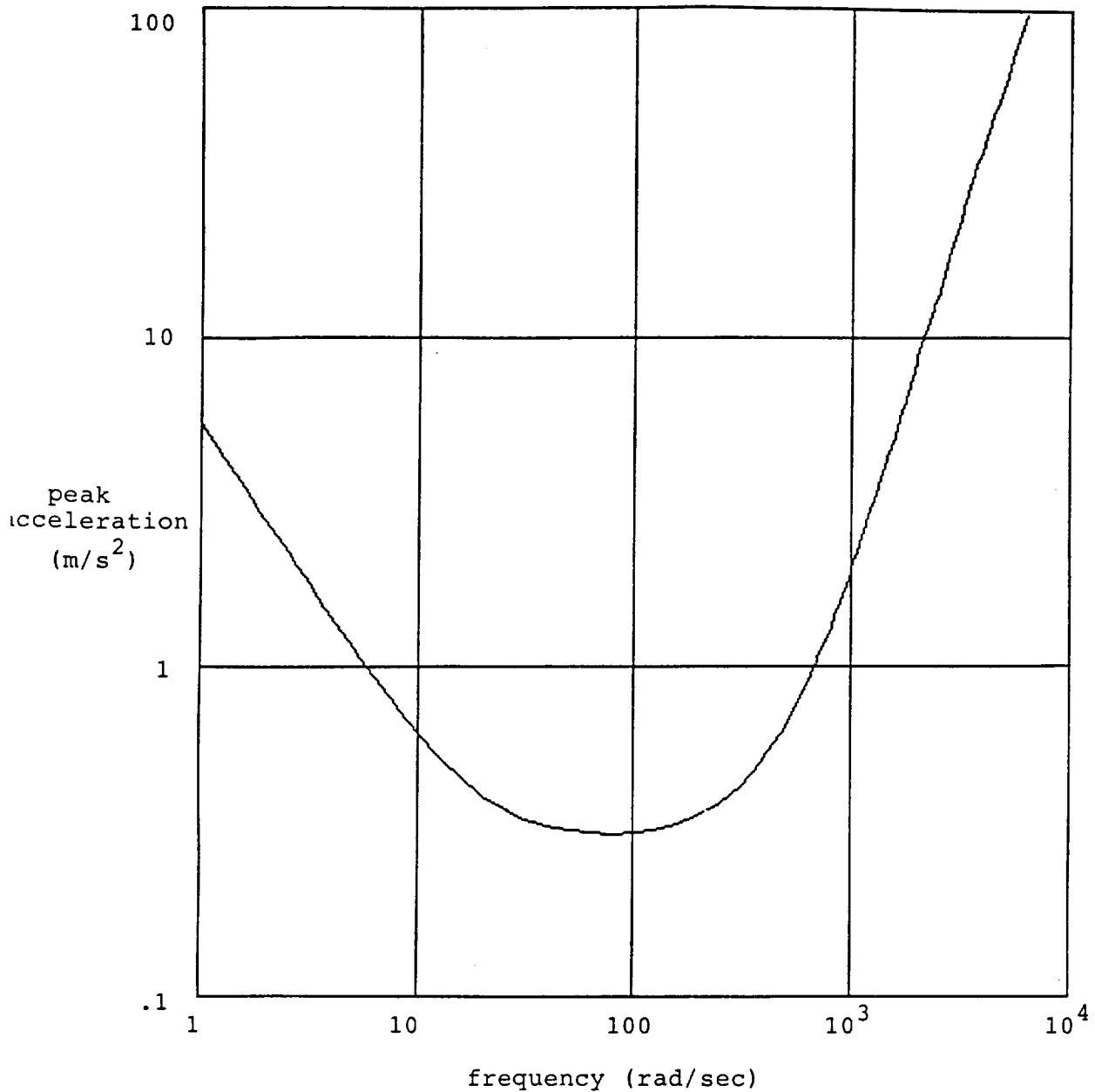


**Figure 2-2. Acceleration Disturbance Sensitivity**

A specification which was not established during Phase I is the limited amount of free-travel allowed along each of the suspension axes. Due to the limited clearances of the Heidenhain linear encoder, the maximum allowed free-travel is shown in Table 2-2. Also shown are the design limits for the free-travel.

**Table 2-2. Free-Travel Specification**

Motion Direction	Reference Direction	Maximum Travel	Design Limits
+X	Toward encoder	0.2mm	0.12mm
-X	Away from encoder	N/A	0.12mm
+Z	Away from focus head	0.2mm	0.15mm
-Z	Toward focus head	0.09mm	0.088mm

### 3. MAGNETIC DESIGN

The magnetic design effort for this phase started with the baseline configuration from the first phase shown in Figure 3.1. The two forces and three torques are produced by two mirror image pole piece sets acting on "C" channels in the shafts that replace the air bearing shafts. Each set is permanent-magnet biased and has six control coils and six pole faces. The unsymmetric configuration presents some problems because of magnetic force-coupling between the axes, but is necessary for compatibility with the linear motors.

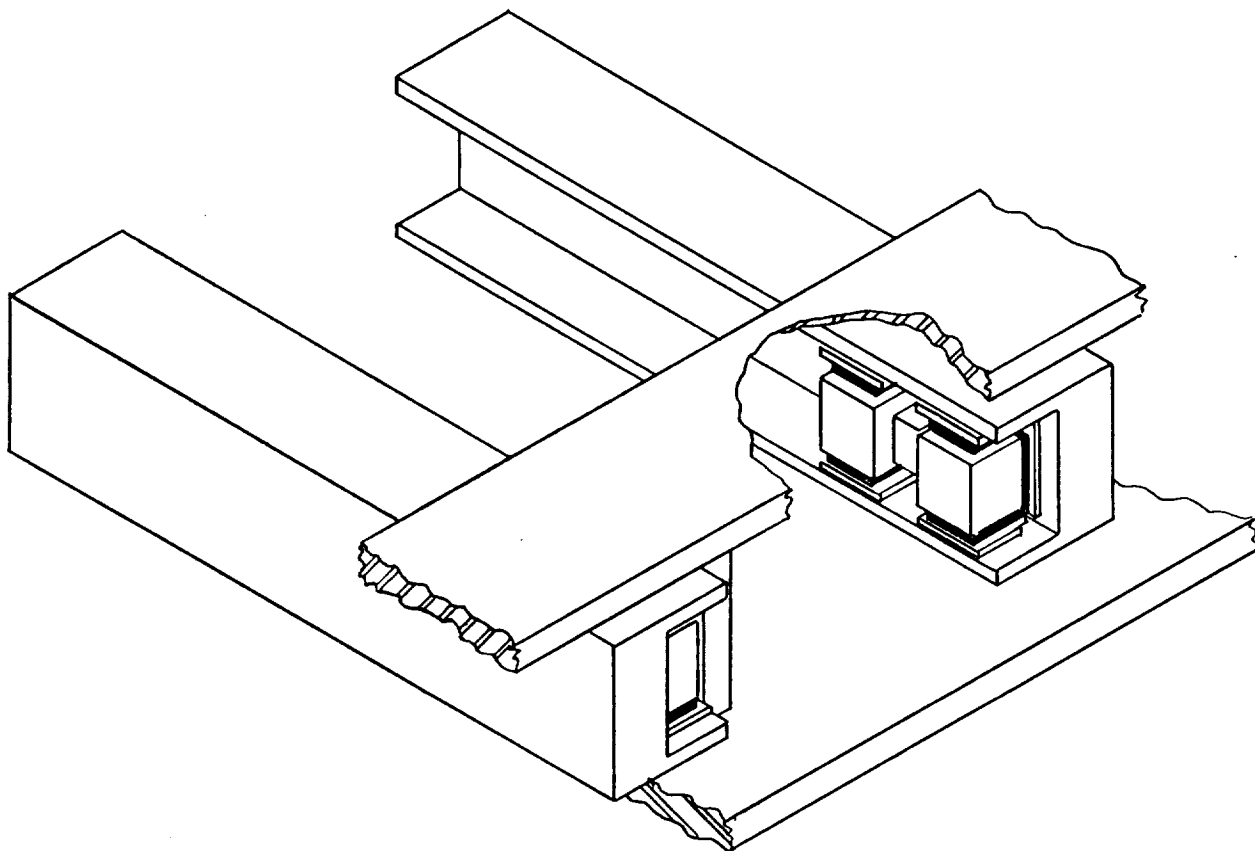


Figure 3-1. Final Bearing Concept

#### 3.1 Design Constraints

The magnetic design was tightly constrained by several factors. Geometrically, the size of the present translator carriage limits the length of the bearings, and the linear motor magnet and coil fields in the shafts limit material removal from the replacement shafts. Excessive material removal will cause

field saturation and corresponding decreases in permeability in the shafts. This will limit the force capability of both the linear motors and magnetic bearing actuators.

Other constraints were imposed by good design practice. The maximum unstable frequency was set at 50 Hz and the minimum gap was set at 0.254 mm (10 mils). Because the bandwidth is expected to be between 100 and 200 Hz, the unstable frequency should not be over 50 Hz. The air gap minimum was set both to limit the allowed travel as a percentage of the total gap, and to reduce the effects of manufacturing imperfections. Practically, the shaft and bearing dimensions can only be correct to about 0.02 mm (0.1 or 0.2 mils) and air gaps of less than 0.25 mm would amplify the percentage change in air gap from imperfections to several percent.

Taken together, the constraints leave little freedom in the magnetic design. The final design was arrived at through an iterative process using a magnetic model very similar to the one described in Section 5. A finite element model is covered in Appendix A. The permanent magnet material and dimensions were chosen for geometric compatibility with the envelope dimensions and ease of fabrication. The high energy density, linear demagnetization characteristics, and corrosion resistance of rare-earth Samarium Cobalt magnets made them an excellent choice for this application. The final magnetic design parameters are listed in Table 3.1.

Table 3.1

X-Axis Unstable Frequency	45 Hz
X-Axis Bias Field	0.149 T
X-Axis Pole Area	$3.78 \times 10^{-4} \text{ m}^2$
X-Axis Nominal Gap	$2.54 \times 10^{-4} \text{ m}^2$
Z-Axis Unstable Frequency	48 Hz
Z-Axis Bias Field	0.126 T
Z-Axis Pole Area	$1.67 \times 10^{-4} \text{ m}^2$
Z-Axis Nominal Gap	$3.05 \times 10^{-4} \text{ m}$
Magnet Parameters	SmCo, 19MGOe Energy Product
Magnet Size	1.27cm x 0.45cm x 0.48 cm

### 3.2 Material Selection

The other design parameter to be finalized from the baseline design was material choice for the pole pieces and replacement shafts. The most important properties were saturation fields and losses. Concerns about actuator-bandwidth reduction from eddy currents made material loss characteristics an important concern. The high fields carried by the shafts made material saturation characteristics crucial as well. Unfortunately, higher saturation materials tend to have higher losses. These factors led to the choice of silicon iron for the shafts and 80% nickel iron for the pole pieces. They are the lowest loss materials that have sufficient field capacity.

Unfortunately, the choice of low loss materials limits, but does not eliminate losses. Laminating the magnetic structure, the usual technique in motors and transformers to reduce eddy currents was not feasible because of the actuator configuration. Eddy currents arise when conductive materials are subjected to changing magnetic fields. They are governed by Lenz's law,  $E = -\nabla \times B$ , which says that changing applied fields will induce currents in conductive materials to oppose the change. The induced currents are dissipated through the resistance of the material. This not only heats the material, but reduces gap fields and forces. The attenuation of flux produced by the control coils also causes a roll off at frequencies above some "eddy current pole" frequency. Electromagnetic induction phenomena such as this are distributed-parameter effects which are not always modeled in a satisfactory way by lumped-parameter techniques. In fact, distributed-parameter models which ignore local saturation within the skin depth of the core (i.e. assume a constant permeability) are also somewhat limited in their predictive power.

The theory and analysis of induced currents in unlaminated cores is presented in Appendix B. The results derived in the appendix were used to provide an estimate for the frequency above which the flux is partially shielded. The analysis and actual measurements on the actuator indicate that the use of an unlaminated magnetic core did not severely impact performance.

Analytic predictions were compared to experimental data for annealed and unannealed test specimens. The results are summarized in Table 3-2. The model permeabilities were chosen for best agreement with the experimental results. Though the actual permeability of the specimens was very difficult to measure, the permeabilities used in the model are reasonable estimates based on material. Figures 3-2 and 3-3 show predictions for the magnitude and phase of the permeance of the unannealed specimen. The model has good agreement with the experimental data shown in Figure 3-4, but has shortcomings with phase at higher frequencies. While the model-predicted phase

losses do not exceed 45 degrees, the actual specimen showed additional phase loss at higher frequencies. The discrepancy is the result of unmodeled hysteresis losses.

Table 3-2

	Unannealed	Annealed
-3dB Magnitude Frequency	180 Hz	1080 Hz
$\theta$ Phase	-30°	-35°
Model Relative Permeability	600	30,000

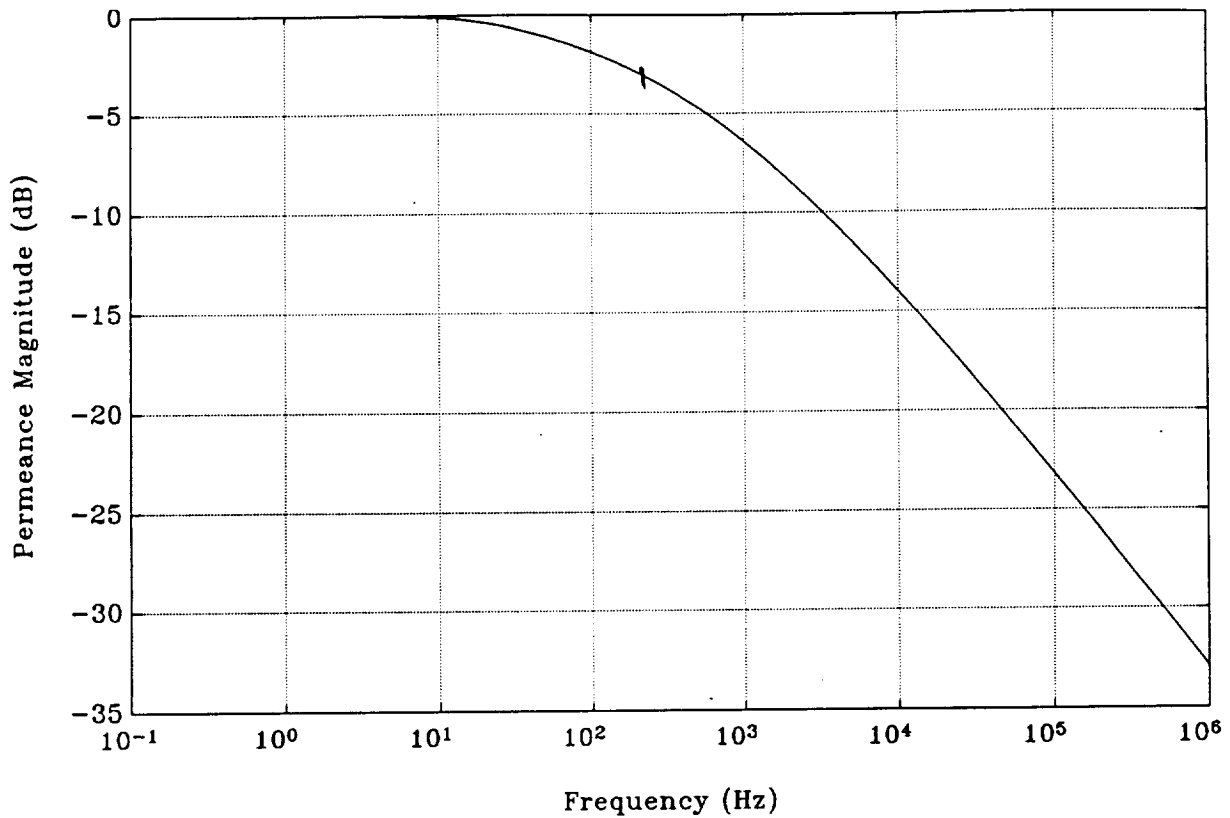


Figure 3-2. Permeance Magnitude

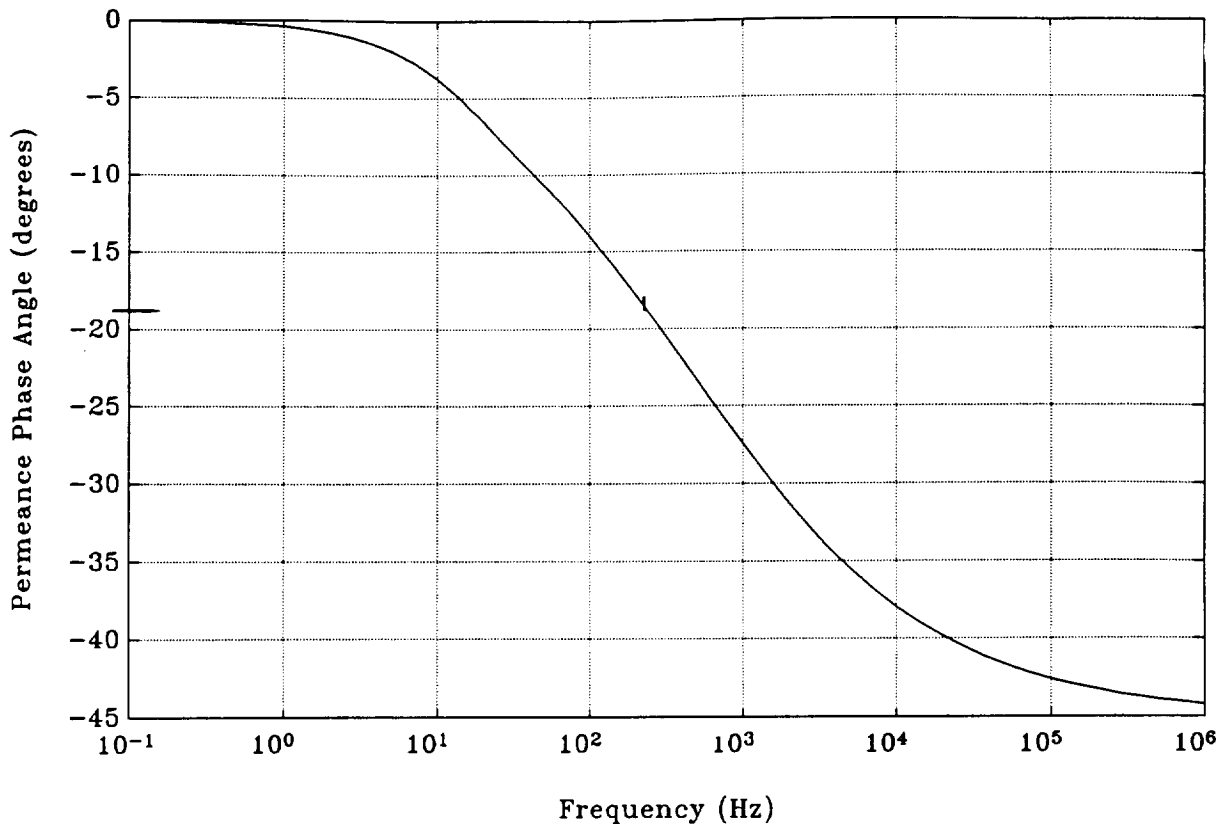


Figure 3-3. Permeance Phase

### 3.3 Control Coil Design

There are two separate analyses which specify the winding parameters for the control coils. The number of turns is determined by an analysis which considers the maximum voltage available to charge the inductance of the coil and the current risetime required for stability. The wire size is determined based on the maximum temperature rise allowed due to resistive heating under steady-state loading. Both analyses are discussed below.

#### 3.3.1 Voltage Analysis

The maximum excitation voltage required for the control coils is essentially determined by their inductance and the rate-of-rise of current needed for control-loop stability and disturbance rejection. It is known that, to prevent limit-cycling in the control-loop, the current must be able to rise fast enough to overcome the force of the "unstable spring" at the maximum allowed excursion of the translator. This can be written as:

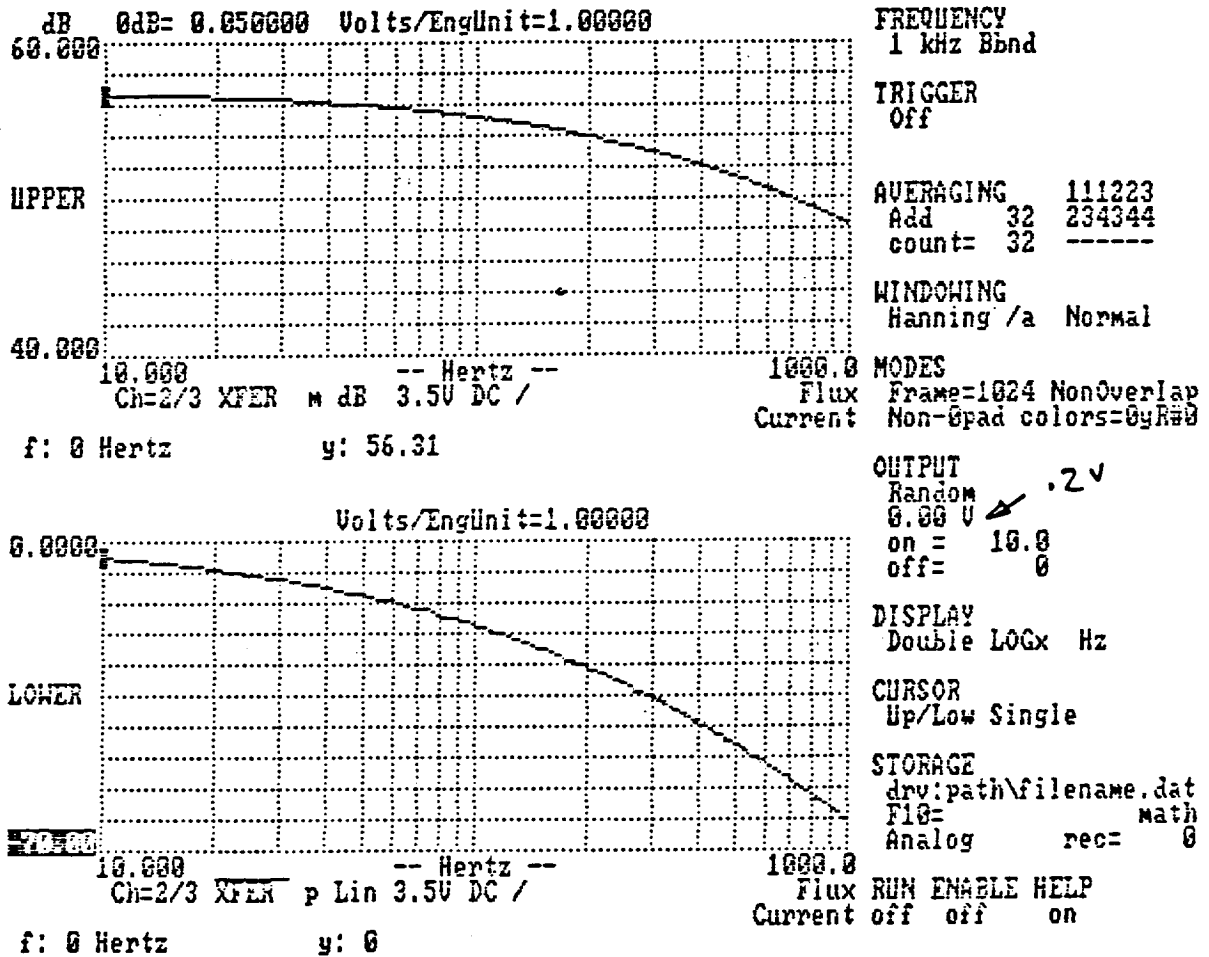


Figure 3-4. Current-to-Flux Transfer Function

$$\frac{dI}{dt} = \frac{V}{L} > \frac{K_x X_{stop}}{K_I \tau_u} \quad \text{Eq. (1)}$$

where:

- $K_x$ = unstable spring constant
- $X_{stop}$ = maximum excursion
- $K_I$ = force/current scale factor
- $\tau_u$ = unstable time-constant

If V is chosen as 10 volts, conservative solution of this equation results in using 130 turns for the x coils with a resulting inductance of 27 mHy for the two coils in series, and 120 turns for the z coils with a total inductance of 21 mHy.

The resulting force scale-factors are 28 N/Amp for each x coil-pair and 17 N/Amp for each z coil-pair. This would result in worst-case steady-state (1g) currents of 360 mA and 290 mA respectively, if the center-of-mass were located such that only half the coils for each axis could be used. Thus the respective current sources must be designed for a maximum current capability of 720 mA and 580 mA in order to provide for 2g peak acceleration.

There is an additional requirement placed on the rise time of the coil current by the fact that the center of force of the linear motor does not act on the center-of-mass of the translator and therefore creates a disturbance torque. This effect is significant enough that only the linear motor coil closest to the center-of-mass is excited in the existing system. Using this scenario and the measured center of mass location, the maximum voltage requirement for the 130 turn x coils is less than 10 volts even if the linear motor current waveform is assumed to be a step. The control coil parameters are summarized in Table 3-3.

Table 3-3. Coil Parameters

x-Axis Turns	130
x-Axis Inductance	27mHy
x-Axis Wire Size	AWG32
x-Axis Max Current (2g)	720mA
z-Axis Turns	120
z-Axis Inductance	21mHy
z-Axis Wire Size	AWG33
z-Axis Max Current (2g)	580mA

### 3.3.2 Thermal Analysis

A thermal analysis was performed to estimate the steady state temperatures present within the windings of the pole faces. The currents assumed for the analysis were those required to support the translator carriage under 1 G loading. Figure 3-5 shows how the pole faces and windings are mounted to the translator carriage. The thermal resistance of the air gaps between the pole faces/windings and the rails is significantly greater than the entire thermal path which includes conductance to the translator carriage in series with convection to the surrounding environment. Consequently, only the latter path was analyzed to estimate steady state temperatures.

The thermal model used is shown in Figure 3-6. It includes thermal resistances for the pole pieces, the interface between the pole pieces and the spacer plate, the spacer plate, the interface between the spacer plate and the translator carriage, and the translator carriage combined with convection to the surrounding air. The last resistance, corresponding to the

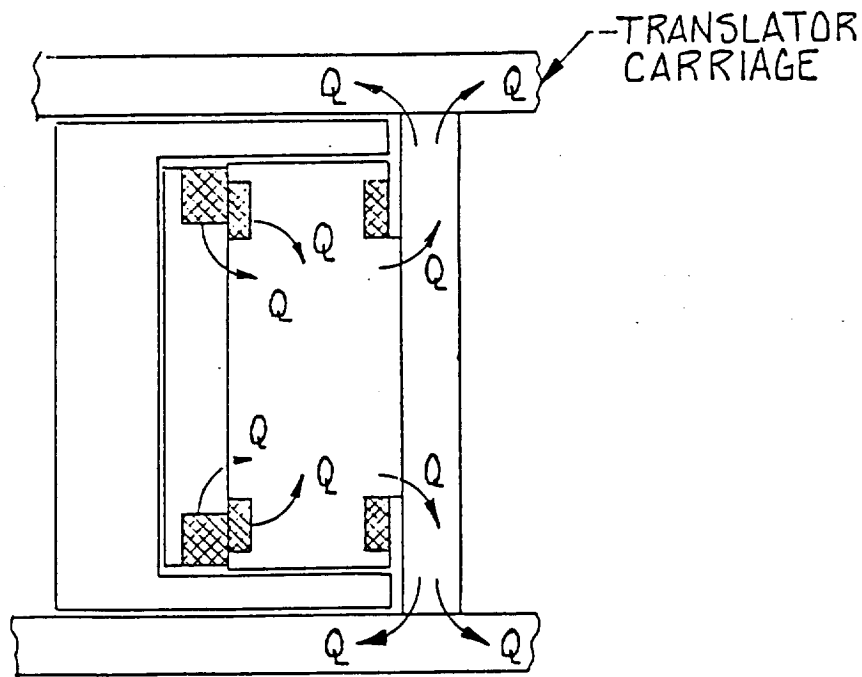


Figure 3-5. Main Thermal Paths for Winding Losses

translator carriage and convection to the surrounding air, was calculated by modeling it as a fin. The effective thermal resistance of a fin is

$$R = \frac{1}{\sqrt{hPKS} \tanh \sqrt{\frac{hP}{KS}}} \quad \text{Eq. (2)}$$

where:

- h ≡ load convection heat transfer coefficient
- P ≡ perimeter of fin
- K ≡ conductivity of fin material
- S ≡ cross-sectional area of fin

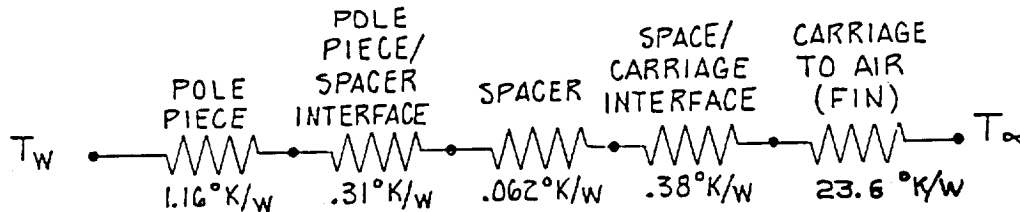


Figure 3-6. Thermal Model

The greatest uncertainty with this model is the coefficient of heat transfer associated with convection from the translator

carriage. A value of .0025 W/in<sup>2</sup>-C was used, based on available empirical formulas<sup>3</sup>. As indicated by these formulas, the actual value of the heat transfer coefficient depends on the orientation of the plate, the vertical length of the plate (if vertically-oriented) and the temperature difference between the plate and ambient. In order to accurately estimate the value, an iterative approach can be taken. However, for the purposes of this analysis a reasonable conservative value of .0025 W/in<sup>2</sup>-C was chosen. Other than the fin the thermal resistance values in the thermal model were simply based on the individual path length (l) divided by the product of the area of the path (A) and the conductivity of the material (K):

$$R = \frac{l}{AK} \quad \text{Eq. (3)}$$

All the thermal resistances associated with the spacer plate through convection to the environment account for the fact that the heat flux will roughly divide evenly between the upper and lower plate of the translator carriage.

Based on an worst case total dissipated power of .76 W for one z-axis pole face and one pair of x-axis pole faces, the windings operate at a temperature of 19.4 °C above ambient.

The thermal model was extended to include the temperature gradients within the windings. It is difficult to predict the effective conductivity of impregnated windings which include conductor, wire insulation and surrounding tape. If it is assumed that the impregnation is complete and that there is negligible air between wires, an effective conductivity of .031 W/in-°C is computed from available empirical formulas<sup>4</sup>, based on a conductivity of  $6.23 \times 10^{-3}$  W/in-°C for poly(amide-imide) insulation. In order to be conservative, a value of .004 W/in-°C was used, based on the same formulas with a 66% packing factor (percent copper) and air filling the remaining space. This substantially lower value stems primarily from the low conductivity of air relative to impregnation epoxy. In fact, the first set of pole faces was not impregnated. However, the replacement set currently being fabricated will be. The thermal model of the windings also included a thermal resistance for some tape surrounding the windings. The conductivity of the tape material was assumed to be .005 W/in-°K and its thickness to be .005 inches. Once again applying empirical formulas<sup>2</sup>, the resulting maximum temperature within the winding relative to its exterior temperature can be determined as a function of the dissipated power (Q) and the volume of the winding (V):

$$T_{MAX} = .587QV \quad \text{Eq. (4)}$$

where

$T_{MAX}$  = maximum temperature relative to exterior

The worst case scenario would be .74 W in one of the x-axis windings. With an x-axis winding volume of .025 in<sup>3</sup> the temperature rise within the winding is 17.4 °C. The sum of this value and the 19.4 °C temperature rise from ambient to the exterior of the windings yields a total steady state temperature increase of 36.8 °C relative to ambient at the hottest point within the windings. This is well below the acceptable operating temperature of poly(amide-imide) wire insulation which is 200°C.

## 4 MECHANICAL DESIGN

Once the envelope dimensions of the magnetic actuators were set, the mechanical design was finalized. The goal of the mechanical design was to translate the magnetic design into a manufacturable device. Instructions for fabrication and assembly were modified or enhanced to achieve the required surface tolerances and relative positioning accuracies.

### 4.1 Actuator Design

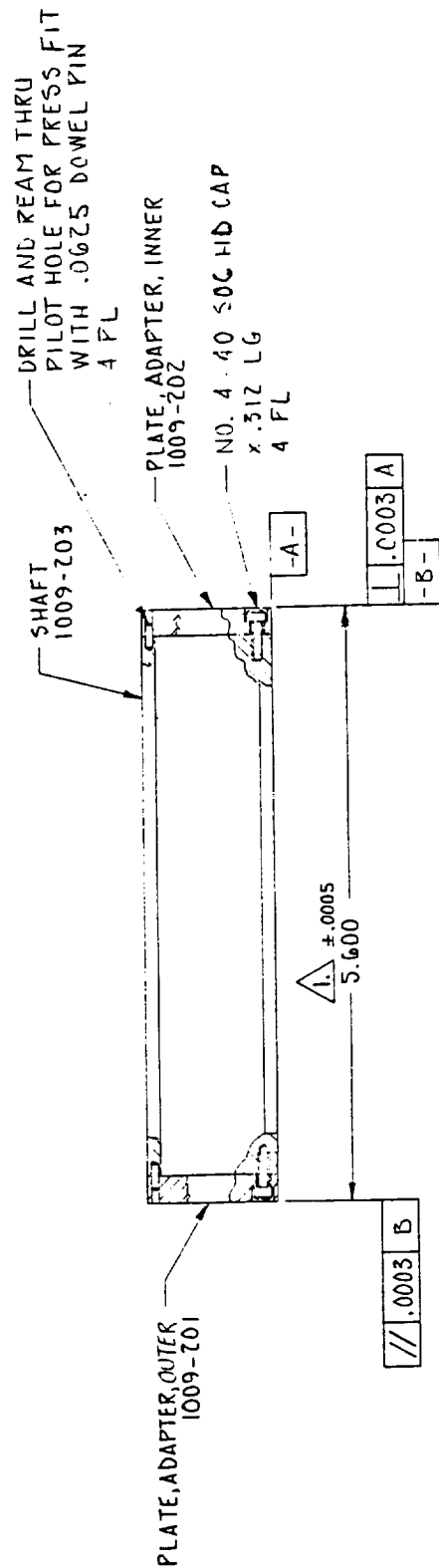
Implementation of the magnetic actuators required redesign of the flux return shafts (SatCon PN 1009-203). "C" channel recesses were added to the shafts to accept the bearing pole assemblies. To allow for compatibility with the existing frame design and to ease precision fabrication of the "C" section interior, interface adapter plates (SatCon PN's 1009-201 and 1009-202) were added to the ends of the shafts. The shaft assembly (SatCon Dwg # 1009-208) is shown in Figure 4-1.

As mentioned above, completion of the magnetic design of the bearing components allowed finalization of the mechanical design of the pole piece assemblies (SatCon PN 1009-111). A two-part design was selected to facilitate the winding and assembly of the actuator assemblies. The X-axis pole faces (SatCon PN 1009-103) are independently removable to allow installation of a previously wound coil. Additionally, this pole face design simplifies the manufacture of the Z-axis actuators (SatCon PN 1009-200). The coils for this actuator are wound directly onto the actuator and are subsequently potted.

Figure 4-2 presents an assembly drawing of one of the magnetic bearings sets (SatCon Dwg # 1009-207). The X- and Z-axis pole sets are assembled with their respective coil windings and are mounted with the bias magnet to the translator spacers (SatCon PN 1009-311). A combination of reliefs milled into one of the side surfaces of each Z-axis pole piece and the extension of the X-axis pole face over the reliefs ensure retention the bias magnet between the two actuators.

### 4.2 System Modifications

The modifications to the translator assembly include mounting provisions for both the pole pieces and the sensors. Complete actuator assemblies (Figure 4-2) consist of two pole piece assemblies and a bias magnet (SatCon PN 1009-111). An access hole is provided in the aluminum back plate to allow X-axis pole face removal without disassembly of the entire pole piece from the upright.



NOTE:  
 DASH 1 AND DASH 2 TO BE MATCH GROUND

Figure 4-1. Magnetic Bearing Shaft Assembly

- NOTES:
1. PARTS SHALL BE DISASSEMBLED TO WIND CONDUCTORS ONTO POLE PIECE, AFTER REASSEMBLY PARTS SHALL MEET SPECIFIED TOLERANCES
  2. SEE ATTACHED SHEET FOR ASSEMBLY PROCEDURES
  3. TO ACHIEVE .9700 DIM REMOVE EQUAL MATERIAL FROM BOTH SIDES

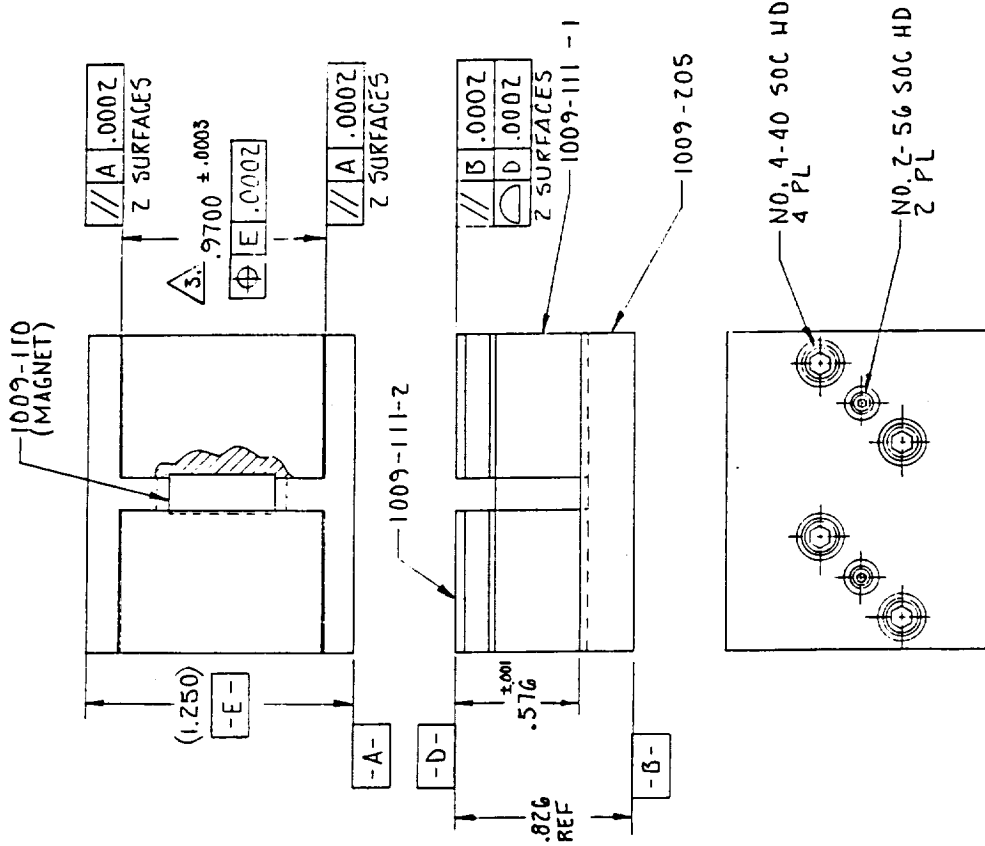
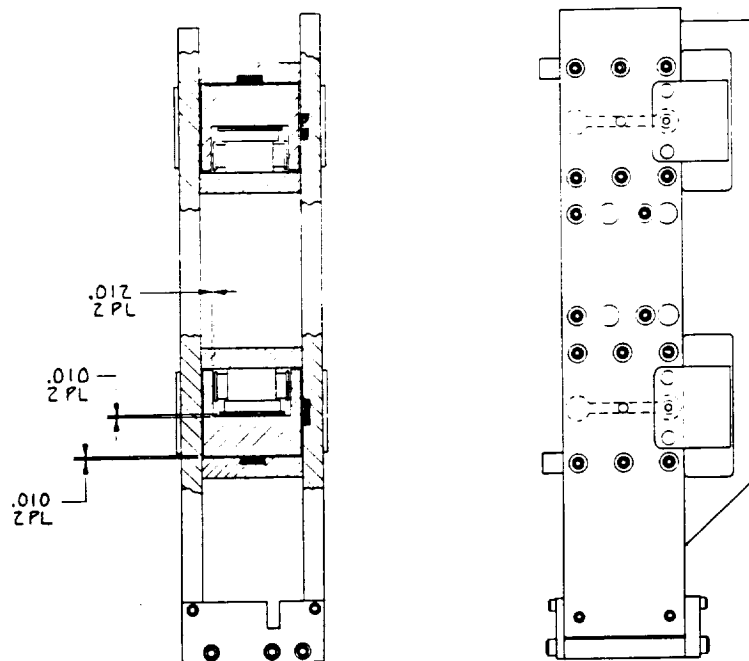


Figure 4-2. Magnetic Bearing Assembly

Each of the two complete original acutator assemblies was fastened and pinned to an inner aluminum upright of the translator assembly. A second set of actuators for delivery to NASA was designed and fabricated as well. Experience with the first set prompted slight design changes in the second set of pole pieces. Shallow slots were cut in the aluminum back plates to position the pole pieces in the Z axis, eliminating the dowel pins. This technique provides more dimensional stability over several assembly/disassembly cycles and allows a closer fit between the pole pieces and permanent magnet.

The capacitive position sensor is disk shaped with 0.312" diameter and 0.100" thickness. Eight total sensors, four per shaft are used. Shallow, round recesses were machined into the top translator plate (SatCon PN 1009-204) and into the outer set of aluminum spacers (SatCon PN 1009-205), both oriented in towards each shaft. The sensing surfaces consist of the outer surfaces of the shafts: the top surface and the side surface



**Figure 4-3. Cross-Section of Magnetic Actuators and Translator Assemblies**

opposite the magnetic actuator assemblies. Figure 4-3 presents a cross section of the translator, shaft and magnetic actuator assemblies (SatCon Dwg # 1009-301), showing the relative positions of the "C"-channel shafts, the actuators and the position sensors.

The first set of outer spacers had a small design problem, however. The sensor leads were routed to the front of the translator carriage, causing some restriction of radial travel. A redesigned set solved this problem by feeding the leads from the plate over the top of the carriage.

Detail drawings of individual components shown in the assembly drawings presented here can be found in Volume II. Also shown are the tolerancing requirements for fabrication and assembly of the frame. Considerations for the magnetic bearing system require flatness and squareness tolerances somewhat less than, but similar to, those used in the air bearing system.

### **4.3 Holding Fixture**

A holding fixture was fabricated for closed loop testing and table-top display. A layout drawing is shown in Figure 4-4 and the individual part drawings are included in Volume II. Based on the GE optical-disk-buffer fixture, it holds the support frame rigidly while allowing the carriage to slide freely. The holding fixture is reconfigurable and allows the frame and carriage to be oriented either vertically or horizontally. Also included in the holding fixture is a mounting clamp for a linear variable differential transformer (LVDT), used to provide position feedback to the linear motor controller. The LVDT (Schaevitz model 1000 HR) consists of a cylindrical coil body and movable core. The body is clamped to the holding fixture and the core is attached to the carriage near the linear encoder by means of a threaded rod and interface clamp. This provides simple non-contacting radial position readings to be made with the addition of complementary LVDT conditioning electronics.

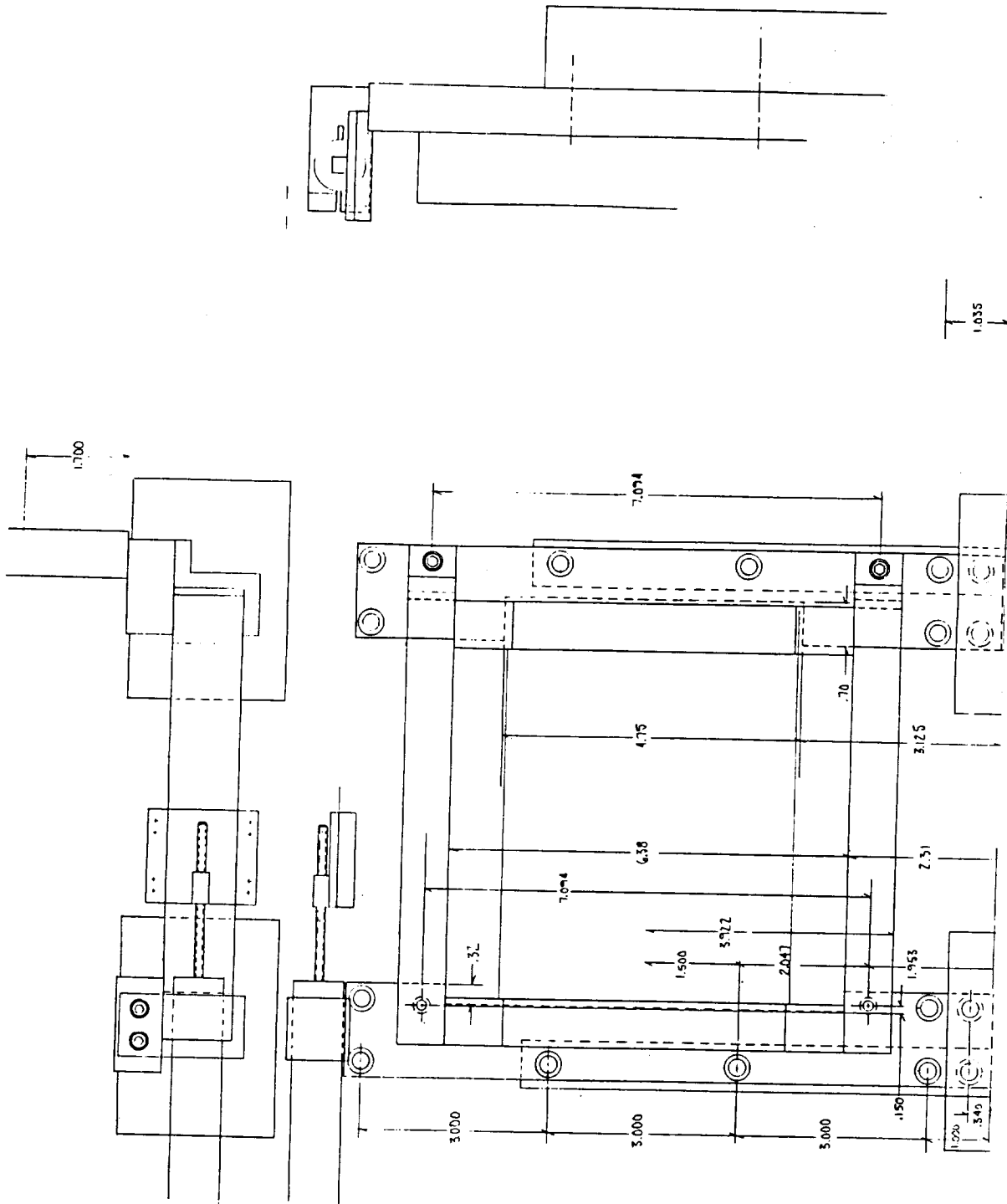


Figure 4-4. Test Fixture Layout

## 5. CONTROLLER DESIGN

The following sections describe the modelling, design, and simulation effort expended in the linear bearing controller design.

### 5.1 Bearing Model

To facilitate the design of a controller for the linear bearing, a model was developed to describe the behavior of the magnetic circuits and the resulting force/current and force/displacement characteristics of the linear bearing. The nomenclature used is shown in Figure 5.1 below.

The nominal coordinates of the center-of-force of each actuator referenced to the center-of-mass are (in meters):

$X_1 = -4.851e-2$	$Y_1 = -1.800e-2$	$Z_1 = 1.571e-2$
$X_2 = -4.851e-2$	$Y_2 = -1.800e-2$	$Z_2 = -1.571e-2$
$X_A = -5.448e-2$	$Y_A = -1.800e-2$	$Z_A = -1.300e-3$
$X_3 = -4.851e-2$	$Y_3 = 3.000e-3$	$Z_3 = 1.571e-2$
$X_4 = -4.851e-2$	$Y_4 = 3.000e-3$	$Z_4 = -1.571e-2$
$X_B = -5.448e-2$	$Y_B = 3.000e-3$	$Z_B = -1.300e-3$
$X_5 = 2.185e-2$	$Y_5 = -1.800e-2$	$Z_5 = 1.571e-2$
$X_6 = 2.185e-2$	$Y_6 = -1.800e-2$	$Z_6 = -1.571e-2$
$X_C = 2.706e-2$	$Y_C = -1.800e-2$	$Z_C = -1.300e-3$
$X_7 = 2.185e-2$	$Y_7 = 3.000e-3$	$Z_7 = 1.571e-2$
$X_8 = 2.185e-2$	$Y_8 = 3.000e-3$	$Z_8 = -1.571e-2$
$X_D = 2.706e-2$	$Y_D = 3.000e-3$	$Z_D = -1.300e-3$

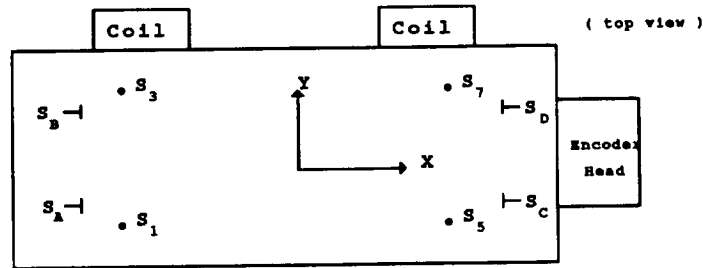
Axis Y is the linear motor drive axis and is not controlled by the magnetic bearing.

The magnets, amplifiers, coils, etc., effective along the x-axis are designated with alphabetical letters A-D. The magnets, amplifiers, coil pairs are AC & BD. Hence, for example, the common current driving coil pair AC is designated as  $I_{AC}$ .

The magnets, amplifiers, coils, etc. effective along the z-axis are designated with numerals 1-8. The magnets, amplifiers, coils are paired 1-2, 3-4, 5-6, 7-8 with the odd numbered members in the z+ space and the even numbered members in the z- space.

Forces are designated as  $F_{X_A}-F_{X_D}$  &  $F_{Z_1}-F_{Z_8}$ . A force component is considered as positive if it acts in the positive direction of the axis. For example current  $I_{12}$ , when positive produces a positive force i.e. the sum  $(F_{Z_1} + F_{Z_2})$  acts along the positive z axis.

**Sensor Orientation**



**Coil Orientation**

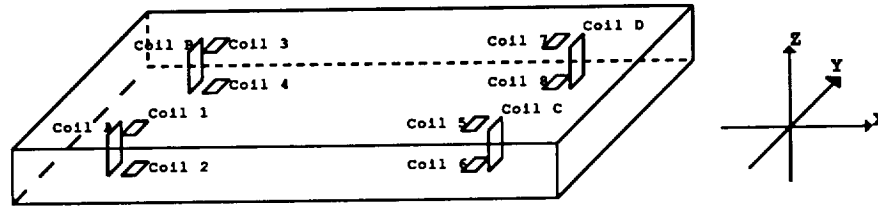


**Figure 5-1 Nomenclature Used for Identifying Bearing Locations**

The bearing has five degrees of freedom  $x, z, \theta_x, \theta_y$  and  $\theta_z$  which describe its location within the bearing frame. The air gaps  $[g_a, g_b, g_c, g_d, g_1, g_2, g_3, g_4, g_5, g_6, g_7, g_8]$  at each pole face are described by

$$[g]^{tr} = [T] * [x, z, \theta_x, \theta_y, \theta_z]^{tr} \quad \text{Eq. 5}$$

where T is a transform derived from the bearing geometrical parameters.

**5.1.1 Magnetic Circuit Model**

The first step in finding the magnetic forces is solving for the air gap fluxes as a function of air gap lengths and control coil currents. The air gap fluxes can be found from a linear, lumped parameter approximation to the magnetic field problem. With this technique, the air gap fluxes are found to be linear functions of coil currents but nonlinear function of the air gap lengths and, therefore, slide position.

The linear equivalent model for one side of the slide, the negative x side, is shown in Figure 5.2 below. Starting from the left side of the magnetic circuit, the permanent magnet is

modelled as a constant magnetomotive force (MMF) source  $M_m$  in series with its reluctance  $R_m$ . The top of the circuit models the pole piece in the lower left-hand corner of Figure 5.1, the negative x, negative y pole piece. This pole piece is modelled by the MMFs ( $M_A, M_1, M_2$ ) produced by the coil currents ( $I_A, I_1, I_2$ ) in series with the air gap reluctances ( $R_A, R_1, R_2$ ) and the reluctances  $R_{i1}$  of the iron paths in the pole.

The pole piece at the upper left-hand side of Figure 5.1 is shown at the bottom of Figure 5.2, and is modelled similarly. The two pole pieces are connected by a reluctance  $R_{i1}$  that models the reluctance of the return iron path in the stator.

As developed in Section 3, the permanent magnet lumped parameters are given by:

$$M_m = \frac{B_r}{l_m \mu_m} = \text{MMF of the permanent magnet.} \quad \text{Eq. (6)}$$

where

$B_r$  = Residual magnetic field of the permanent magnet  
 $l_m$  = permanent magnet length  
 $\mu_m$  = permanent magnet magnetic permeability,

$$R_m = \frac{l_m}{\mu_m A_m} = \text{permanent magnet reluctance.} \quad \text{Eq. (7)}$$

where

$l_m$  = permanent magnet length  
 $A_m$  = permanent magnet cross-sectional area.

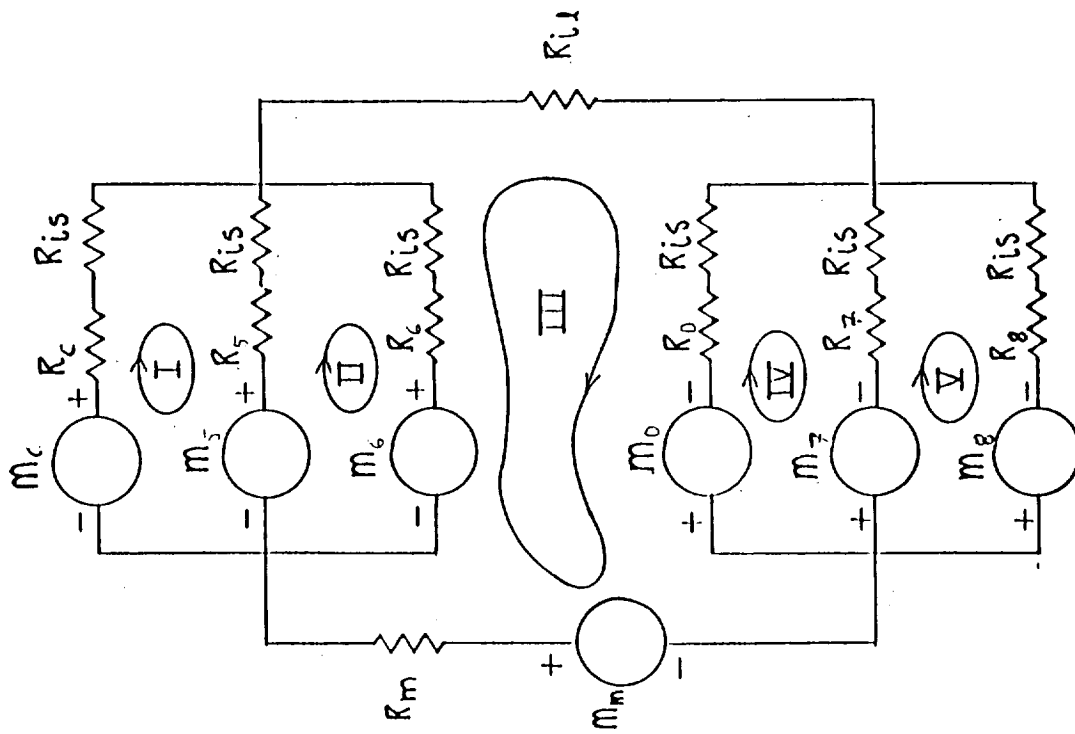
The iron path reluctances are

$$R_{is} = \frac{l_{is}}{\mu_i A_{is}} = \text{Reluctance of pole paths.} \quad \text{Eq. (8)}$$

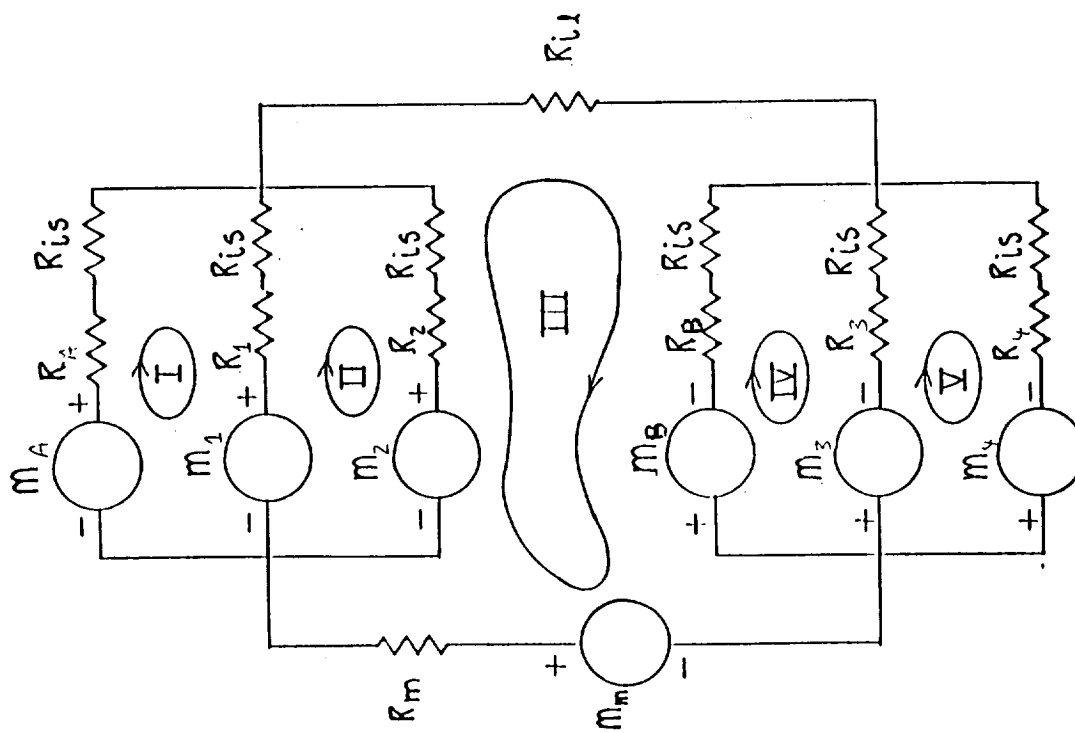
where

$l_{is}$  = length of pole path  
 $\mu_i$  = magnetic permeability of iron  
 $A_{is}$  = pole cross-sectional area.

$$R_{i1} = \frac{l_{i1}}{\mu_i A_{i1}} = \text{reluctance of return path} \quad \text{Eq. (9)}$$



Postivie x-side Magnetic Circuit



Negative x-side Magnetic Circuit

Figure 5-2. Linear Equivalent Model of the Magnetic Circuit

where

$l_{11}$  = return path length

$A_{11}$  = return path cross-sectional area.

The coil MMFs ( $M_A, M_B, M_1, M_2, M_3, M_4$ ) are determined by the number of turns on the coil and the coil currents:

$$\begin{aligned}M_A &= N_{tx}I_A = N_{tx}I_{AC} \\M_B &= N_{tx}I_B = N_{tx}I_{BD} \\M_1 &= N_{tz}I_1 = N_{tz}I_{12} \\M_2 &= N_{tz}I_2 = N_{tz}I_{12} \\M_3 &= N_{tz}I_3 = N_{tz}I_{34} \\M_4 &= N_{tz}I_4 = N_{tz}I_{34}\end{aligned}$$

where

$N_{tx}$  = Number of turns on x-coils

$N_{tz}$  = Number of turns on z-coils

$I_{AB}, I_{CD}, I_{12}, I_{34}$  are control coil currents

The air gap reluctances, ( $R_A, R_B, R_1, R_2, R_3, R_4$ ) are given by:

$$R_A = \frac{g_A}{\mu_o A_{gx}}$$

$$R_B = \frac{g_B}{\mu_o A_{gx}}$$

$$R_1 = \frac{g_1}{\mu_o A_{gz}}$$

$$R_2 = \frac{g_2}{\mu_o A_{gz}}$$

$$R_3 = \frac{g_3}{\mu_o A_{gz}}$$

$$R_4 = \frac{g_4}{\mu_o A_{gz}}$$

Eq. (10)

where

$\mu_o$  = magnetic permeability of air

$A_{gx}$  = x-direction pole face areas

$A_{gz}$  = z-direction pole face areas

$g_A, g_B, g_1, g_2, g_3, g_4$  are air gap lengths, which are a function of the slide position

Values for these parameters are found in Table 3.1 of Section 3.1.

The gap fluxes are found by solving for the fluxes in the five loops labelled I, II, III, IV, and V in Figure 5.2. The vector of loop fluxes  $\phi_n$  are a linear function of the reluctances and MMFs given by

$$\mathbf{R}_n \phi_n = \mathbf{M}_n \quad (\text{Eq. 11})$$

where

$\mathbf{R}_n$  is the matrix of loop reluctances

$\phi_n$  is the vector of loop fluxes

$\mathbf{M}_n$  is the vector of loop MMFs.

These are given in terms of the lumped parameters of Figure 5.2 as:

$$\mathbf{R}_n = \begin{bmatrix} (\overline{R_A} + \overline{R_1}) & -\overline{R_1} & 0 & 0 & 0 \\ -\overline{R_2} & (\overline{R_1} + \overline{R_2}) & 0 & 0 & 0 \\ 0 & -\overline{R_2} & (R_m + \overline{R_2} + R_{11} + \overline{R_B}) & -R_B & 0 \\ 0 & 0 & -\overline{R_B} & (\overline{R_B} + \overline{R_3}) & -\overline{R_4} \\ 0 & 0 & 0 & -\overline{R_4} & (\overline{R_3} + \overline{R_4}) \end{bmatrix}$$

Eq. (12)

$$\phi_n = [\phi_I, \phi_{II}, \phi_{III}, \phi_{IV}, \phi_V]^T$$

Eq. (13)

$$\underline{\mathbf{M}}_n = \begin{bmatrix} M_A - M_1 \\ M_1 - M_2 \\ M_m + M_2 - M_B \\ -M_B + M_3 \\ -M_4 + M_4 \end{bmatrix} = \begin{bmatrix} N_{tx} I_{AC} - N_{tz} I_{12} \\ 0 \\ M_m + M_{tz} I_{12} - M_{tx} I_{AB} \\ -N_{tx} I_{AB} + N_{tz} I_{34} \\ 0 \end{bmatrix}$$

where the overbar indicates the series combination of the gap and pole reluctances as:

$$\begin{aligned} \overline{R_A} &= R_A + R_{1s} \\ \overline{R_B} &= R_B + R_{1s}, \text{ etc.} \end{aligned} \quad (\text{Eq. 15})$$

The five linear equations in the loop fluxes represented by Eq. 1 above can be solved for the fluxes, for example by inverting the reluctance matrix  $\mathbf{R}$  to yield

$$\underline{\phi}_n = R_n^{-1} \underline{M}_n \quad \text{Eq. (16)}$$

The gap fluxes  $\underline{\phi}_n$  of the negative x side can then be found as linear combinations of the loop fluxes as

$$\underline{\Phi}_n = T_{\phi\phi} \underline{\phi}_n \quad \text{Eq. (17)}$$

where

$\underline{\Phi}_n$  = vector of gap fluxes =  $[\Phi_A, \Phi_1, \Phi_2, \Phi_B, \Phi_3, \Phi_4]^T$

$\underline{\phi}_n$  = vector of loop fluxes

$T_{\phi\phi}$  = transformation matrix

$$T_{\phi\phi} = \begin{bmatrix} 1 & 0 & 0 & 0 & 0 \\ -1 & 1 & 0 & 0 & 0 \\ 0 & -1 & 1 & 0 & 0 \\ 0 & 0 & 1 & -1 & 0 \\ 0 & 0 & 0 & 1 & -1 \\ 0 & 0 & 0 & 0 & 1 \end{bmatrix} \quad \text{Eq. (18)}$$

The gap fluxes for the negative x-side, therefore, are given as a function of the coil currents ( $\underline{I}$ ) and gaps ( $\underline{g}$ ) by

$$\underline{\Phi}_n = T_{\phi\phi} \cdot R_n^{-1}(\underline{g}) \cdot \underline{M}_n(\underline{I}) \quad \text{Eq. (19)}$$

The gap fluxes for the positive x-side ( $\underline{\Phi}_p$ ) can similarly be found from the magnetic circuit shown in Figure 5.3 below.

### 5.1.2 Nonlinear Force Model

The nonlinear force model is based on the assumption that the force F generated at a magnet pole face is given by

$$F = 0.5 * B^2 * A / \mu_0 \quad \text{Eq. (19)}$$

where "B" is the average flux density at the pole face and "A" is the area of the pole face. This assumption has been shown to hold good over a wide range of applications.

Considering the geometry of the linear bearing, the magnetic circuits are strongly coupled except when the bearing is centrally located with respect to the frame. In the general case the linear model of the magnetic circuits derived in Section 5.1.1 gives flux densities at each of the pole faces as a

function of the bearing displacement and the coil excitations. These are used to calculate the forces at each pole face. The forces at each pole face are next transformed to rigid body forces and moments on the bearing i.e.

$$[F_x, F_z, M_x, M_y, M_z]^{-1} = [T]^{-1} * [F_g] \quad \text{Eq. (20)}$$

where  $[F_g]$  is a vector representing the air gap forces and  $[T]$  is a transform derived from the bearing geometrical parameters.

The nonlinear force model is used in the dynamic simulation to model the behavior of the bearing over the allowed range of free travel.

### 5.1.3 Linear Force Model

The linear model is derived essentially from the linear magnetic circuit model and the linearized form of force expression Eq. (19) "B" is expressed in terms of the air gap, coil excitation and permanent magnet bias at the jth pole face. Restating Eq. (19)

$$F_j = K(\Delta b_j + B_{0j})^2 \quad \text{Eq. (21)}$$

where K is a constant,  $B_{0j}$  is the permanent magnet bias flux density and  $\Delta b_j$  is the control flux generated by the excitation coil.

The coil pair "AC" is driven by the current  $I_{ac}$  and the pair "12" is driven by the current  $I_{12}$  resulting in control fluxes  $\Delta b_{ac}$  and  $\Delta b_{12}$ . Summing the forces at the pole faces "A" and "C" using Eq. (21) leads to

$$\Delta F_{X_{ac}} = F_{xa} + F_{xb} = k'_{ac} * \Delta b_{ac} \quad \text{Eq. (22)}$$

Similarly summing the forces at the pole faces "1" and "2" leads to

$$\Delta F_{Z_{12}} = F_{xa} + F_{xb} = k'_{12} * \Delta b_{12} \quad \text{Eq. (23)}$$

where  $k'_{ac}$  and  $k'_{12}$  are constants. However, ignoring iron path reluctances at the jth control coil

$$\Delta b_j = \mu_o * I_j / G_j \quad \text{Eq. (24)}$$

which for small increments in  $I_j$  and  $G_j$  approximates to

$$\Delta b_j = k_i * \Delta i_j + k_g * \Delta g_j \quad \text{Eq. (25)}$$

Combining these into Eqs. (22) and (23) results in

$$\Delta F_{X_{ac}} = k'_{iac} * \Delta i_{ac} + k'_{gac} * \Delta g_{ac} \quad \text{Eq. (26)}$$

and

$$\Delta F_{z12} = k'_{i12} \Delta i_{12} + k'_{g12} \Delta g_{12} \quad \text{Eq. (27)}$$

Linearized force expressions can be derived for the forces generated at the rest of the pole faces i.e

$$\Delta F_{x_{bc}} = k'_{i_{bc}} \Delta i_{bc} + k'_{g_{bc}} \Delta g_{bc} \quad \text{Eq. (28)}$$

$$\Delta F_{x_{34}} = k'_{i_{34}} \Delta i_{34} + k'_{g_{34}} \Delta g_{34} \quad \text{Eq. (29)}$$

$$\Delta F_{x_{56}} = k'_{i_{56}} \Delta i_{56} + k'_{g_{56}} \Delta g_{56} \quad \text{Eq. (30)}$$

$$\Delta F_{x_{78}} = k'_{i_{78}} \Delta i_{78} + k'_{g_{78}} \Delta g_{78} \quad \text{Eq. (31)}$$

These are linear functions of the respective excitation currents and there is no cross-coupling between the forces acting in the x and z directions. This however does not strictly hold true when the slide is at a displaced position away from the center. For the linear analysis and controller design it is assumed that the linear force relationship and the zero cross coupling holds true.

#### 5.1.4 Eddy Current Model

Measurements of the transfer function "force/excitation-current" made on the fully assembled magnetic bearing showed the first break-point located beyond 600Hz. A precise value for this break frequency could not be ascertained because of signals introduced by structural resonances in the bearing and the measurement set-up. However, the cumulative effects of eddy currents, hysteresis and other loss mechanisms present in the bearing can be assumed to result in a insignificant phase and gain loss at 500 Hz. Consequently both the linear and the non-linear analyses omit modelling eddy current and hysteresis loss mechanisms.

#### 5.1.5 Amplifier Model

The amplifier is assumed to be linear over the operational current and frequency range. The amplifiers are designed to have a frequency response of 1000Hz. The linear analysis and design takes this into account. The non-linear simulation also imposes  $\delta I / \delta t$  (rate of change of current) limits on the amplifiers. A schematic of the amplifier is shown in Figure 5.3. The rate limits are essentially imposed by the amplifier rail voltage. This is an important parameter in determining limits on the rate of change of disturbance input which the control loop can withstand without going into limit cycles or going totally unstable.

#### 5.1.6 Sensor Model

The 8 capacitive sensors measure the air-gaps at their respective locations. These measurements are transformed to the displacements and rotations  $\Delta x$ ,  $\Delta z$ ,  $\Delta \theta_x$ ,  $\Delta \theta_y$ ,  $\Delta \theta_z$ . The individual sensors were calibrated on a measurement setup. The

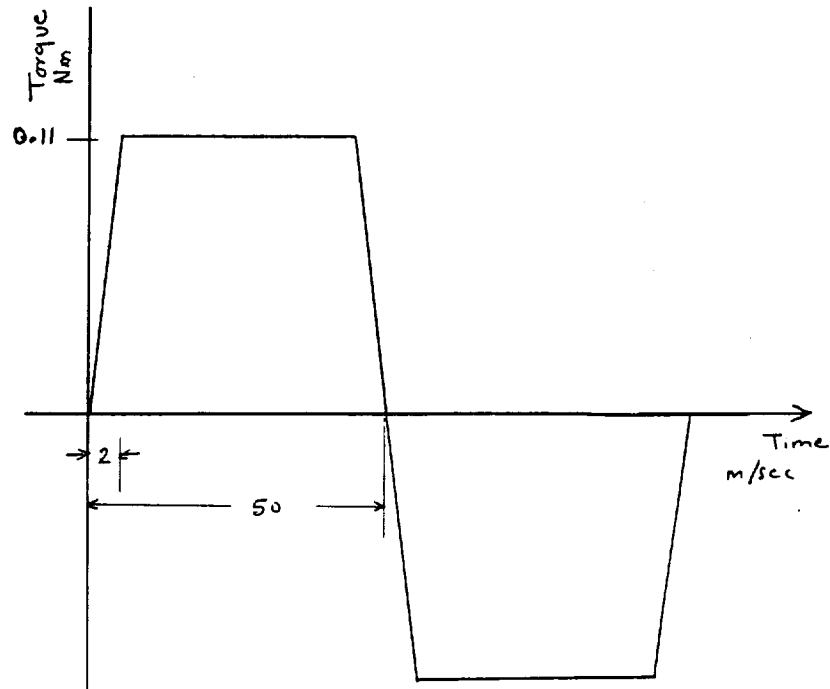


**Figure 5-4 Torque Profile Used to Model Motor Disturbance**

with the geometric center with resulting non-trivial cross products of inertia which introduces dynamic coupling between the 5 degrees of freedom even at the nominally central location.

Based on the nominal values of the bias flux density at the air-gaps and a mass distribution of the bearing without the linear optical encoder head, the open loop eigenvalues of the magnetic bearing are listed in Table 5.1 for the gravity conditions the bearing will experience.

Under zero gravity operating conditions and for small deviations around the operating point, the dynamics of the 5 degrees-of-freedom are decoupled except for the coupling introduced by the cross products of inertia. This allows the magnetic bearing controller to be designed as a set of 5 SISO loops for the 5 degrees of freedom. The cross-coupling which occurs when the bearing is at an off-center location is an important factor specially when considering behavior of the bearing at start-up/shut-down. This is studied as part of the non-linear simulation specially to confirm if a single compensation scheme is adequate for start-up from a corner as well as under normal operating conditions to give an acceptable dynamic performance.

**Table 5.1**

Degree of Freedom	Eigenvalues		
	lg Bias x	lg Bias z	0g Bias
x	3.4466e+02	2.4116e+02	2.3367e+02
	-3.4466e+02	-2.4116e+02	-2.3367e+02
z	2.4961e+02	3.0040e+02	2.7722e+02
	-2.4961e+02	-3.0040e+02	-2.7722e+02
$\theta_x$	7.9566e+01	1.2999e+02	1.1352e+02
	-7.9566e+01	-1.299e+02	-1.1352e+02
$\theta_y$	1.6107e+02	1.5214e+02	1.5122e+02
	-1.6107e+02	-1.5214e+02	-1.5122e+02
$\theta_z$	4.4553e+01	3.9860e+01	4.1787e+01
	-4.4553e+01	-3.9860e+01	-4.1787e+01
	[Eigenvalues in Radians/sec]		

### 5.2.1 Compensator Design

The compensator is essentially designed as 5 SISO lead/lag circuits in conjunction with an error integrator for regulation of the 5 degrees of freedom. Figure 5.5 shows a block schematic of the compensator scheme for regulating the x displacement.

The measurements from the sensors are transformed to the x displacement by the transform [T], x is the relative displacement between the suspended slide with respect to the bearing frame, X<sub>ref</sub> is the reference input for the x displacement. The sum of the integral of  $\epsilon_x$ , the error between  $x_{ref}$  and x measurement, and the output of the lead/lag compensator multiplied by the gain factor  $K_x$  is the control signal for x axis. The lead/lag compensation for all the SISO loops is set at 60Hz/800Hz but with different values of gains. The open loop transfer function for the x-axis displacement loop is shown in Figure 5.6. The designed cross-over frequency is 100Hz. The open loop transfer functions for regulating the rest of the degrees of freedom are similar. The sensitivity of these transfer functions to a lg bias either in the x or z axis is very small resulting in robust controllers.

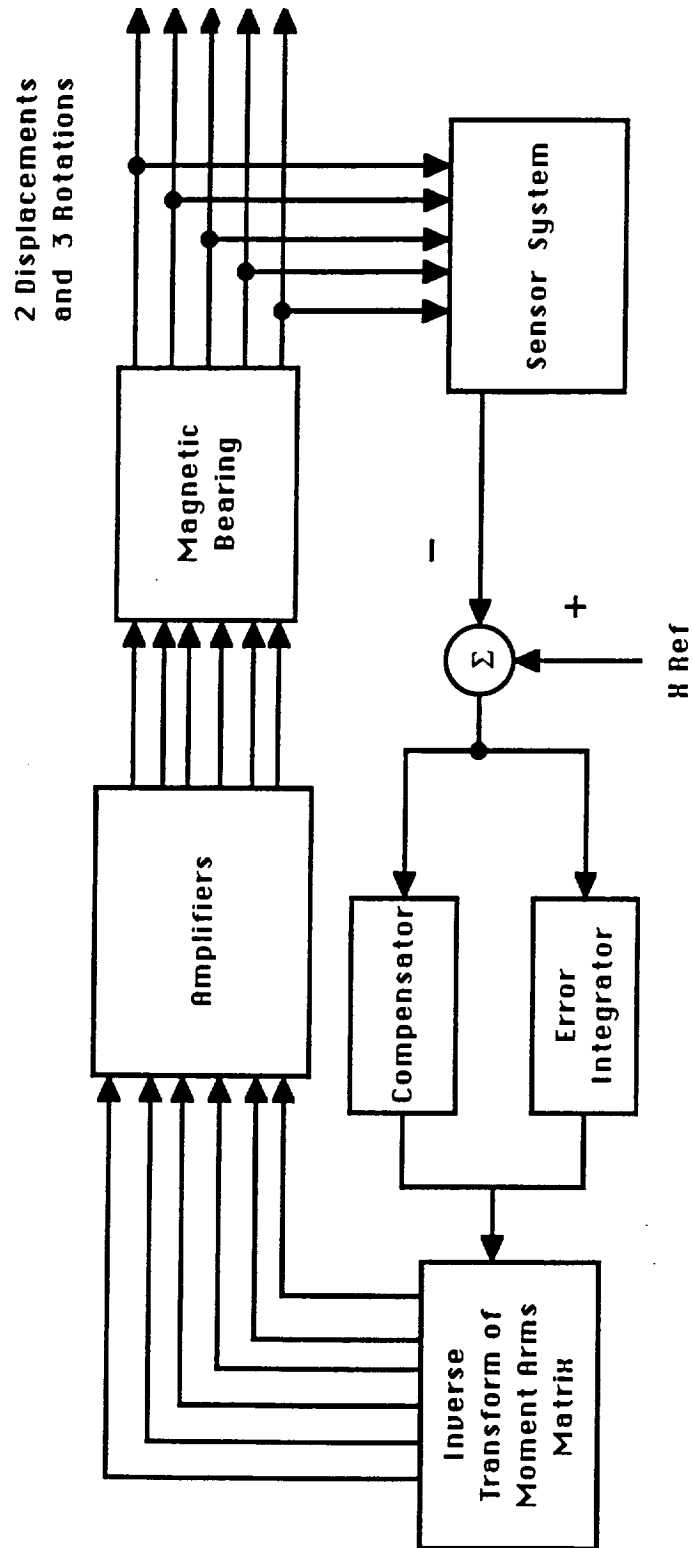


Figure 5-5 Block Schematic of the Compensation for the x Degree of Freedom

The compensation parameters, including the cross-over frequencies, may need to be modified for individual SISO loops depending on the structural resonances in the bearing and their influence on the stability of the 5 loops. This will be ascertained best on the bearing test bed.

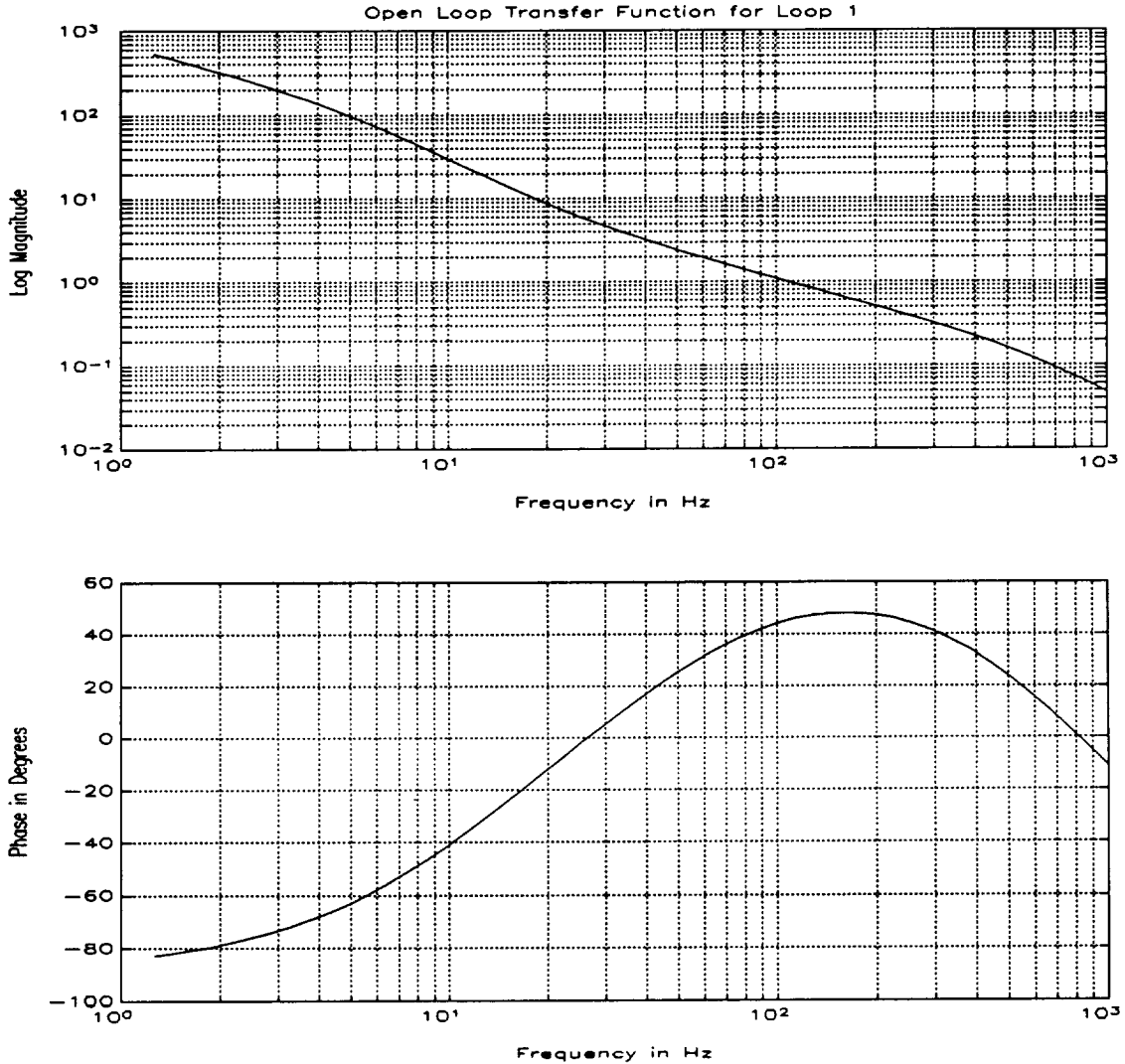


Figure 5-6 Open Loop Transfer Function for loop X.

An important issue considered in the linear analysis process is the gain variation and cross coupling introduced when the bearing slide is located away from its central location with respect to the frame. Both these reflect on the stability margins of the individual SISO loops and the overall controller. The approach taken to arrive at an acceptable controller design was to map the damping ratios of all the eigenvalues of the

closed loop system over the allowed range of travel for the slide and to establish that none of these was smaller than an arbitrarily set positive value. A more rigorous approach was not adopted as the cross-coupling and nonlinearities introduced at off-center locations could not be handled systematically. The non-linear simulation was used to ensure absence of limit cycles and other nonlinear destabilizing effects.

Figures 5-7 and 5-8 are representative examples of the shift in cross-over frequency of the open-loop transfer. Figure 5.7 shows the shift in cross-over frequency of loop x when the bearing has a 1g bias along the x axis. Slide locations  
 (i) corner A - maximum travel -50% nominal airgaps  
 (ii) corner D - maximum travel +50% nominal airgaps

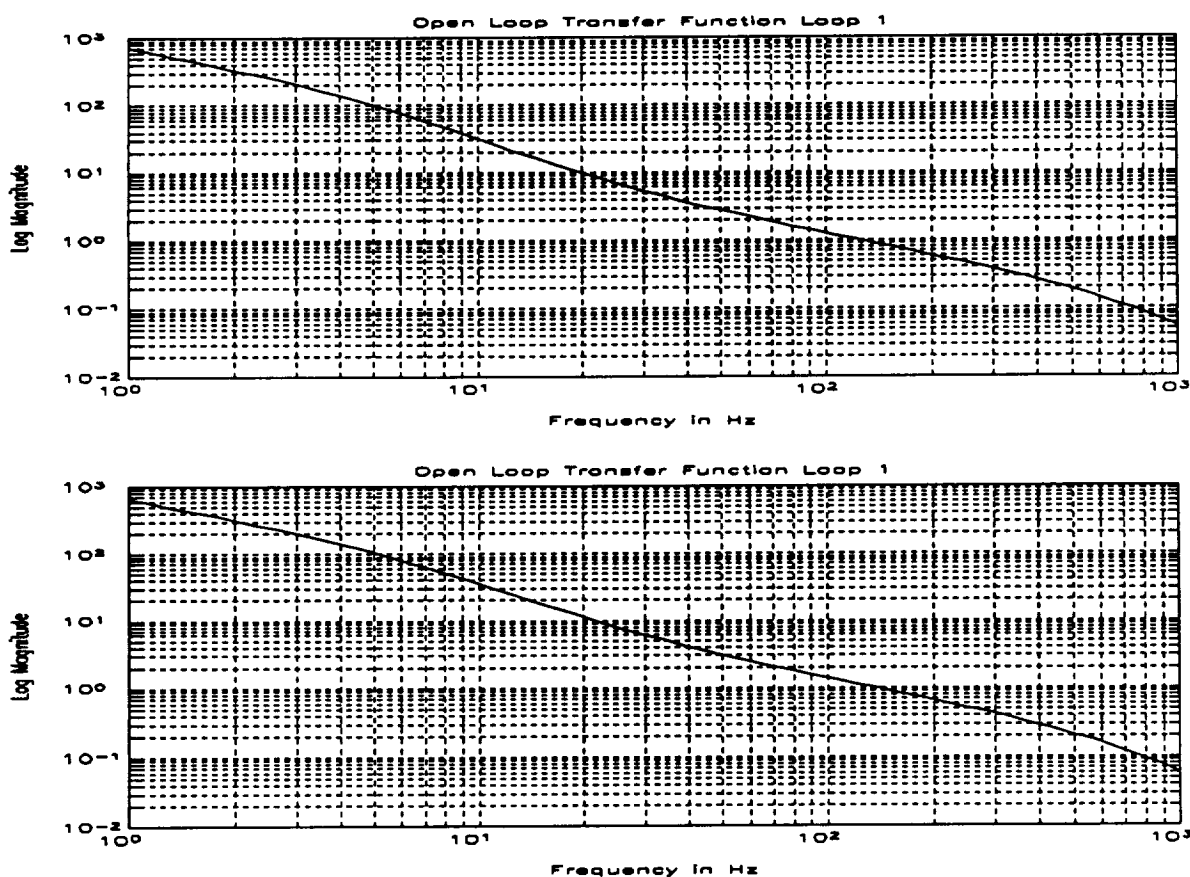


Figure 5-7. Shift in Openloop Crossover Frequency of X Loop

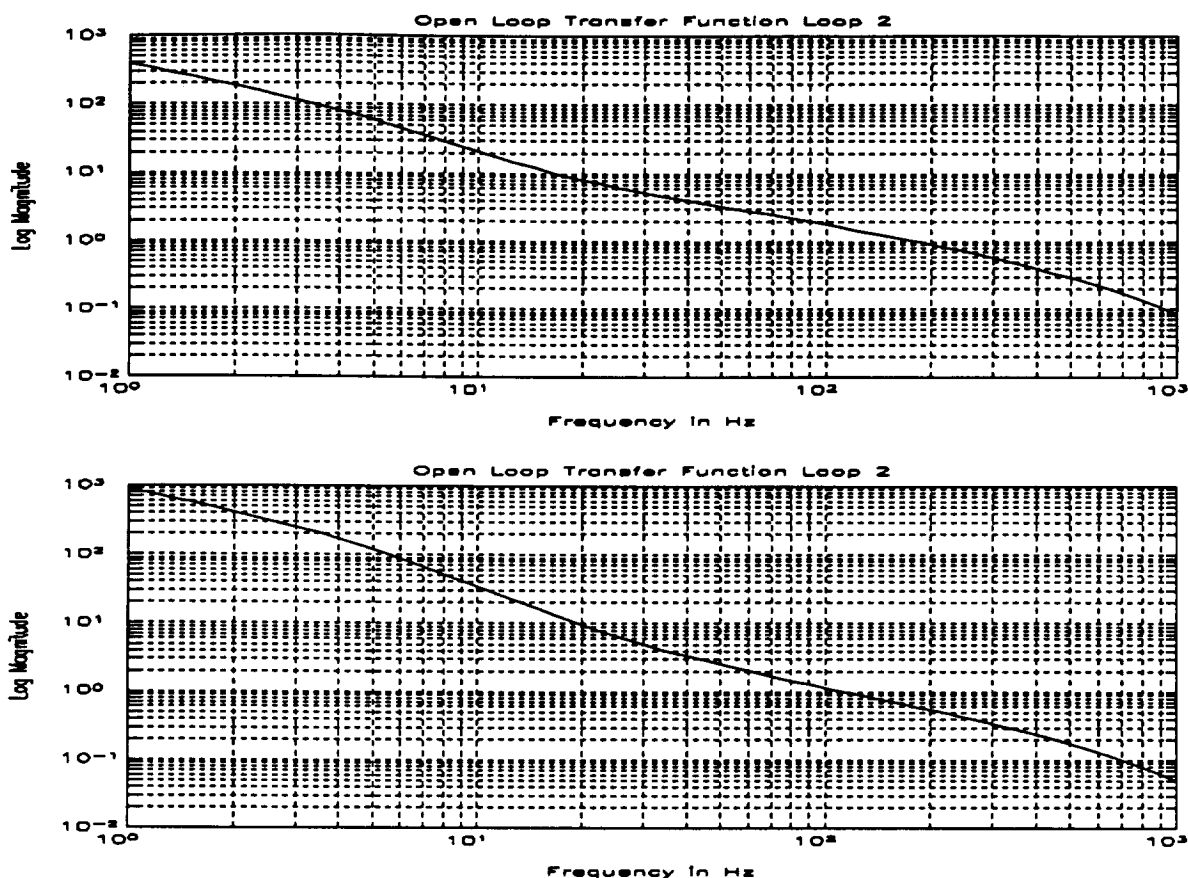


Figure 5-8. Shift in Openloop Crossover Frequency of Z Loop

The bearing controller has 6 control variables namely the currents  $I_{ac}$ ,  $I_{bd}$ ,  $I_{12}$ ,  $I_{34}$ ,  $I_{56}$  and  $I_{78}$  which result in 6 control forces  $Fx_{ac}$ ,  $Fx_{bd}$ ,  $Fz_{12}$ ,  $Fz_{34}$ ,  $Fz_{56}$  and  $Fz_{78}$ . However only 5 degrees of freedom  $x$ ,  $z$ ,  $\theta_x$ ,  $\theta_y$  and  $\theta_z$  are controlled. The compensation signals of the 5 degrees of freedom are transformed to the control currents using an inverse of the reaction arm matrix. The reaction arm matrix  $[R]$  is derived from the geometry of the bearing which transforms the 6 control forces to rigid body forces and moments  $Fx$ ,  $Fz$ ,  $M\theta_x$ ,  $M\theta_y$  and  $M\theta_z$ . The  $5 \times 6$  reaction arm matrix cannot be inverted directly. The Moore-Penrose generalized inverse is used to invert the reaction arm matrix.

### 5.3 Non-Linear Dynamic Simulation

The non-linear dynamic simulation is programmed in the simulation language ACSL which allows incorporation of user defined routines written in FORTRAN. ACSL allows a convenient means of solving for continuous systems described by a set of differential equations. Subroutines written in FORTRAN model the

non-linear characteristics of the magnetic bearing. The non-linear force model is described in Section 5.1.1 above.

The main features of the simulation are briefly listed below:

- (a) Nonlinear Magnet force model based on a linear solution of the coupled magnet circuits. A square law magnet flux to force relationship is assumed. The coupled circuit solution implicitly accounts for cross coupling terms in the spring and control coefficients.
- (b) The coil inductance is assumed to be a function of the effective air gaps across which the coil acts.
- (c) The amplifier is modelled as a 1 khz bandwidth small signal current feedback amplifier. Saturation limits on the drive voltage and the output current are implemented. The available drive voltages are bounded by

$$\begin{aligned} V_d &= V_{\max} - I \cdot R - \frac{I \cdot dL}{dt} \quad \text{positive limit} \\ V_d &= -V_{\max} - I \cdot R - \frac{I \cdot dL}{dt} \quad \text{negative limit} \end{aligned} \quad \text{Eq. (32)}$$

where  $|V_{\max}|$  is the power bus voltage,  $I$  the instantaneous load current,  $R$  the coil resistance and  $dL/dt$  the rate of change of inductance calculated as

where  $L$  is the inductance modeled as

$$L = L_0 + \frac{K}{G} \quad \text{Eq. (34)}$$

where  $L_0$  is a constant approximated to the leakage inductance and  $G$  is the effective air-gap of the inductance.

- (d) The mutual inductance between the various coils is not taken into account in the amplifier model i.e. the induced emf and the resultant effect on a coupled amplifier-coil combination is not modelled. This is justified by the assumed high bandwidth (1 khz) of the amplifiers. The effect on the available drive has been ignored.
- (e) The amplifier output current is limited to  $\pm I_{\max X}$  and  $\pm I_{\max Z}$ .
- (f) The slide is modelled as a rigid body with the center of mass at a given location not necessarily at the center of geometry. The geometry of the slide is described with respect to the center of mass i.e the location of the magnets and sensors is relative to the center of mass.

- (g) Collision between the suspended slide and the bearing frame are assumed to be elastic.
- (h) The simulation allows experimental data pertaining to a disturbance in the bearing frame location to be read in from a text file. This test data can be scaled and is introduced as a pseudo realtime input to the simulation.

The following "switches" are made available to change the model features on-line and to control certain outputs

LswVSet to 1 for a variable inductance model  
 LswFSet to 1 for a fixed inductance model  
 LswLdSet to 1 to incorporate  $dL/dt$  terms, else 0

WrOutD      If set .true. then the experimental data read in from a text file is displayed on the terminal.

WrOutC      If set true the air gaps at the time of a collision are printed out on the screen.

WrOutW      If set true the velocity of the slide before and after a collision is printed out on the screen.

The collision model used to simulate the collisions between bearing slide and frame is based in the following assumptions:

- (1) All collisions are elastic conserving both the total energy and linear/angular momentum.
- (2) The frame mass  $M_f$  is much greater than slide mass  $M_s$ .
- (3) The slide is assumed to be a thin i.e its z dimension/thickness is ignored.
- (4) Collisions are only along the x and z axis where the collisions along the x axis are on the face A, B, C or D and not at a point on this face and that collisions along the z axis are at the corners 1 to 8(refer to diagram above).
- (5) The above implies that
  - (a) a collision along the x axis will result in an instantaneous change in the x and  $\theta_z$  velocity components of the slide.
  - (b) and that a collision along the z axis will result in an instantaneous change in the  $\dot{z}$ ,  $\dot{\theta}_x$  and  $\dot{\theta}_y$  velocity components of the slide.

The complete derivation for this model is given in Appendix C.

#### 5.4 Start-Up/Shut-Down Procedure

A start-up/shut-down strategy is considered necessary for the magnetic bearing to ensure smooth transition between the two extreme conditions of bearing parameter variation when the bearing slide is located in one corner of the frame as against the nominally centered operating condition. This procedure is complicated by the necessity to design the controller so that the bearing is insensitive to the direction of gravity when being

tested under 1g conditions. The following assumptions were made to establish a start-up/shut-down strategy:

- (a) No "gravity-direction" sensing allowed
- (b) May start from the same corner each time
- (c) The shut-down procedure brings the bearing to rest in the same corner every time
- (d) The compensation may be changed when the bearing has passed from start-up to a nominally centered operating condition.
- (e) Signal cross-coupling may be added to cancel the bearing cross-coupling terms when starting-up.
- (f) The bearing may be started-up with suitable bias currents.

The start-up strategy adopted under the above assumptions is

- (a) Always startup from the corner  $-\Delta x, -\Delta z$  which are the extreme possible displacements along the negative x and z axes. Referring to figure 5.1 this position is corner 2.
- (b) Bias currents  $I_{\beta ac}, I_{\beta bd}, I_{\beta 12}, I_{\beta 34}, I_{\beta 56}, I_{\beta 78}$  are introduced such that the actuators exert zero force on the bearing slide. The forces on the bearing are solely due to gravity.
- (c) The control loops for regulating the x and z displacements of the bearing slide are given reference signals  $x_{ref}$  and  $z_{ref}$  which place it just slightly away from the start-up corner.
- (d) The reference signals  $x_{ref}$  and  $z_{ref}$  are ramped down to zero at a rate slow enough assure dynamic stability of the regulation loops.

## 6. POSITION SENSOR

The baseline position sensor selected during the first phase was a capacitive device from Mechanical Technology, Inc. Before designing the sensor into the magnetic bearing system, it was necessary to demonstrate its applicability to this measurement task. This effort involved sensor testing for magnetic-field sensitivity, design of suitable interface electronics, and sensitivity and linearity testing of the combined sensor/readout system using a laser interferometer.

### 6.1 Preliminary Sensor Testing

One of the first tasks undertaken in the phase II effort was the testing and evaluation of the capacitive sensors identified in phase I. The sensor, MTI model ASP-20-PCR, and associated electronics have a  $0.5 \mu$  resolution and  $500 \mu$  range specified. A testbed was designed to allow testing and calibration of the sensors in a configuration similar to the actual optical disk buffer. This testbed consisted of a mounting fixture for the sensor, a precision linear translator, and a silicon iron target piece. The target piece, made of the same material as the magnetic bearing shafts, was mounted to the linear translator and moved uni-directionally in  $10 \mu$  steps from over the range of the sensor ( $50$ - $500 \mu$ ). The voltage output of the electronics was taken and fitted to the best line. A graph of the position error versus range is shown in Figure 6.1. The graph shows substantial linearity deviation and error. This implied problems with either the sensor and/or the linear translator. Based on this data, it was decided to calibrate the sensors using a laser interferometer. This allowed the performance of the capacitive sensor itself to be tested independent of the translator. The preliminary testing also investigated the effects of magnetic fields on the sensor. A pole piece (Satcon PN 1009-101) was fabricated for this purpose. Fitting on top of the target piece, the pole piece was wound with 30 turns of 22 wire to produce large target magnetic fields. Additionally, permanent magnets were used to produce magnetic fields in and around the capacitive sensor itself. Testing showed magnetic fields to have no discernable effect on the sensors.

### 6.2 Interface Circuit Design

The capacitance of the position sensor varies inversely with the distance from the sensor to the target. Over the specified measurement range, the sensor varies in capacitance from approximately  $0.35$  picofarads (pF) to  $3.5$  pF. Any stray capacitance on the sensor leads will effect the linearity of the measurement unless the leads are appropriately guarded. The ability to detect position accurately is also hampered by any load placed on the sensor capacitance by the measurement electronics.

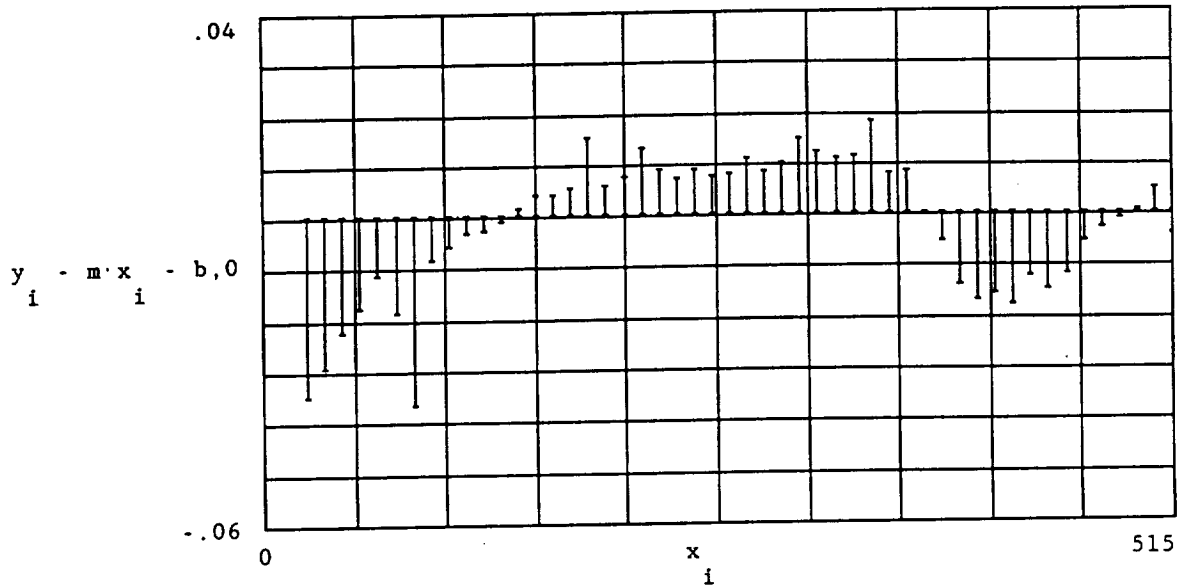


**Figure 6-1. Sensor Position Error**

The block diagram of the capacitive sensor interface circuit is shown in Figure 6.2. The sensor is driven by a 16 kHz current source so that the resultant voltage is proportional to the sensor impedance. The AC voltage produced across the sensor is buffered by a "guard" loop, full-wave rectified, and low-pass filtered to produce a DC output voltage directly proportional to distance. The effects of stray capacitance on the sensor leads are greatly reduced by driving the shield of the sensor cable with a "guard" loop. The guard loop drives the shield with a voltage identical to that across the sensor, and thus no current flow is possible. The impedance of the shield is a capacitance greater than 200 pF to ground. In order to drive this load, the voltage across the sensor is buffered by the FET input stage, a high-bandwidth differential op-amp, and a high-current buffer. The bandwidth of this follow-up loop must be high to reduce any effects of the guard capacitance upon the sensor capacitance.

The schematic of the sensor interface electronics is shown in Figure 6.3. To reduce the input capacitance of the sensor electronics, a Field Effect Transistor (FET) input stage is used. This input stage presents a very high resistance and low capacitance load to the sensor. The FET input stage is configured as a source-follower where the source signal will exactly follow the gate (input) signal. The source terminals of

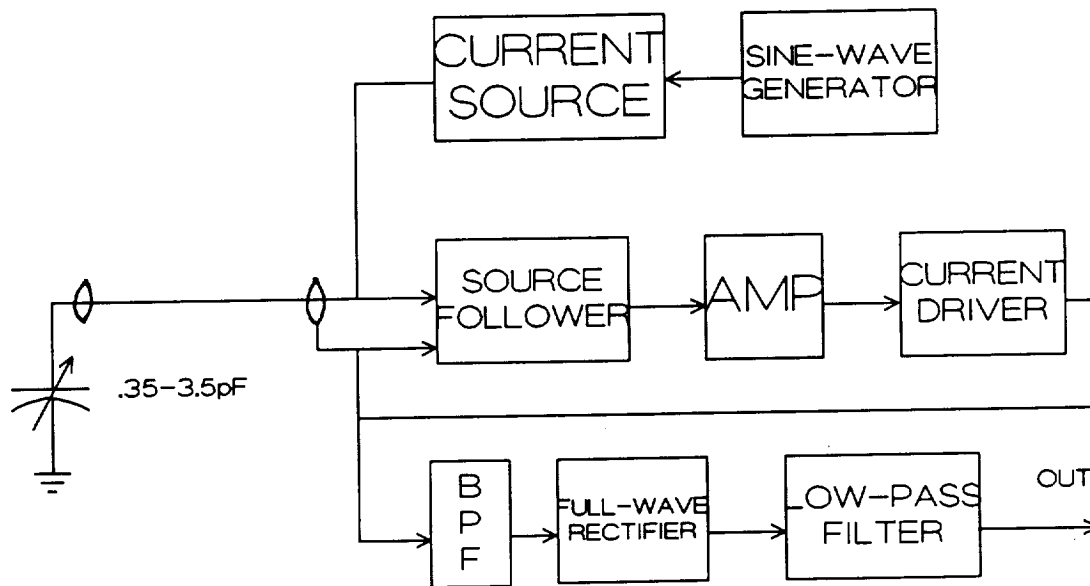


**Figure 6-2. Sensor Interface Block Diagram**

the FETs are each loaded with a transistor current source. The high impedance of the current sources reduces the effect of any gate-to-source capacitance. The drain of the FETs are capacitively coupled to the buffered sensor voltage to reduce the effects of any gate-to-drain capacitance. Stray capacitance on the circuit board is reduced by placing the buffer-loop circuitry on a copper-clad board with the copper clad driven by the guard voltage. This circuit is also placed within a metallic box connected to guard loop. The copper clad and box act like part of the shield in helping to reduce stray effects. The output of the sensor guard-loop is bandpass filtered to eliminate both DC drift and high-frequency noise effects. The signal is then full-wave rectified and low-pass filtered to produce a DC output voltage. The filter is a four-pole Butterworth with a corner frequency of 2 kHz, and contributes less than 10 degrees of phase error at 100 Hz. A plot of the ideal amplitude and phase characteristics is shown in Figures 6.4 and 6.5.

### **6.3 Interferometer Tests**

Testing of the sensor electronics was done using the laser interferometer test setup shown in Figure 6.6. The laser interferometer has an accuracy of .025 microns.

The capacitor sensor target and laser interferometer test-surface were mechanically attached to each other. The target and

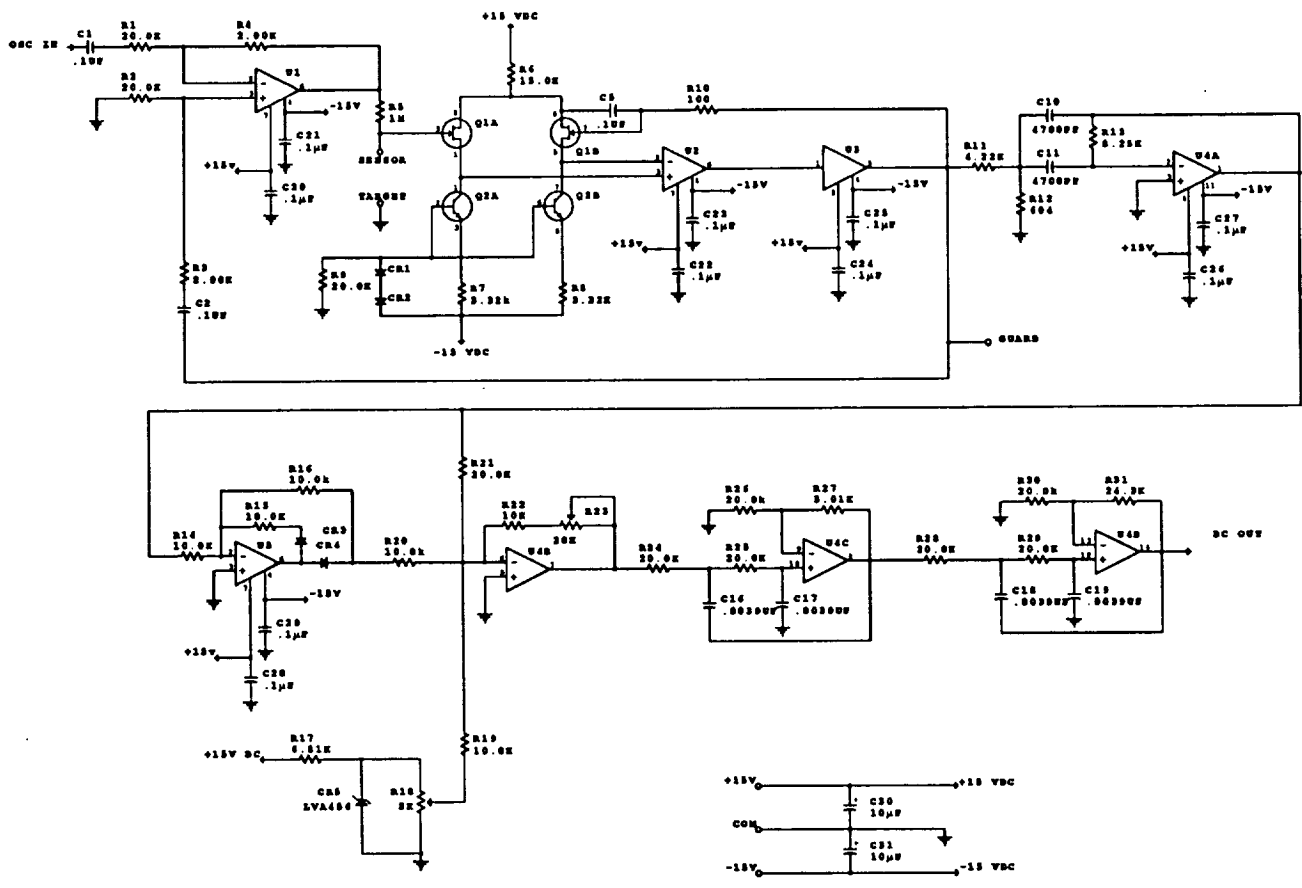
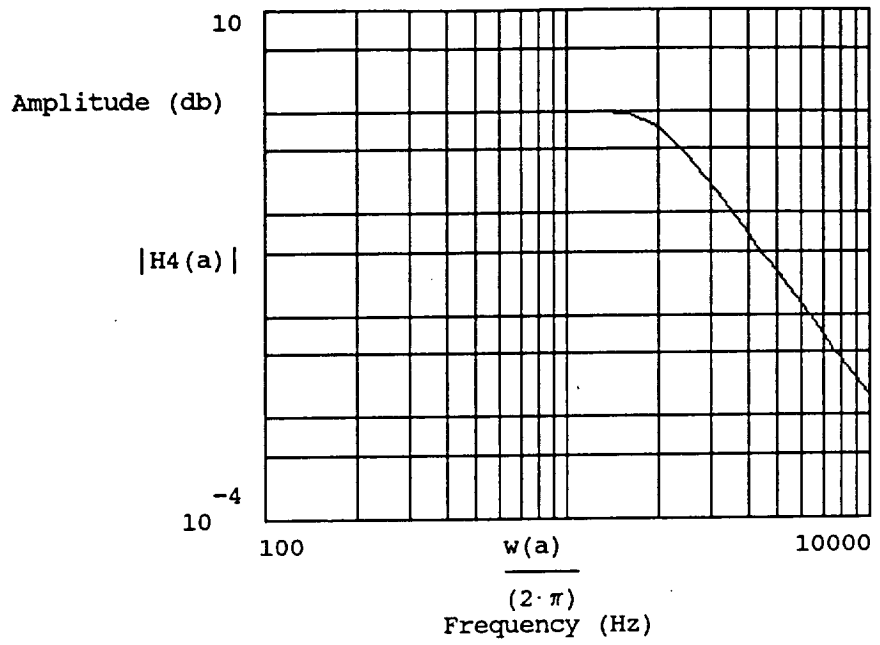
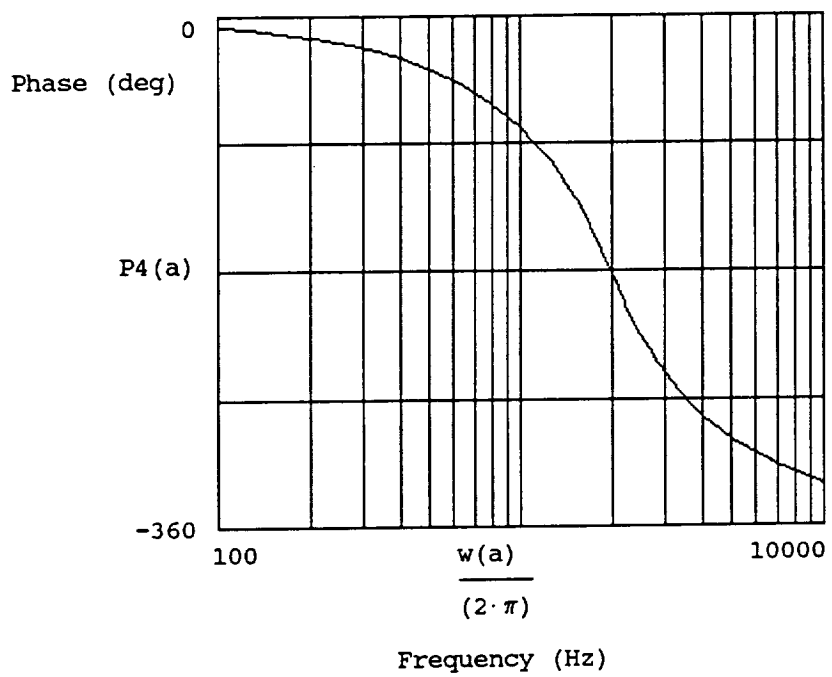


Figure 6-3. Capacitive Sensor Interface Electronics



4 Pole Butterworth Amplitude Response



4 Pole Butterworth Phase Response

Figure 6-4. Figure 6-5.

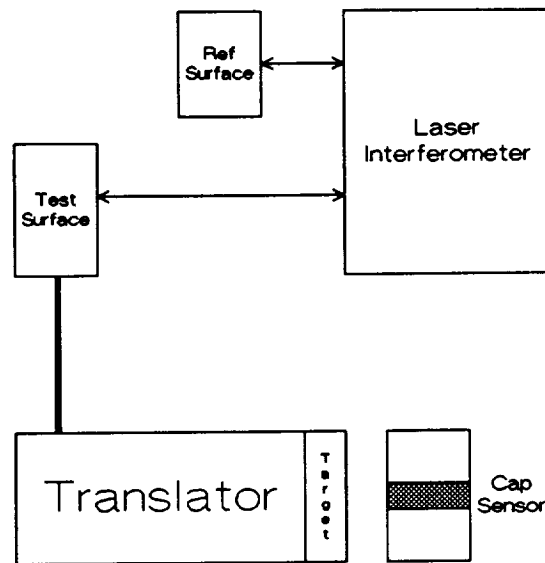


**Figure 6-6. Capacitor Sensor Test Setup**

test surfaced were move using the translator. A plot of the sensor output voltage vs position as indicated by the laser interferometer is shown in Figure 6.7.

As shown in Figure 6.8, the sensor electronics have a linearity of  $\pm 5\%$  over the full range of the sensor. The operating range that the optical disk bearing will require is approximately 250 microns  $\pm 100$  microns. The sensor electronics has a linearity of  $\pm 1.5\%$  over this range.

#### **6.4 Sensor Electronics Noise**

During the course of testing, it became apparent that the noise inherent in the sensor interface electronics would need to be reduced. This reduction was required because the large amount of forward loop-gain in the  $\theta_2$  control loop amplified the sensor noise to the point that the voltage resulting across the control coils was actually saturating the coil driver output stage. The  $\theta_2$  loop requires approximately ten times the forward loop-gain of the other control loops because of the relative shortness of the distance between the actuators as compared to the moment of inertial.

Investigation of the cause of the electronics noise revealed two predominant sources. Referring to Figure 6.3, these sources are the sense resistor in the excitation-current source (R5,  $1\text{M}\Omega$ ) and the high-bandwidth op-amp in the guard loop (U2, HA2544). The noise produced at the output by R5 could be reduced by

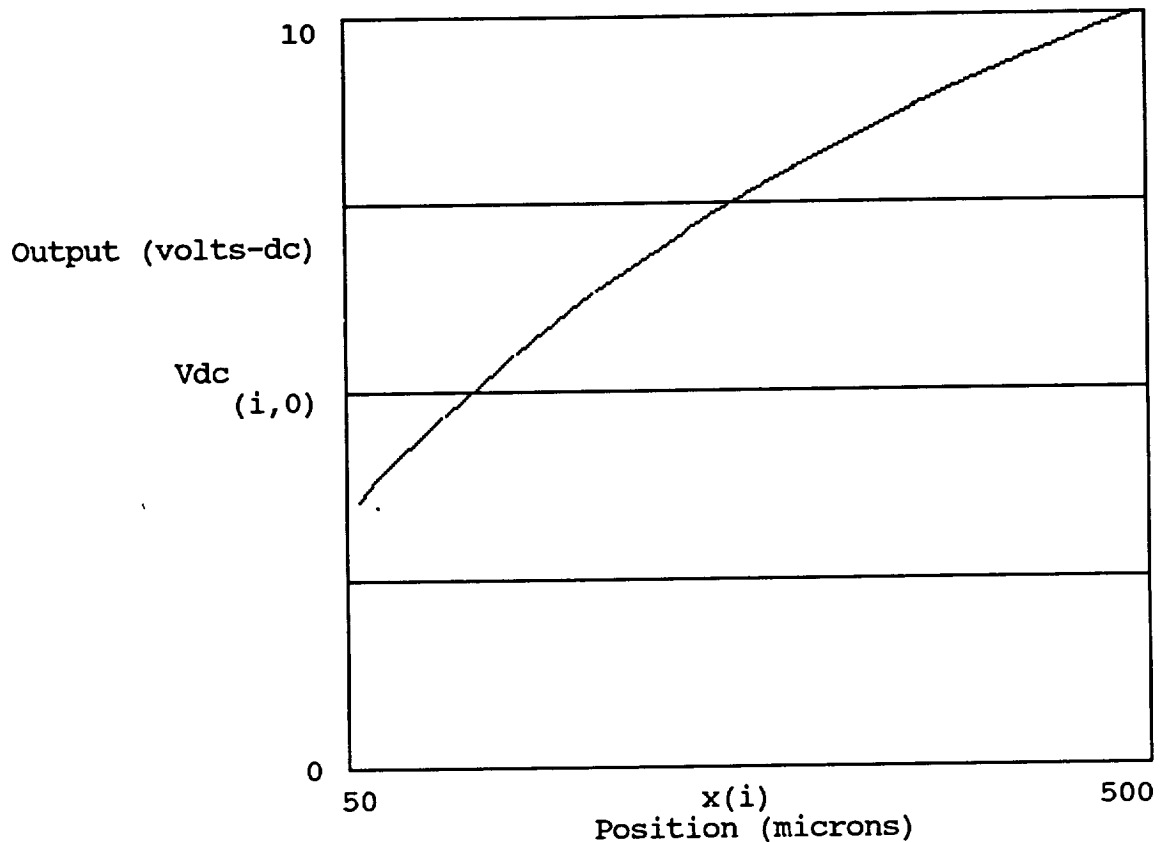
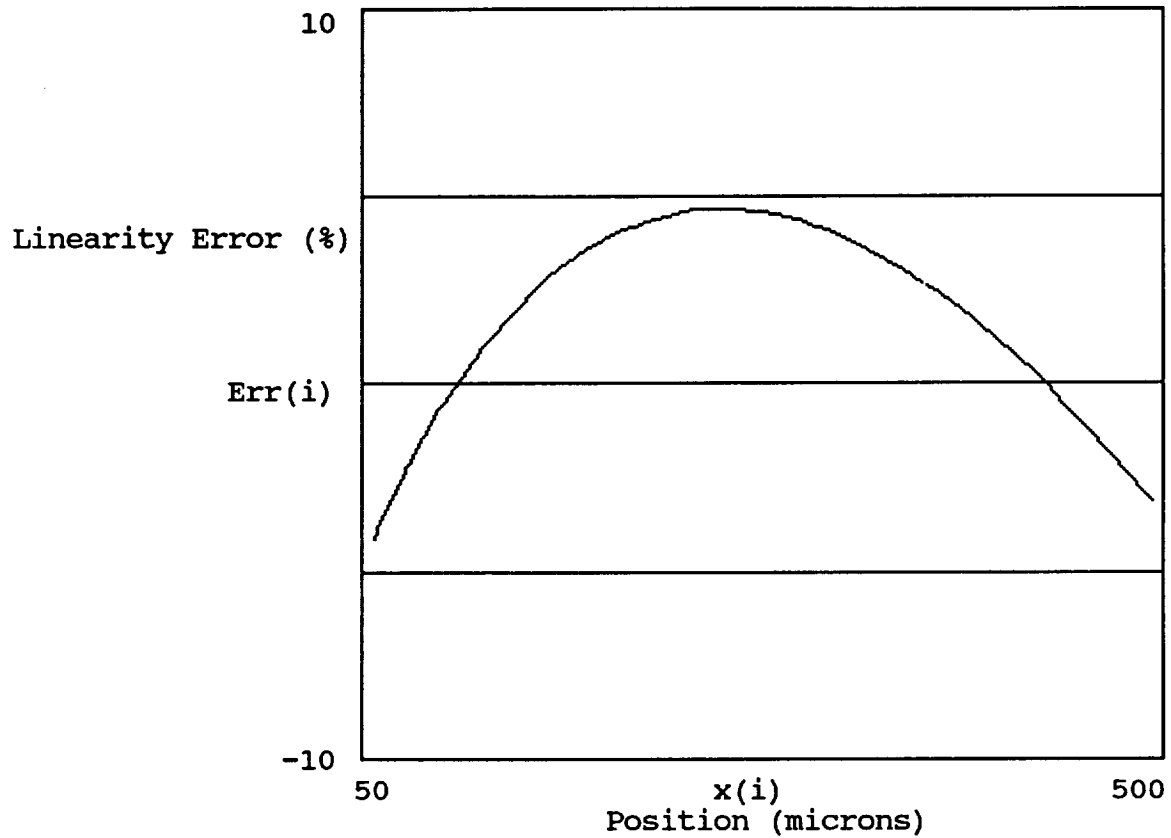


**Figure 6-7. Capacitor Sensor Output vs Position**

approximately a factor of five by changing  $R_5$  to  $10M\Omega$  and  $R_3$  and  $R_4$  to  $20K\Omega$ . Unfortunately, the noise produced at the output by  $U_2$  is actually 40% larger than that produced by  $R_5$  and thus both sources must be reduced for a significant net decrease. Because low-noise version of  $U_2$  could not be found, a different approach was taken to noise reduction, i.e., an increase in sensor signal. This was achieved by increasing the amplitude of the input to the voltage-to-current converter ( $U_1$ ) and thereby increasing the drive current to the sensor by a factor of five. This allowed a decrease in the circuit gain after the full-wave rectifier and resulted in a factor of five reduction in noise. The penalty for this approach is that the full-scale range of the interface circuit is reduced to about 0.42mm, but, since the maximum range required in this system is 0.4mm, this was felt to be a worthwhile compromise, especially since it required changing only one component in each channel ( $R_{22}$ ).



Capacitor Sensor Electronics Linearity Error

Figure 6-8. Capacitor Sensor Electronics Linearity Error

## 7. ELECTRONIC DESIGN

The support electronics required for the magnetic bearing system include the control electronics, the start-up circuit, and a circuit to protect the actuator coils from overheating. The design of each circuit is discussed in the following sections.

### 7.1 Loop Decoupling

The mechanical hardware for the magnetic bearing system employs eight position sensors and six control coils. The control algorithm is most easily analyzed and designed in terms of the five decoupled degrees-of-freedom in an orthogonal coordinate frame. This allows implementation of the algorithm with five independent single-input, single-output compensation networks. Decoupling of the orthogonal degrees-of-freedom is accomplished mathematically through the use of a matrix manipulation called the pseudo-inverse. The prefix "pseudo" is used because only a square matrix has a true inverse, whereas the two matrices which describe this system are 8x5 and 5x6. Implementation of the pseudo-inverses of these matrices is accomplished by resistor summing networks which weigh the outputs of the eight sensors and the inputs to the six coils. In a system where the sensors and actuators were located symmetrically about the center-of-mass, the weightings would all be equal and the loops would be inherently decoupled. Due to the unfavorable center-of-mass location of the translator, the weighing resistors are seriously imbalanced. This results in reduced total-forced capability since only a small fraction of the capability of some actuators is available.

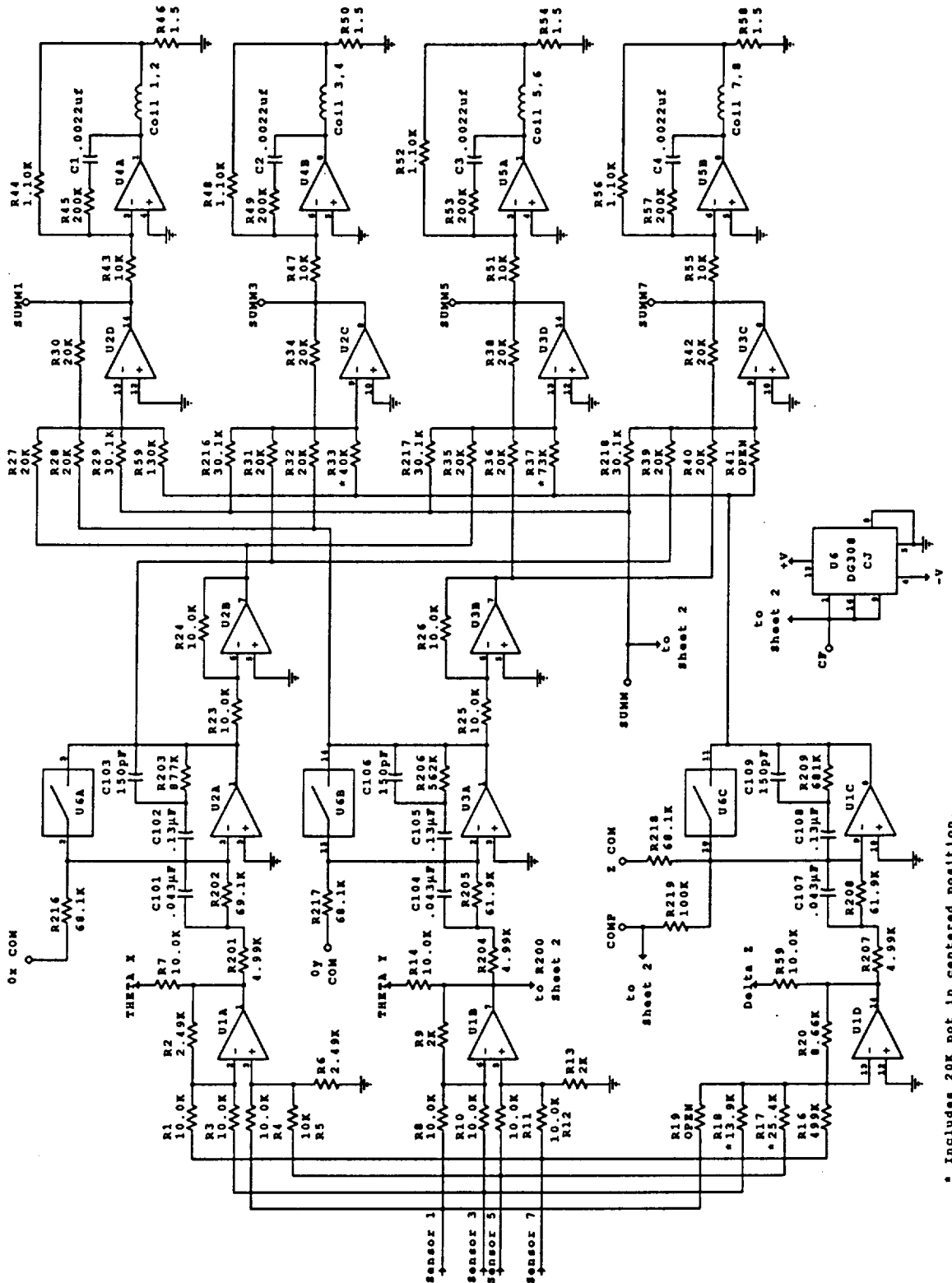
### 7.2 Control Electronics

The schematic of the control electronics is shown in Figure 7.1. The front end of the control electronics consists of a summing and difference stage which decouples each of the degrees-of-freedom. With reference to Figure 7.2 for the location of the capacitor sensors and the actuators, the five degrees-of-freedom are decoupled using the following signs:

$$\begin{aligned}\theta_x &= [S_1 - S_3] + [S_5 - S_7] \\ \theta_y &= [S_5 - S_1] + [S_7 - S_3] \\ \theta_z &= [S_A - S_C] + [S_D - S_B] \\ X &= [S_A - S_C] + [S_B - S_D] \\ Z &= -[S_1 + S_3 + S_5 + S_7]\end{aligned}\tag{Eq. (35)}$$

The resistors indicated by the asterisks include a 20K $\Omega$  potentiometer which is used to adjust the sensor "moment arms" and thereby decouple the loops.

The control-loop compensation follows the input summing stage. The actual control-loop compensation algorithm is implemented with a single op-amp stage in each loop. The



\* Includes 20K pot in centered position.

Figure 7.1 ODB Control/Power Electronics

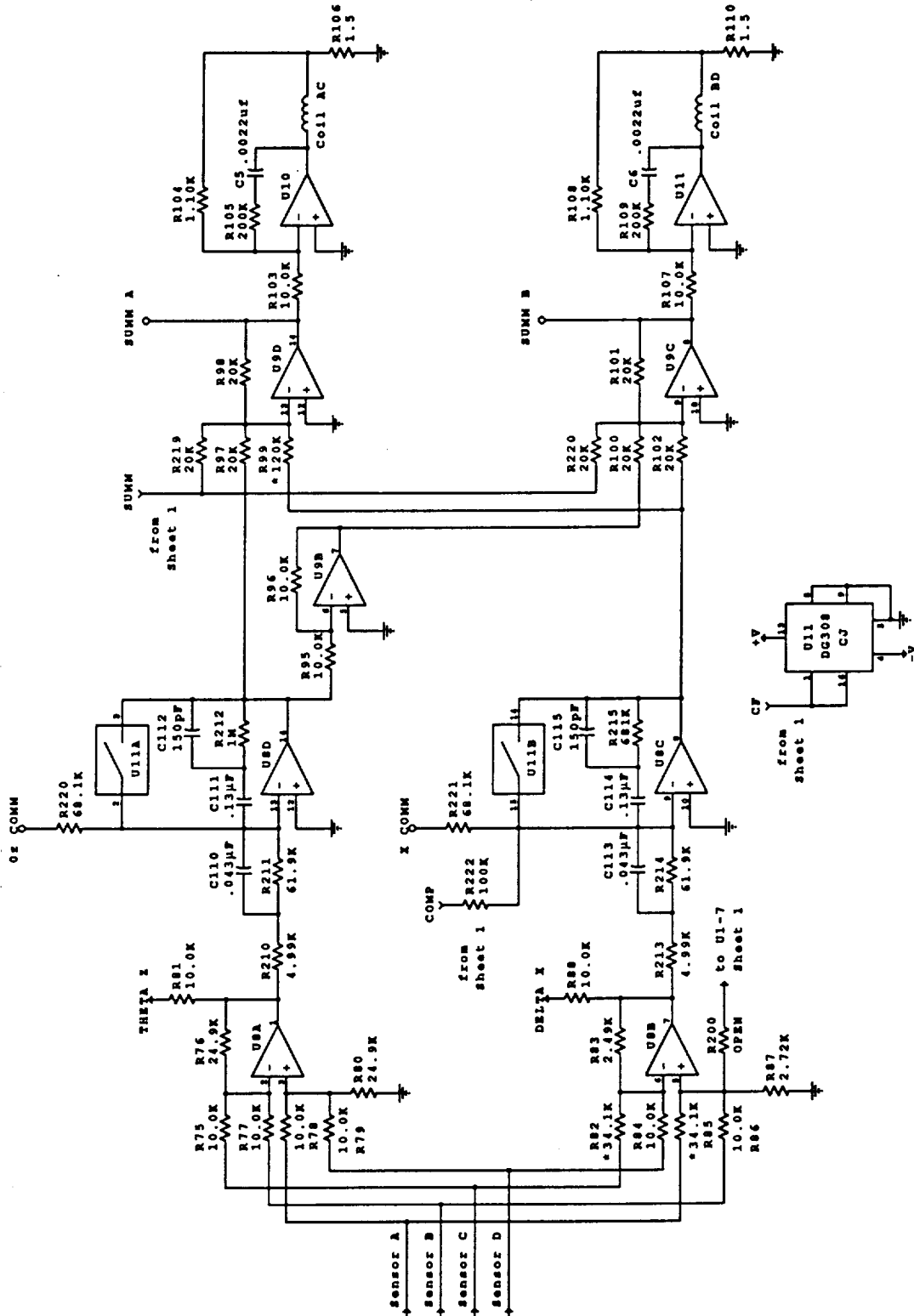
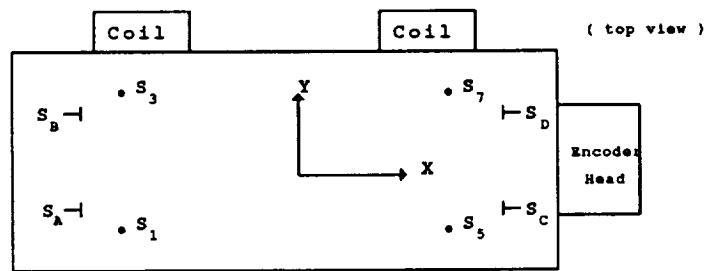


Figure 7-1 (continued)

\* Includes 20K pot in centered position.

### Sensor Orientation



### Coil Orientation

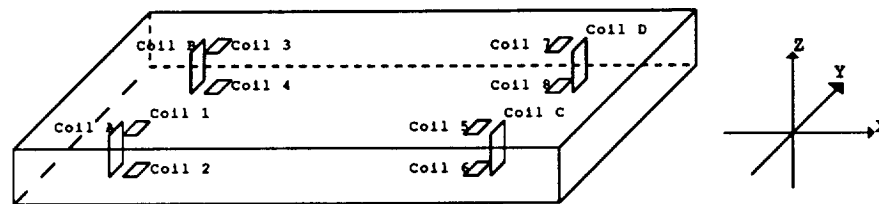


**Figure 7-2 Nomenclature Used for Identifying Bearing Locations**

integrator and the zero which cancel it are implemented with the series R-C feedback network. The zero which provides the lead compensation and the pole which cancels it are implemented with the parallel R-C, series R input network. The additional feedback capacitor provides roll-off of the gain at high frequencies for noise reduction.

Following the compensation stage is a second summing stage which combines the five degrees-of-freedom to determine the resulting force that each of the actuators must produce. The five degrees-of-freedom are combined to produce currents in the actuator coils using the signs as follows:

$$\begin{aligned}
 I_{12} &= \theta_x - \theta_y - Z \\
 I_{34} &= -\theta_x - \theta_y - Z \\
 I_{56} &= \theta_x + \theta_y - Z \\
 I_{78} &= -\theta_x + \theta_y - Z \\
 I_{AC} &= \theta_z + X \\
 I_{BD} &= -\theta_z + X
 \end{aligned}
 \tag{36}$$

The power stage which drives the current to the actuators consists of a power amplifier in a voltage-to-current converter topology. The output current to the actuator coil is sensed

through the  $1.5\Omega$  resistor. The voltage produced across the sense resistor is fed back to the amplifier to provide a linear conversion from input voltage to output current. An integral-plus-lead configuration is used in the feedback path for stability. With the indicated values, the circuit will have a bandwidth of 2 KHz with a phase margin of 45 deg. A plot of the measured closed loop amplitude and phase response for the current driver is shown in Figure 7.3.

### 7.3 Start-Up Circuit

The start-up circuit actually performs three functions:

1. Closes the control loops using the defined start-up procedure,
2. Opens the loops by reversing the start-up procedure,
3. Automatically cycles through opening and closing the loops if any coil current exceeds the maximum (2g) value for more than 2 seconds.

This last function protects the current sources and control coils against overheating should the control loops "latch-up." The actual steps implemented for the start-up procedure are:

1. Inject full current in the control coils so as to pull the translator to the -x, -z corner.
2. Change the coil currents to those bias values which will result in no force on the translator from the actuators.
3. Zero the compensator integrators.
4. Close the loops with a commanded position slightly out of the --x, -z corner.
5. Change both the bias current and commanded position to zero.

Each step in the sequence lasts for one full second and the changes in value take place with an exponential time-constant of 0.1 second.

The schematic of the start-up circuit is shown in Figure 7.4. The circuitry in the upper-left corner senses the commanded coil currents and detects an over-current lasting more than 2 seconds. The circuitry in the upper-right corner generates the one second timing and provides the decoding to enable each of the five separate steps. This circuit is controlled by the front-panel "Control Loops: Open/Closed" switch which can be overridden by the over-current projection. The circuitry in the lower-left corner generates the exponentially changing voltages for both the coil currents and the commanded position.

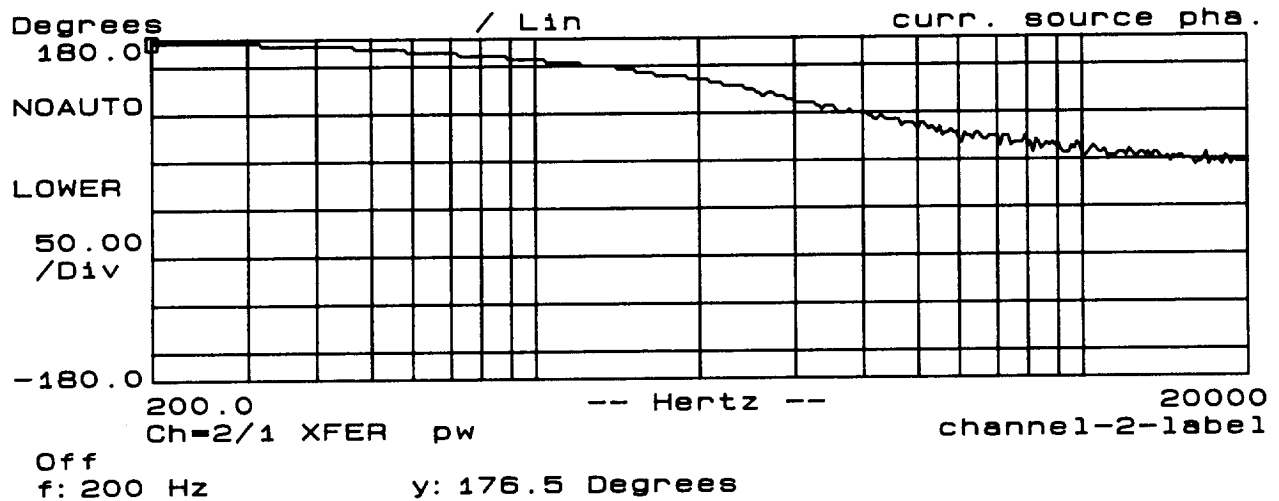
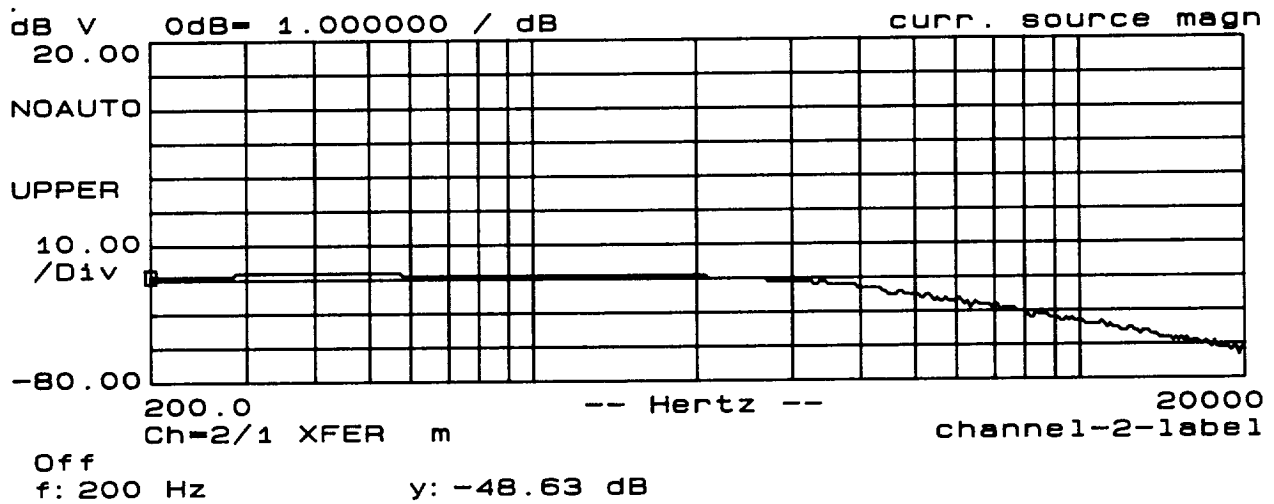


Figure 7-3. Current Dirver Amplitude and Phase Response

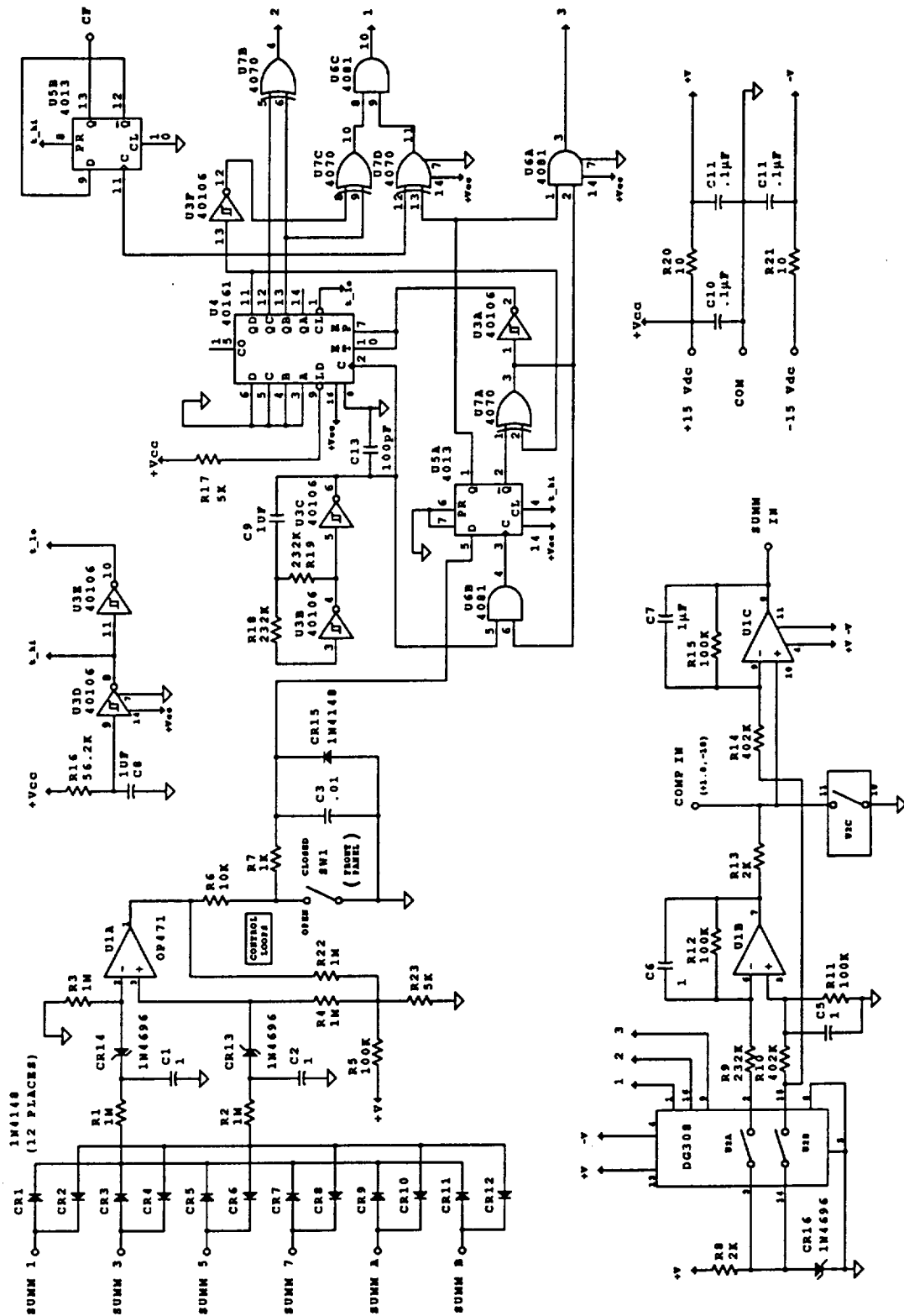


Figure 7-4. Start-Up Circuit

## 8. FABRICATION AND ASSEMBLY

All hardware projects must make the step from design to reality. Usually, it is more difficult than expected, and this project was no exception. Though no insurmountable problems were encountered, fabrication problems cost several weeks delay.

Most of the part fabrication problems were the result of vendor errors. Though SatCon's first vendor delivered the high precision frame with 0.1 mil tolerances acceptably, the less difficult pole pieces were made improperly three times. The extensive stress relief required for optimum magnetic properties made re-work time consuming and expensive because only limited machining may be done afterwards. The heat treatment also makes the magnetic material mechanically softer and more delicate. This is especially true of the Hy-Mu80 pole pieces. Eventually, another vendor was contracted to fabricate the delivered pole pieces.

Another area of some difficulty was coil winding. The pole pieces were designed as two parts to facilitate separate winding of the X and Z control coils. This made winding easier, but mechanical re-assembly to specification difficult. As shown in SatCon drawing 1009-111A, the pole pieces were located relative to each other with dowel pins and held with a #2-56 bolt. The disassembly and assembly during the winding process deformed the holes slightly, degrading the parallelism of the X axis pole faces required by Satcon drawing 1009-210. A light surface grinding restored the flatness, but future designs could improve this feature.

Assembly of the frame and carriage caused no major problems, but was not an easy task. The linear motor magnets on the frame produced large difficult to control attractive forces between the frame pieces. This problem was overcome by use of a fixture made by GE for assembly of their frame. The fixture held the center portion of the frame stationary and moved the magnets and flux return bars with a lead screw. Correct assembly of the carriage proved to be delicate. Shims were used to set the appropriate X axis gaps, the carriage was bolted together, and the shims removed. The shims had a tendency to compress and the pole pieces to shift slightly, however, and several trials were needed.

A disadvantage of the linear bearing design is the necessity of having sensor and power leads coming off the suspended carriage. Lead dress was therefore an important consideration. The control coil and sensor leads were run beneath the stiffening

plate, 1009-304. The control leads were attached to 30 gauge stranded leads beneath the stiffening plate and stress relieved with silicone gel. The control, sensor, and linear motor leads exited the translator carriage at top and bottom and bundled with the sensor grounding strap into an umbilical for connection to the electronics box. Though the stiffness of the lead bundle can be felt in the linear translator motion, its effect is small.

## **9. INTEGRATION AND TEST**

### **9.1 Center-of-Mass Location**

In order to balance the forces and torques produced by the magnetic actuators, it is necessary to know the center of mass of the suspended translator carriage. In 1986, GE performed finite element studies of the original translator design. This provided an initial estimate of the center of mass, but changes made to the carriage design by GE and the magnetic bearings added by JDI necessitated a revised estimate. A new estimate was found by assembling all of the translator parts together with "dummy" masses for the optical head, linear encoder head and pole pieces. The assembled translator was balanced on a "knife edge" in three orthogonal axes, thus pinpointing the center of mass. The measured location is shown in Figure 9.1, which indicates that the center of mass is significantly removed from the center of force application.

### **9.2 Force Test Fixture Design**

The relationships describing the force/current/gap characteristics of the Z- and X-axis bearings were developed through the use of a static force test fixture. This fixture holds both the translator frame and the carriage assembly in a known and fixed relative position allowing the magnetic gaps to be varied. Force/current information results from varying the current to the bearing coils and reading the resulting force vectors.

Figure 9.2 presents an assembly drawing of the test fixture with the frame and translator in place. A base plate (SatCon PN 1009-219) provides a location for mounting the translator frame to three Kistler force transducers. An adapter rail (SatCon PN 1009-218) was required to provide suitable mounting for the force sensors per the manufacturer's recommendations. During testing, the base plate assembly was mounted to the table of a milling machine, providing a massive, precision positioning system, allowing accurate variation of the gaps.

The carriage assembly is mounted to a support (SatCon PN 1009-303) which is fixtured to the spindle quill of the milling machine. The quill (which contains the bearings in which the milling machine spindle rotates) was found to be very stiff and have no significant axial or radial play, a critical requirement for producing accurate changes in the gaps.

Additionally, in order to retain the gaps at higher current levels and at higher frequencies, the whole test bed assembly, which includes the milling machine as well as both fixturing assemblies, must have no resonances below the maximum test frequency of roughly 1000 Hz. Structural resonances in the test

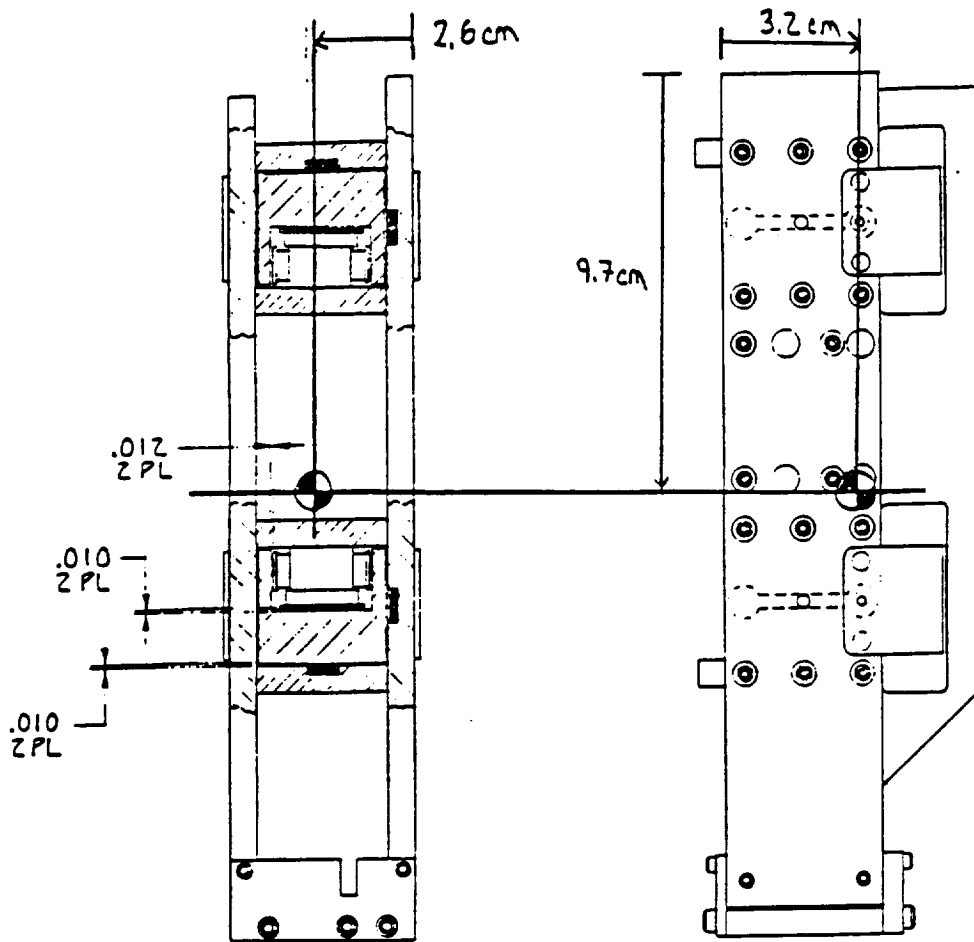


Figure 9-1. Measured Center-of-Mass Location

fixture were not noticed in testing.

Drawings for the remainder of the force test fixture mechanical components can be in Volume II and are as follows:

- 1009-112 Force Sensor Bushing
- 1009-216 Frame Mount, Left
- 1009-217 Frame Mount, Right
- 1009-218 Adapter Rail, Force Sensor
- 1009-219 Base Plate
- 1009-303 Mount, Translator Carriage
- 1009-310 Adapter Collar, Force Test Fixture

### 9.3 Test Plan

#### I. Open Loop Testing

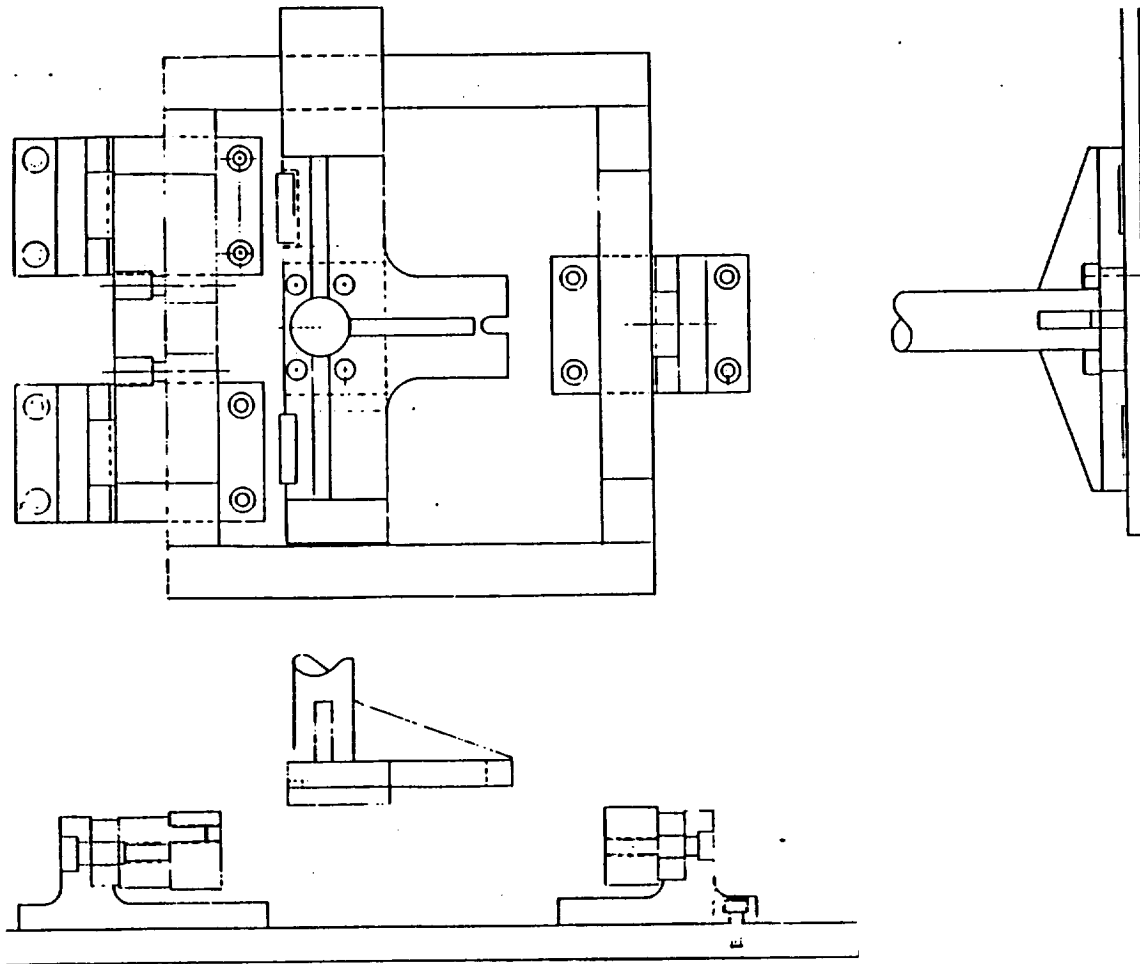


**Figure 9-2. Bearing Test Fixture Layout**

- A. Mount translator/frame assembly into force-test fixture.
- B. Locate translator for equal air-gaps at each pole face:
  1. Eight z-axis pole faces (1-8) (0.012 in.)
  2. Four x-axis pole faces (A-D) (0.010 in.)
- C. Connect each position sensor to its appropriate interface circuit. Adjust the offset potentiometer of each sensor interface circuit for zero volts  $\pm 10$  mV

DC output. Measure the RMS voltage of each output in the band from 0.01 to 100Hz:

1. V(A) 5. V(1)
2. V(B) 6. V(3)
3. V(C) 7. V(5)
4. V(D) 8. V(7)

Observe that there are no spectral peaks below 1000Hz with amplitude larger than 6db above the sensor noise floor.

D. Measure air-gap flux density at each pole face:

1. B(A) 7. B(3)
2. B(B) 8. B(4)
3. B(C) 9. B(5)
4. B(D) 10. B(6)
5. B(1) 11. B(7)
6. B(2) 12. B(8)

E. Measure resistance of each coil pair:

1. R(A,C)
2. R(B,D)
3. R(1,2)
4. R(3,4)
5. R(5,6)
6. R(7,8)

F. Measure inductance of each coil pair:

1. L(A,C)
2. L(B,D)
3. L(1,2)
4. L(3,4)
5. L(5,6)
6. L(7,8)

G. Measure the DC output voltage of each sensor interface circuit:

1. V(A) 5. V(1)
2. V(B) 6. V(3)
3. V(C) 7. V(5)
4. V(D) 8. V(7)

H. Inject 100mA peak sinewave of current at 10Hz into coil pairs (A,C) and (B,D).

J. Measure the peak forces and torques:

1. Net x-force
2. Net z-force
3. Net  $\theta_x$ -torque
4. Net  $\theta_y$ -torque
5. Net  $\theta_z$ -torque

K. Increase the frequency of the current sinewave until the force or torque force specified below lags the

current by 45 degrees, and measure the frequency.  
Return the frequency to 10Hz.

- Step H: Net x-force
- Step L: Net  $\theta_z$ -torque
- Step M: Net z-force
- Step N: Net  $\theta_y$ -torque
- Step P: Net  $\theta_x$ -torque

- L. Reverse current direction in coil pair (B,D), and repeat steps K and L.

#### Remove Currents

- M. Inject 100 mA peak sinewave of current at 10Hz into coil pairs (1,2), (3,4), (5,6) and (7,8), and repeat steps J, and K.
- N. Reverse current direction in coil pairs (5,6) and (7,8), and repeat steps J and K.
- P. Reverse current direction in coil pairs (3,4) and (5,6), and repeat steps J and K.

#### Remove Currents

- R. Displace the translator 0.001 in. in the positive-x direction. Measure the change in static force and torque in each axis:
  - 1. Net x-force
  - 2. Net z-force
  - 3. Net  $\theta_x$ -torque
  - 4. Net  $\theta_y$ -torque
  - 5. Net  $\theta_z$ -torque
- S. Return the translator to the previous x location, and displace it 0.001 in. in the positive-z direction. Measure the change in static force and torque in each axis:
  - 1. Net x-force
  - 2. Net z-force
  - 3. Net  $\theta_x$ -torque
  - 4. Net  $\theta_y$ -torque
  - 5. Net  $\theta_z$ -torque
- T. Return the translator to the previous z location.
- U. Displace the translator 1/2 the nominal air-gap (0.005 in.) in the positive-x direction. Repeat steps F through T.
- V. Displace the translator 1/2 the nominal air-gap (0.006

in.) in the positive-z direction. Repeat steps F. through T.

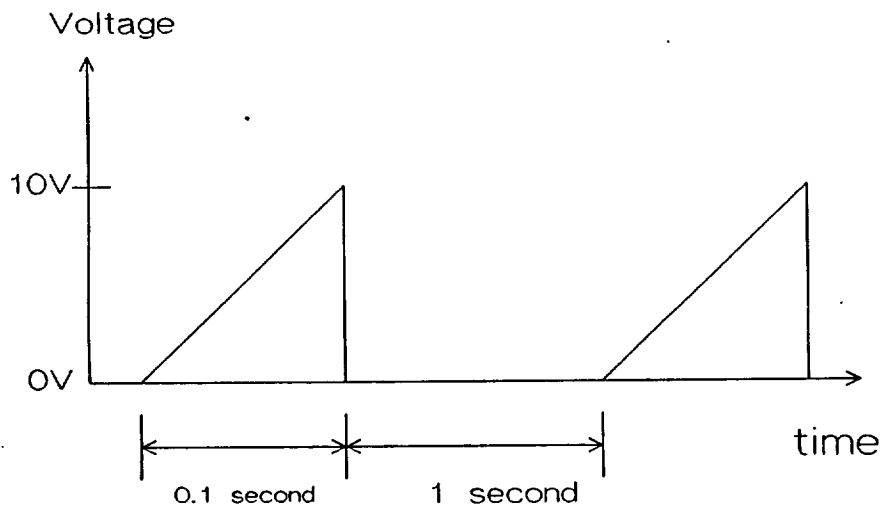
W. Displace the translator 1/2 the nominal air-gap (0.005 in.) in the negative-x direction (back to centered-x position). Repeat steps F through T.

X. Displace the translator 1/2 the nominal air-gap (0.006 in.) in the negative-z direction (back to centered-z position).

## II. Closing the Loops

A. Connect the control loop current drivers to their appropriate control coils.

B. Connect the voltage waveform shown below to the x-force command input. Measure the peak x-force produced.



Voltage Waveform

C. Repeat step D for the same waveshape except going from zero to -10 volts.

D. Connect the voltage waveform shown above to the z-force command input. Measure the peak z-force produced.

E. Repeat step F for the same waveshape except going from zero to -10 volts.

Disconnect the voltage.

F. Dismount the translator/frame assembly from the force test fixture and mount onto the test stand in the

horizontal orientation (Z-axis vertical). Attach the touch-down pads to all pole faces.

- G. Close the control loops and suspend the translator in the centered position.
- H. Alternately adjust the offset potentiometers of position sensors A and B until the currents in coil pairs A,C and B,D are both zero  $\pm 10\text{mA}$ .
- I. Remount the translator/frame assembly on the test stand in the vertical orientation (X-axis vertical).
- J. Alternately adjust the offset potentiometers of position sensors 1, 3 and 5 until the currents in coil pairs (1,2), (3,4), (5,6), and (7,8) are all zero  $\pm 10\text{mA}$ .
- K. Connect 0.1 volt peak 10Hz sinewave to the  $\theta_y$ -position command input. Adjust the r-z sensor-proportioning resistor (R200) for a null in the x-position measurement.
- L. Connect 0.1 volt peak 15Hz sinewave to the  $\theta_x$ -position command input. Alternately adjust the two r-y sensor-proportioning resistors (R17, R18) for a simultaneous null in the z-position measurement at both frequencies.

Disconnect the voltage sinewaves.

- M. Connect 0.1 volt peak 10Hz sinewave to the  $\theta_z$ -position command input. Adjust the two r-y sensor-proportioning resistors (R82, R85) to equal value for a null in the x-position measurement.

Disconnect the voltage sinewave.

- N. Connect 0.1 volt peak 10Hz sinewave to the x-position command input. Adjust the r-y current-proportioning resistor (R99) for a null in the  $\theta_z$ -position measurement.

Disconnect the voltage sinewave.

- P. Connect 0.1 volt peak 10Hz sinewave to the z-position command input. Alternately adjust the r-x and r-y current-proportioning resistors (R33, R37) for a simultaneous null in both the  $\theta_x$ -position and the  $\theta_y$ -position measurements.

Disconnect the voltage sinewave.

- R. Connect 0.1 volt RMS white-noise source bandlimited between 5 and 500Hz to the x-position command input.
- S. Measure the open-loop magnitude and phase response of the x-position loop. Adjust the gain as necessary for 0db cross-over at 100Hz.
- T. Measure the closed-loop magnitude response of the x-position loop.

Disconnect the white-noise source.

- U. Repeat steps R, S and T for each control loop:
  - 1. z-position
  - 2.  $\theta_x$ -position
  - 3.  $\theta_y$ -position
  - 4.  $\theta_z$ -position
- V. Connect 0.1 volt peak 1Hz squarewave to the x-position command input. Measure the x-position step response.
- W. Increase the squarewave amplitude to 2 volts peak. Measure the x-position step response.

Disconnect the voltage squarewave.

- X. Repeat steps V and W for each control loop:
  - 1. z-position
  - 2.  $\theta_x$ -position
  - 3.  $\theta_y$ -position
  - 4.  $\theta_z$ -position

Disconnect the voltage squarewave.

### III. Closed Loop Testing

- A. Connect 0.1 volt peak 10Hz sinewave to the x-position command input. Measure the position signal in each of the other four loops:
  - 1. z-position
  - 2.  $\theta_x$ -position
  - 3.  $\theta_y$ -position
  - 4.  $\theta_z$ -position

Disconnect the voltage sinewave.

- B. Repeat step A for the z-position command input:
  - 1. x-position
  - 2.  $\theta_x$ -position
  - 3.  $\theta_y$ -position
  - 4.  $\theta_z$ -position

Disconnect the voltage sinewave.

- C. Repeat step A for the  $\theta_x$ -position command input:
  - 1. x-position
  - 2. z-position
  - 3.  $\theta_y$ -position
  - 4.  $\theta_z$ -position
- D. Repeat step A for the  $\theta_y$ -position command input:
  - 1. x-position
  - 2. z-position
  - 3.  $\theta_x$ -position
  - 4.  $\theta_z$ -position
- E. Repeat steps A for the  $\theta_z$ -position command input:
  - 1. x-position
  - 2. z-position
  - 3.  $\theta_x$ -position
  - 4.  $\theta_y$ -position
- F. Connect 4 volt peak 1Hz squarewave to the linear motor loop position command input. Measure the peak position signal in each of the position control loops:
  - 1. x-position
  - 2. z-position
  - 3.  $\theta_x$ -position
  - 4.  $\theta_y$ -position
  - 5.  $\theta_z$ -position

Disconnect the voltage squarewave.

- G. Measure the magnetic field along all three axes with the Hall probe at the location of the optical head:
  - 1.  $B(x)$
  - 2.  $B(y)$
  - 3.  $B(z)$
- H. Measure the peak value of the magnetic field along all three axes as the Hall probe is moved over the location of the disk surface:
  - 1.  $B(x)$
  - 2.  $B(y)$
  - 3.  $B(z)$
- J. Measure the current in each control coil:
  - 1.  $I(A,C)$
  - 2.  $I(B,D)$
  - 3.  $I(1,2)$
  - 4.  $I(3,4)$
  - 5.  $I(5,6)$
  - 6.  $I(7,8)$

- K. While observing the x- and z-position signals, cycle the OPEN/CLOSE LOOP switch a number of times to ensure proper start-up operation.
- L. While observing the x- and z-position signals, strike the surface on which the test stand is resting with enough force to cause the translator to hit the frame, and ensure that the loops do not go unstable.
- M. Repeat steps A. through M. with the assembly mounted such that the z-axis is vertical, i.e. rotated 90 degrees.

**9.4 Test Results**

**9.4.1 Open Loop Testing**

RMS voltage of each output in the band from 0.01 to 100Hz:

- |                 |                 |
|-----------------|-----------------|
| 1. V(A) 0.23 mV | 5. V(1) 0.21 mV |
| 2. V(B) 0.27 mV | 6. V(3) 0.16 mV |
| 3. V(C) 0.32 mV | 7. V(5) 0.26 mV |
| 4. V(D) 0.18 mV | 8. V(7) 0.24 mV |

No spectral peaks below 1000Hz with amplitude larger than 6db above the sensor noise floor were observed.

Air-gap flux density at each pole face:

- |                 |                  |
|-----------------|------------------|
| 1. B(A) 1.47 kg | 7. B(3) 1.71 kg  |
| 2. B(B) 1.60 kg | 8. B(4) 1.50 kg  |
| 3. B(C) 1.38 kg | 9. B(5) 1.54 kg  |
| 4. B(D) 1.67 kg | 10. B(6) 1.60 kg |
| 5. B(1) 1.46 kg | 11. B(7) 1.66 kg |
| 6. B(2) 1.43 kg | 12. B(8) 1.50 kg |

Resistance of each coil pair:

- 1. R(A,C) 10.02  $\Omega$
- 2. R(B,D) 9.95  $\Omega$
- 3. R(1,2) 8.32  $\Omega$
- 4. R(3,4) 8.39  $\Omega$
- 5. R(5,6) 8.45  $\Omega$
- 6. R(7,8) 8.23  $\Omega$

Inductance of each coil pair:

- 1. L(A,C) 22.69 mH
- 2. L(B,D) 21.32 mH
- 3. L(1,2) 16.93 mH
- 4. L(3,4) 16.89 mH
- 5. L(5,6) 15.90 mH
- 6. L(7,8) 15.38 mH

X axis drive response at 10 Hz:  
Centered position:

X force 43.80 newton/amp  
Z force 1.58 newton/amp  
X field 2.68 kgauss/amp

+0.005" X displacement:  
X force 48.00 newton/amp  
Z force 2.61 newton/amp

+0.005" Z displacement:  
X force 42.49 newton/amp  
Z force 4.99 newton/amp

+0.005" X, +0.006" Z displacement:  
X force 48.40 newton/amp  
Z force 4.06 newton/amp

Z axis drive response at 10 Hz:

Centered position:  
X force 1.26 newton/amp  
Z force 55.30 newton/amp  
Z field 4.33 newton/amp

+0.005" X displacement:  
X force 5.52 newton/amp  
Z force 48.9 newton/amp

+0.005" Z displacement:  
X force 3.9 newton/amp  
Z force 80.73 newton/amp

+0.005" X, +0.006" Z displacement  
X force 9.60 newton/amp  
Z force 74.90 newton/amp

Linear motor coupling at 10 Hz:

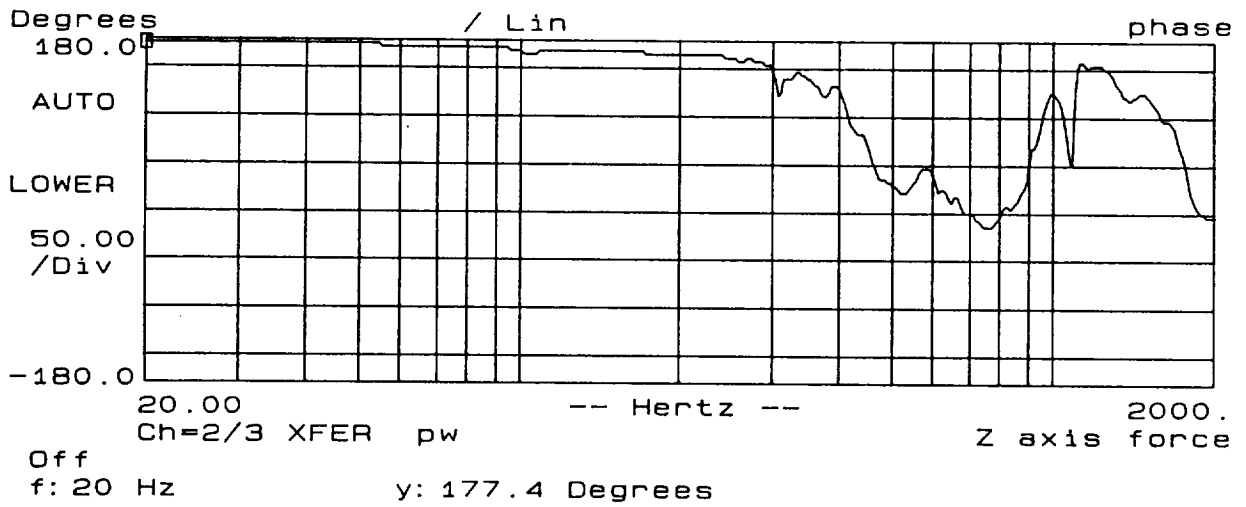
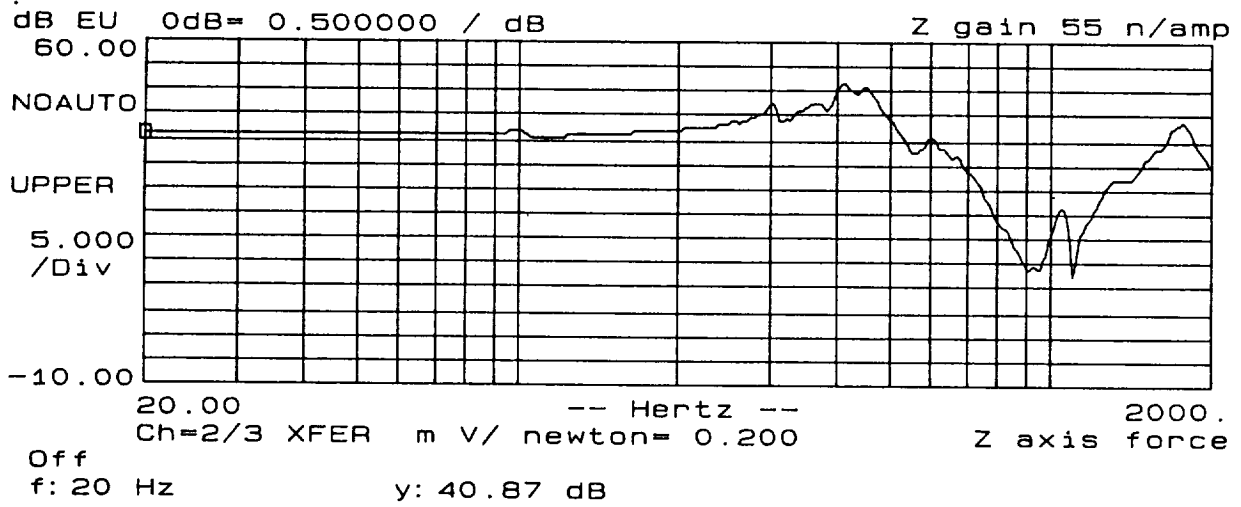
X force 0.44 newton/amp  
Z force 0.74 newton/amp

Leakage field near optical head:

< 25 gauss maximum

The results of the static testing were very encouraging. The primary concerns were force gains, cross coupling, linear motor interaction, and eddy current effects. The results are shown in Figures 9.3 to 9.6. Though the force gains are lower than expected, the system overdesign still allows adequate force levels (2g) to be produced. The cross coupling at the centered position is less than 5% X to Z force, and less than 0.2% Z to X force. At the worst case, one-half gap displacement in both X and Z, the cross coupling is only 8% X to Z force, and 12% Z to X force.





Z PSD, 2KHz, gap 2 field

Figure 9-4. Z Axis Force/Current



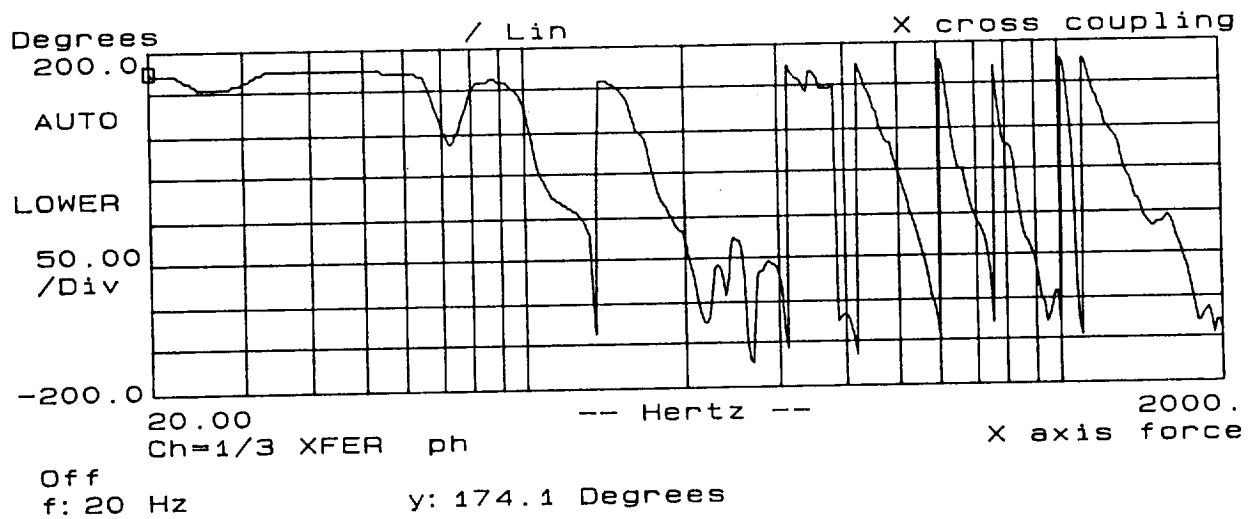
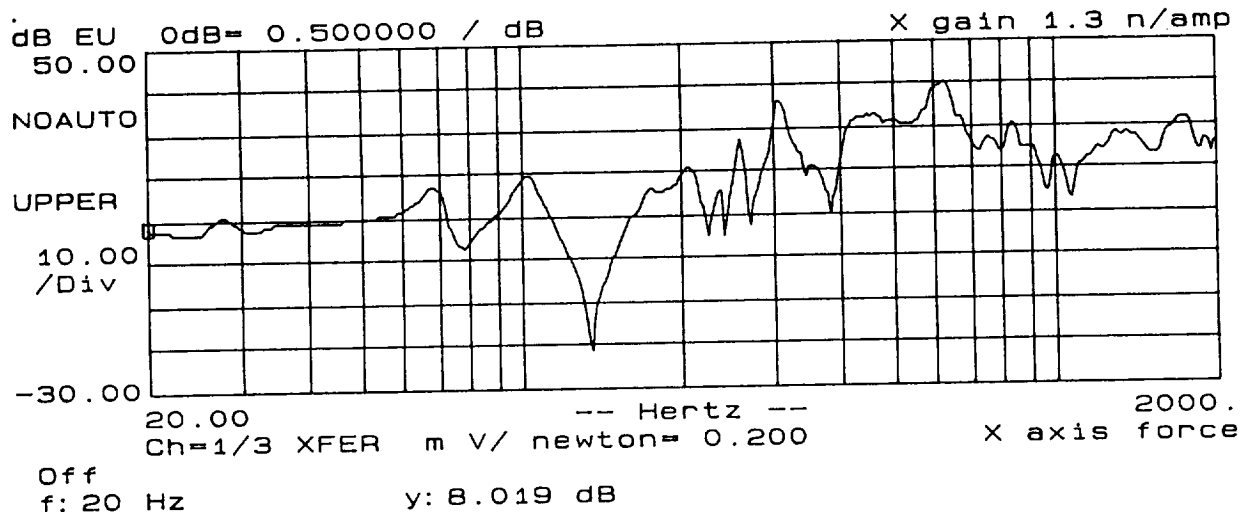


Figure 9-6. Z-X Axis Cross Coupling

The eddy current test results were also good. There were concerns that the force roll off would limit the bandwidth of the control loop. Fortunately, current to field measurements show the roll off to be beyond 500 Hz with a phase loss of only  $10^\circ$  at 100 Hz as shown in Figure 9.7.

Interaction between the linear motor coils and the magnetic bearings was another area of concern. Preliminary analysis indicated that the disturbances should be small, but the geometry of the problem is very complicated. The static test show the coupling gains to be less than 1 newton/amp below 100 Hz in the x axis, and less than 0.5 newton/amp in the z axis for excitation of the encoder side coil.

#### 9.4.2 Closed Loop Testing

This section presents the loop transfer functions and step responses for the suspended translator. The loop responses are shown in Figures 9-8 to 9-13. The loops were adjusted for gain crossover at 100 Hz, giving phase margins from 35 to 67 degrees. The step responses are shown in Figures 9-14 to 9-18. The loops shown little overshoot and good settling time.

Overall, the system behavior was excellent. Steps K-P of the test plan yielded -36 dB  $\theta_y/x$  isolation, -42 dB  $\theta_x/z$  isolation, -48 dB  $\theta_z/x$  isolation, -39 dB  $x/\theta_z$  isolation, and -50 dB  $z/\theta_x$  and  $z/\theta_y$  isolation. The suspension current was 450 mAmp.

#### 9.4.3 Disturbance Sensitivity

The sensitivity of the magnetic bearing system to external disturbances was quantified in two ways: interaction with the linear motor, and bench-top "bang." Linear motor interaction was measured by the transfer function from linear motor current to both effort and motion in all five degrees-of-freedom. The results are shown in Figures 9-18 through 9-20. Figures 9-18 and 9-19 show the motion response in four of the degrees-of-freedom in units of either microns/amp for x and z or milliradians/amp for  $\theta_x$  and  $\theta_y$ . Figure 9-20 shows both the motion and effort response for the  $\theta_z$  loop since the effort response in this loop is significantly higher than in any other due to the relative shortness of the moment arm of the actuators in that axis as compared to the "moment arm" of the mass moment-of-inertia. The peak in the  $\theta_z$  effort response occurs at about 95 Hz and is 18 volts/amp where saturation occurs at approximately 12 volts. The effort response does fall off rather quickly at both lower and higher frequencies, reaching 7 volts/amp at both 10 Hz and 200 Hz. Since the waveform of the linear motor current during a slew maneuver is not known, assessment of the impact of this effort response on system operation was not possible. The worst-case motion responses are 10  $\mu$ /amp in the Z loop and 0.2 mRad/amp in the  $\theta_y$  loop.



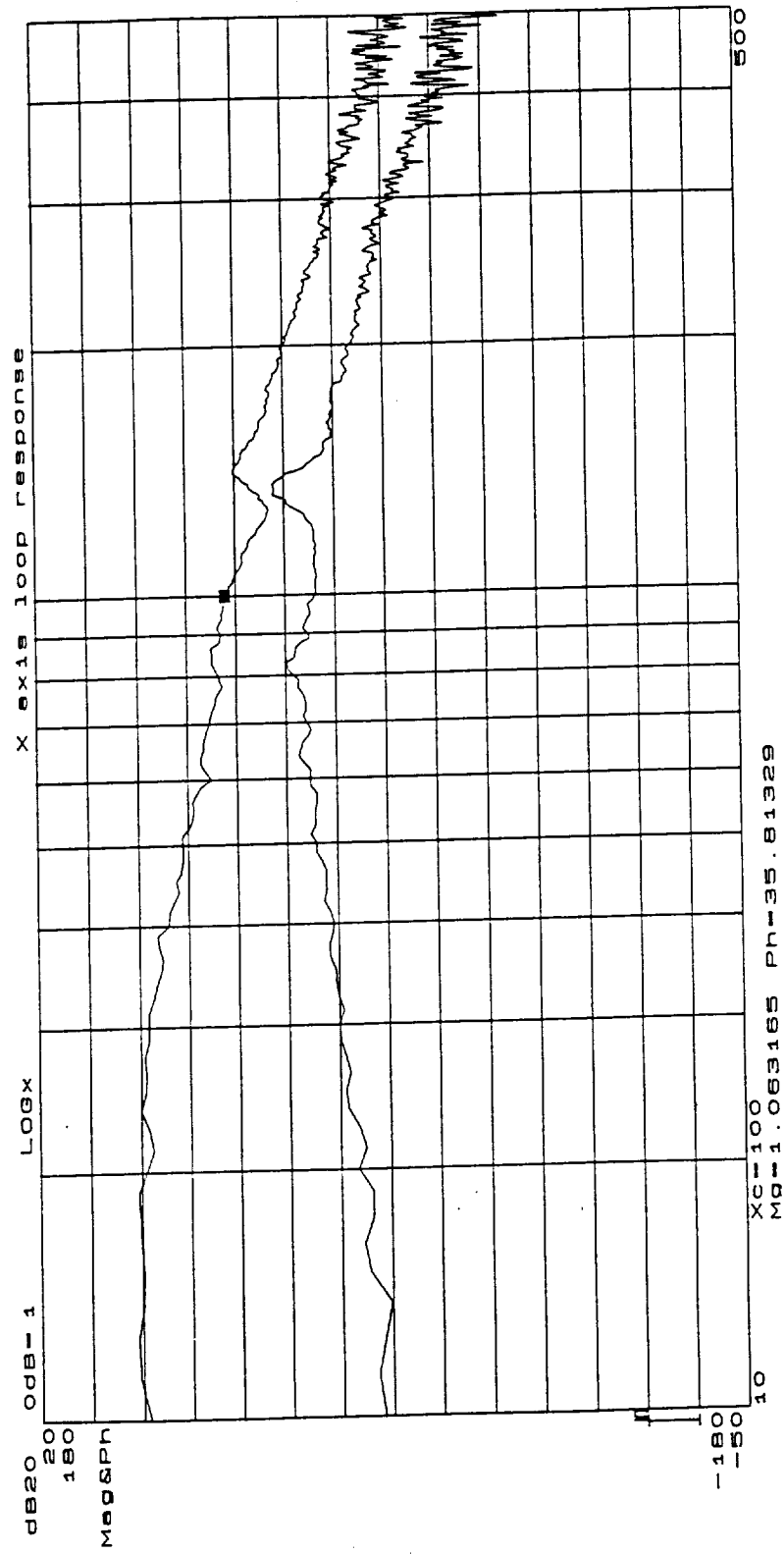


Figure 9-8. X Axis Loop Response

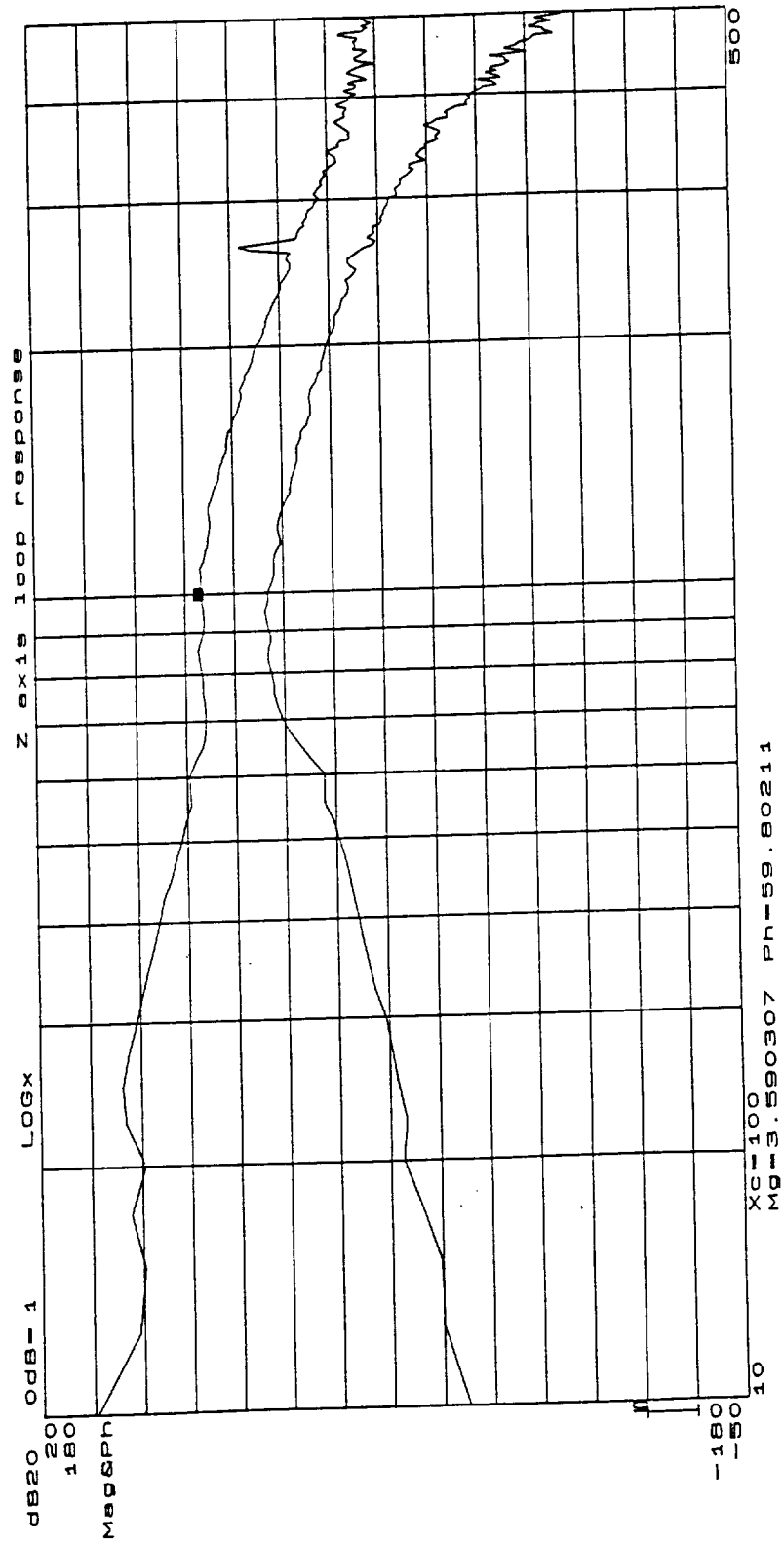


Figure 9-9. Z Axis Loop Response

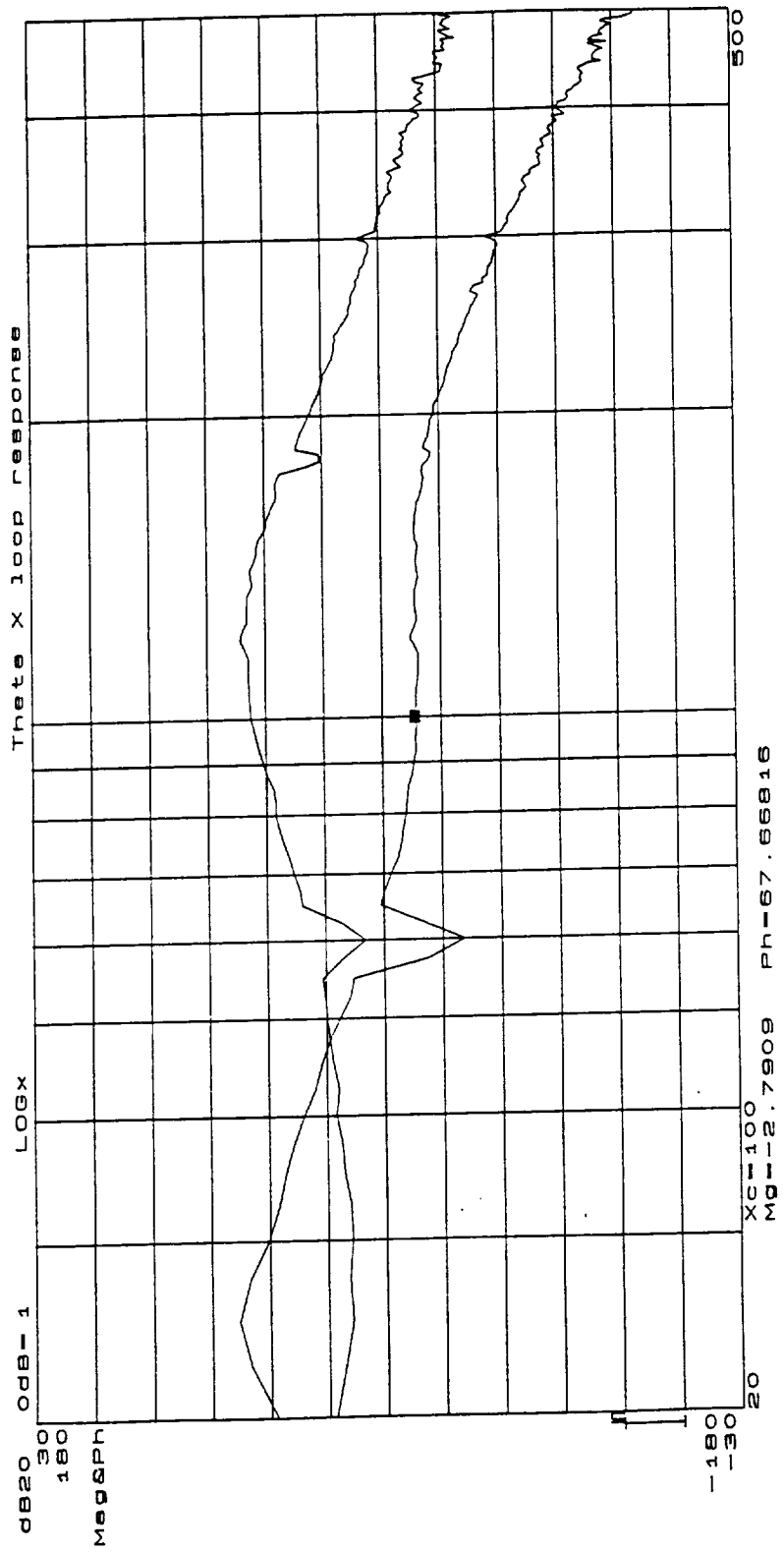


Figure 9-10.  $\theta_x$  Loop Response

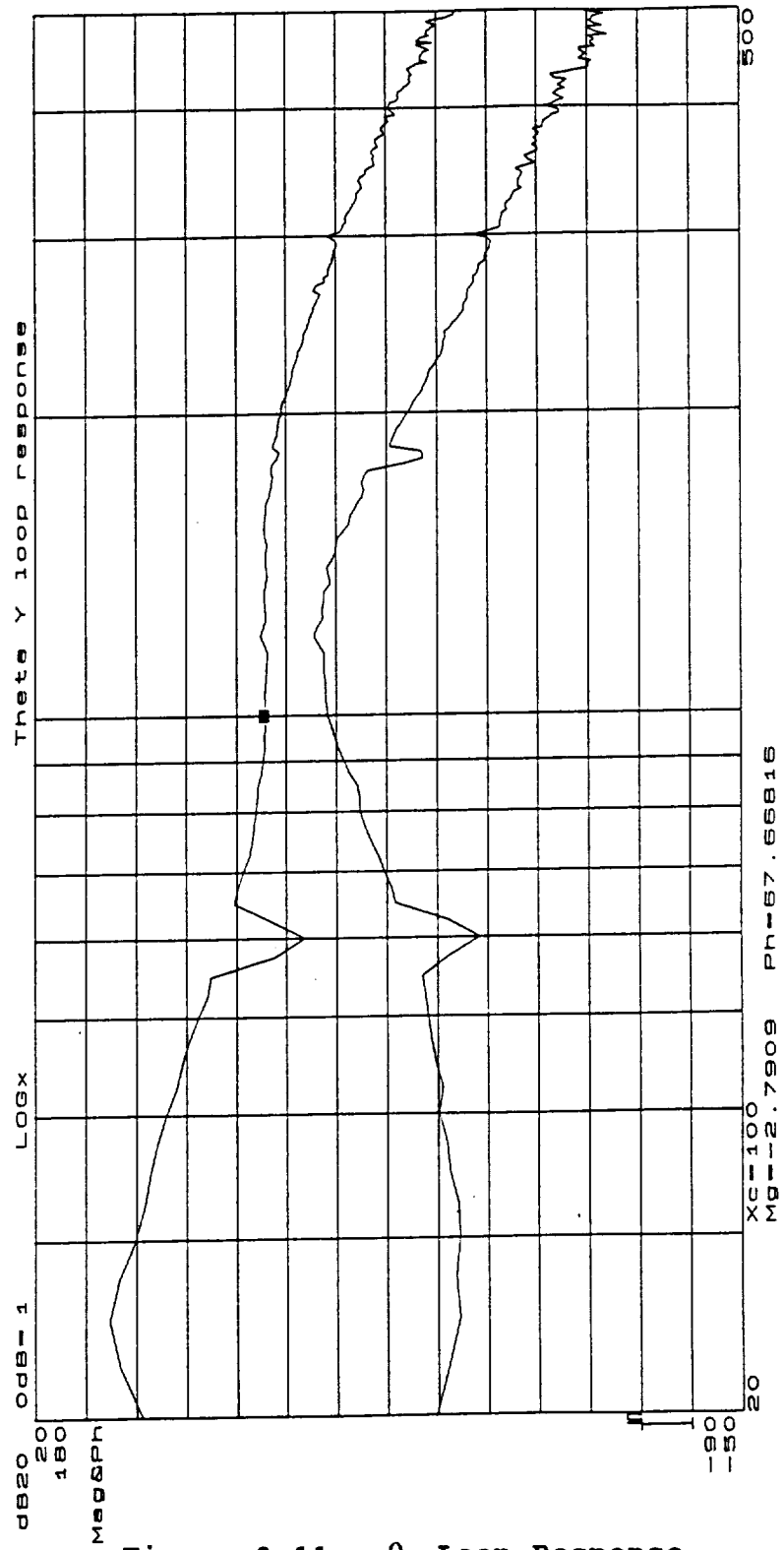


Figure 9-11.  $\theta_y$  Loop Response

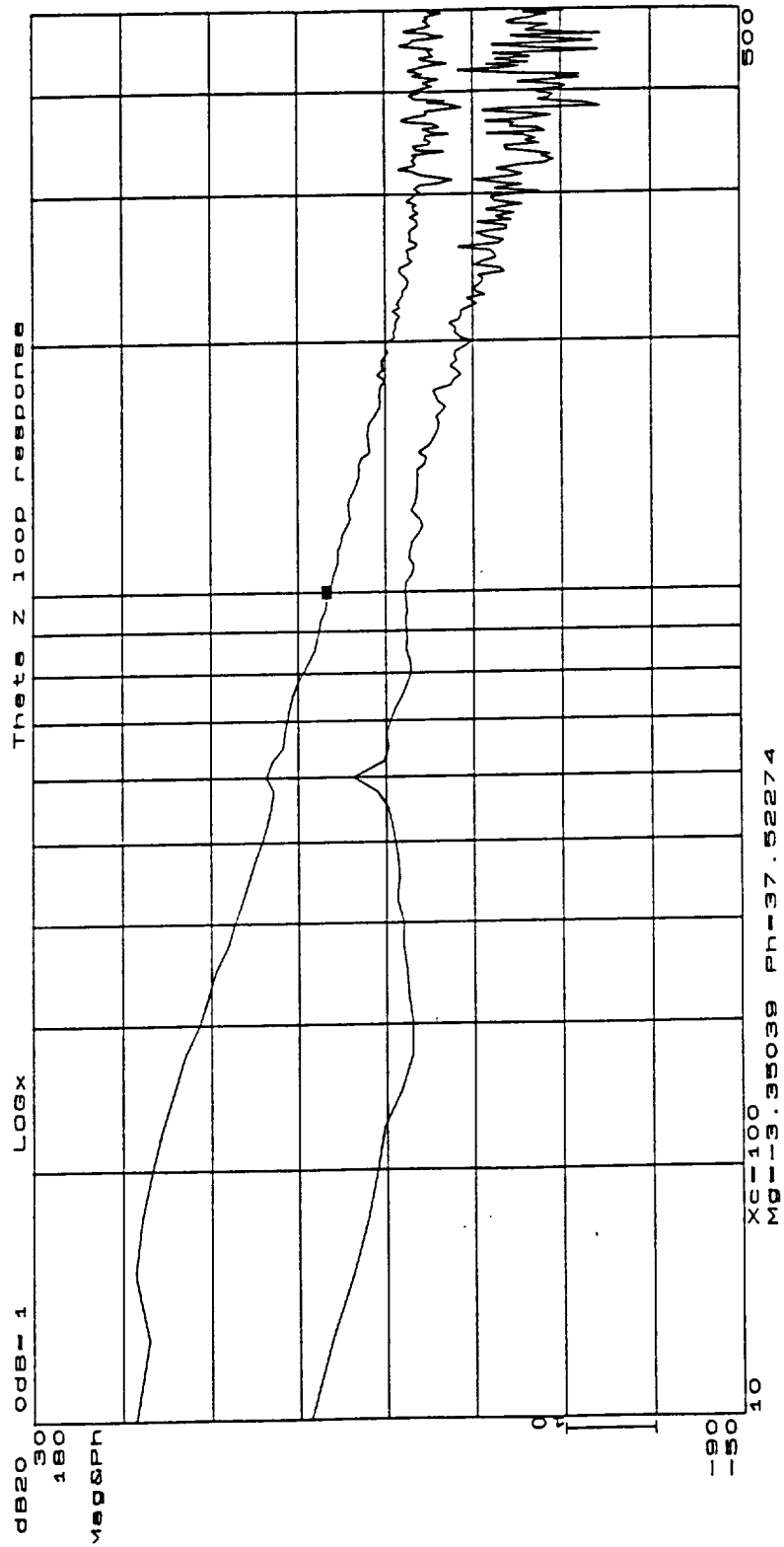


Figure 9-12.  $\theta_z$  Loop Response

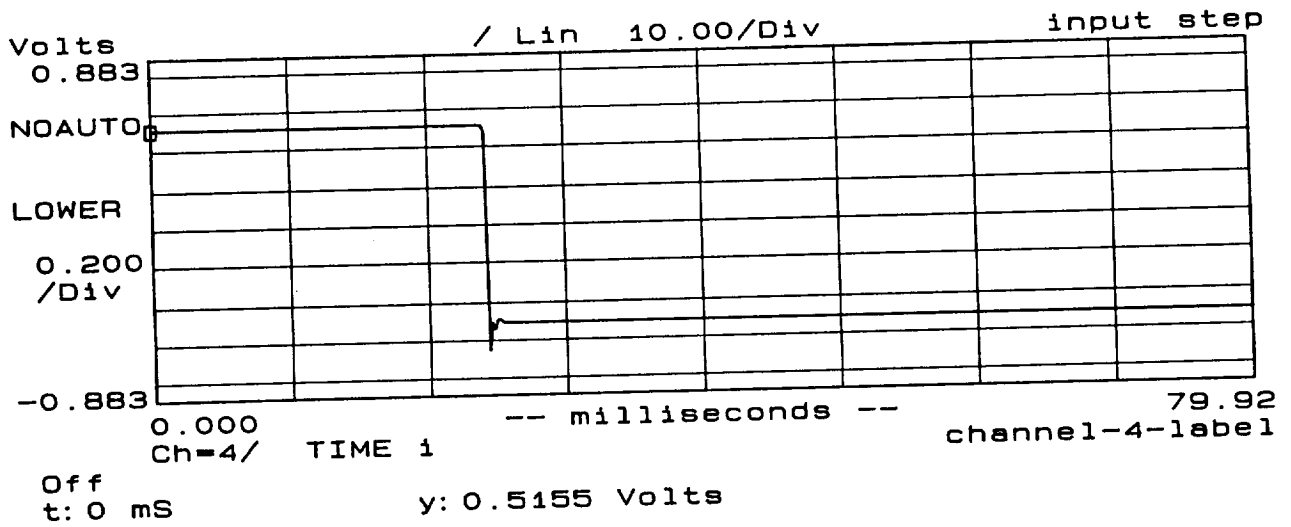
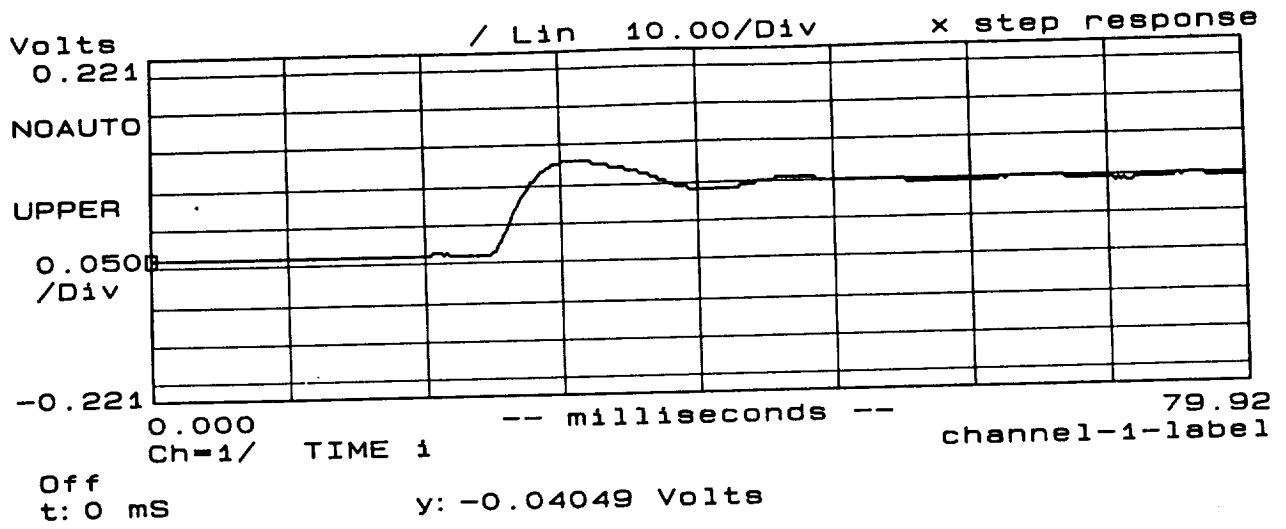


Figure 9-13. X Step Response

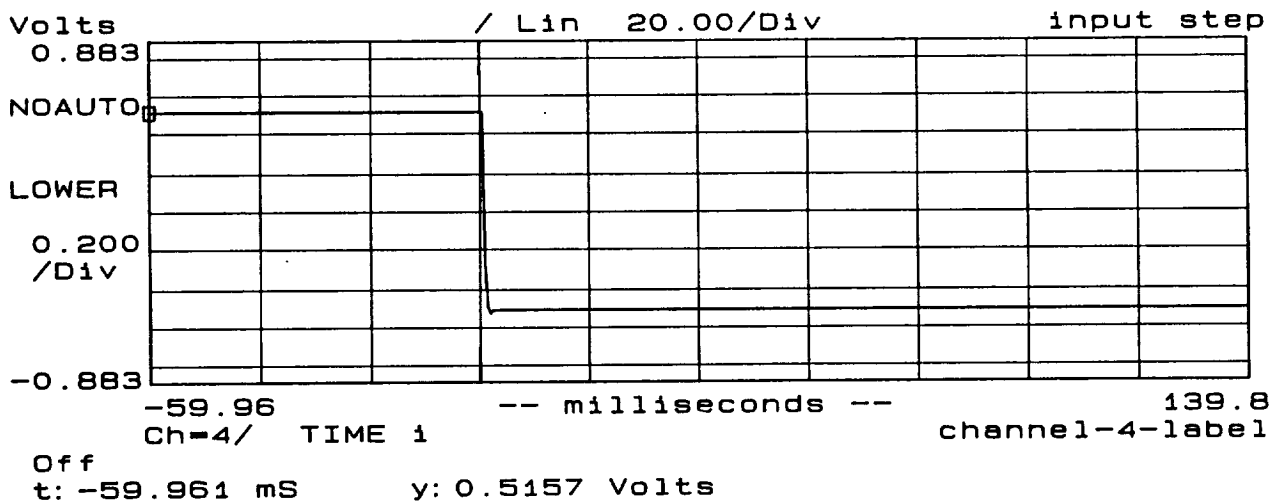
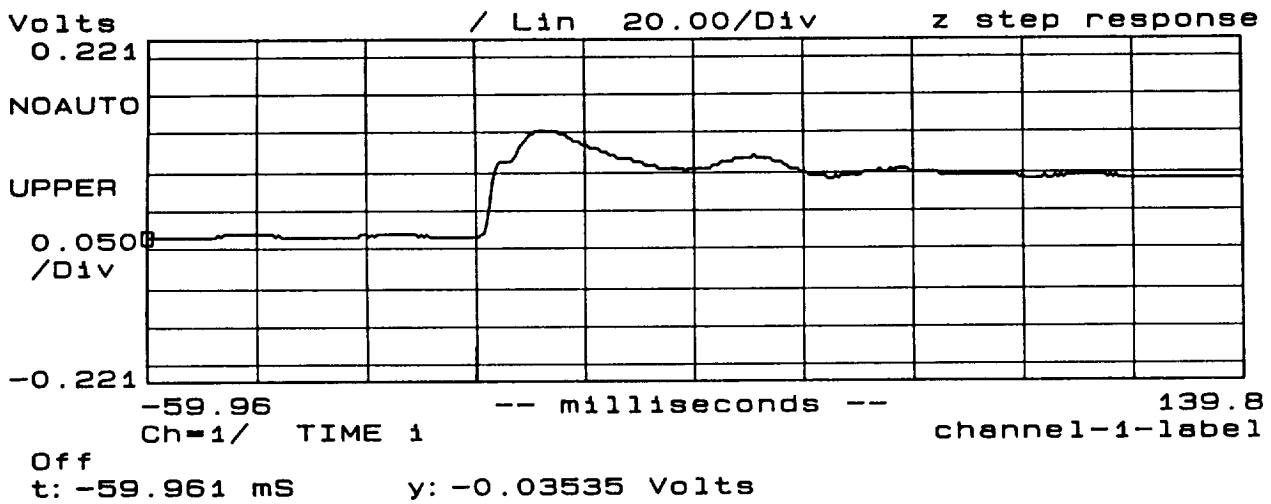


Figure 9-14. Z Step Response

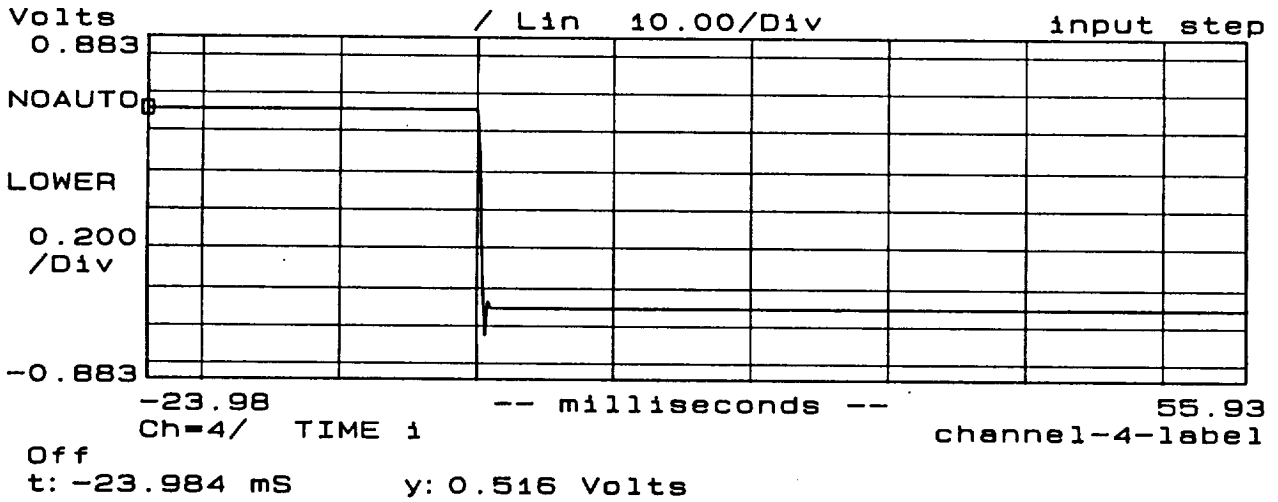
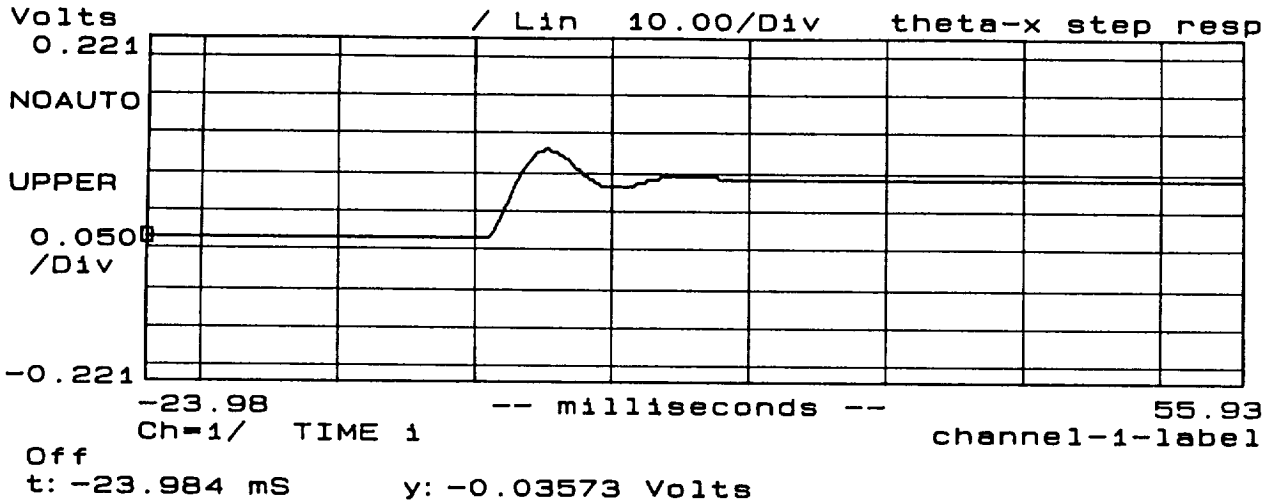


Figure 9-15.  $\theta_x$  Step Response

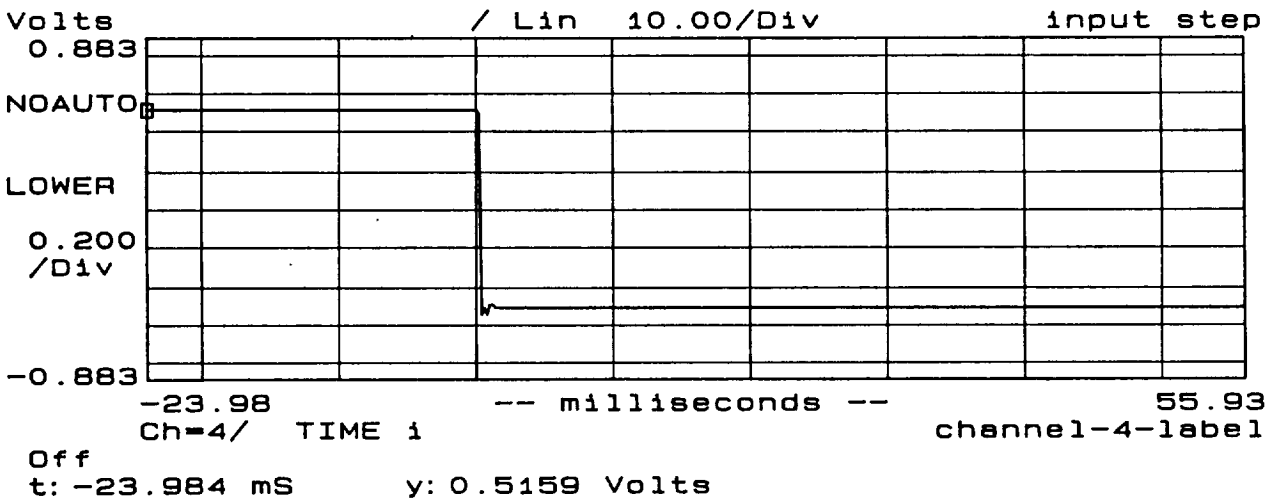
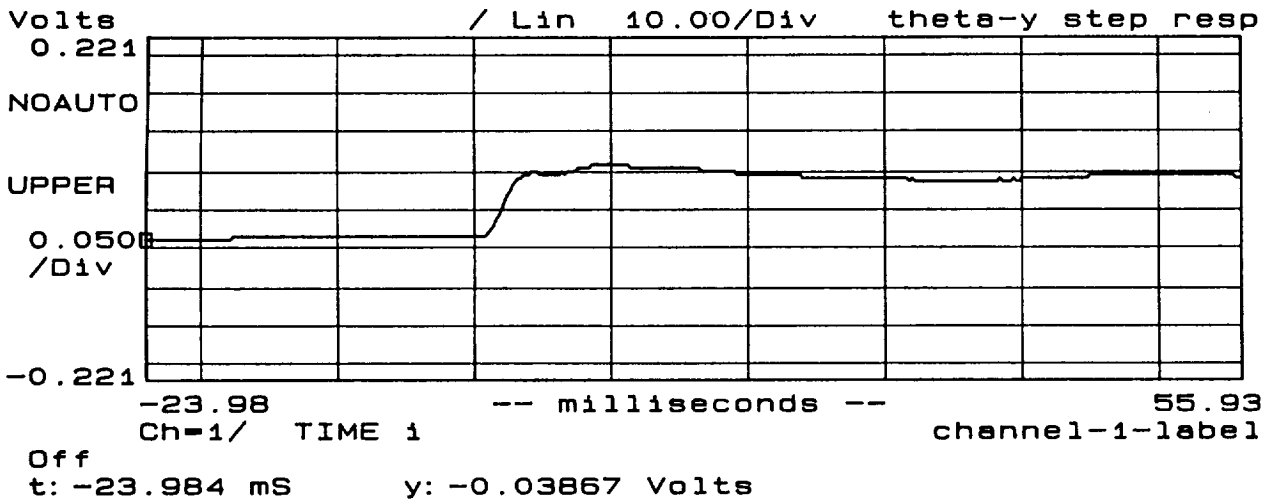


Figure 9-16.  $\theta_y$  Step Response

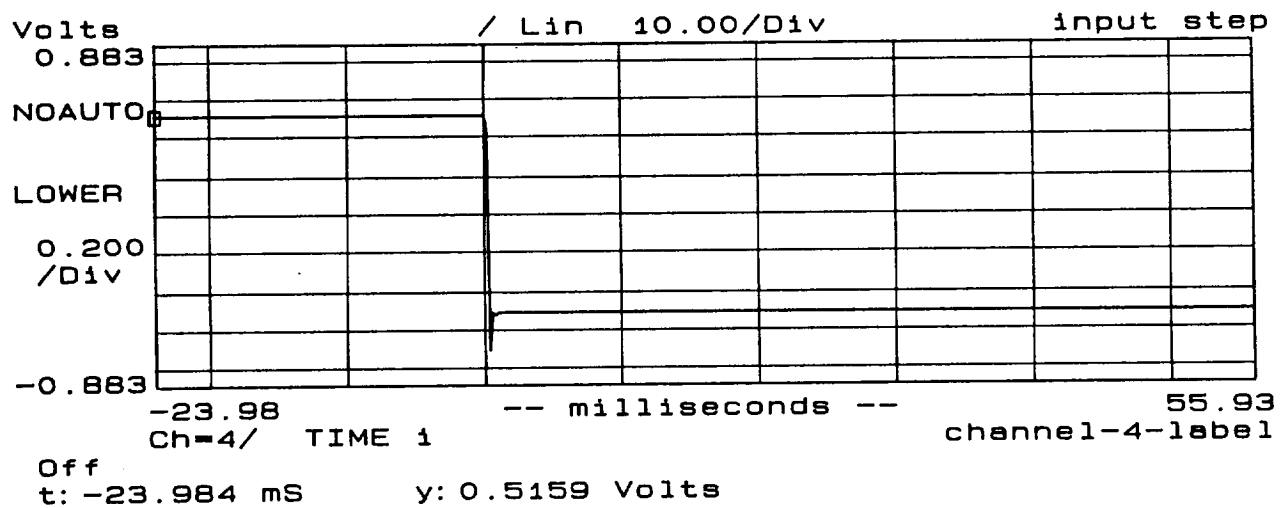
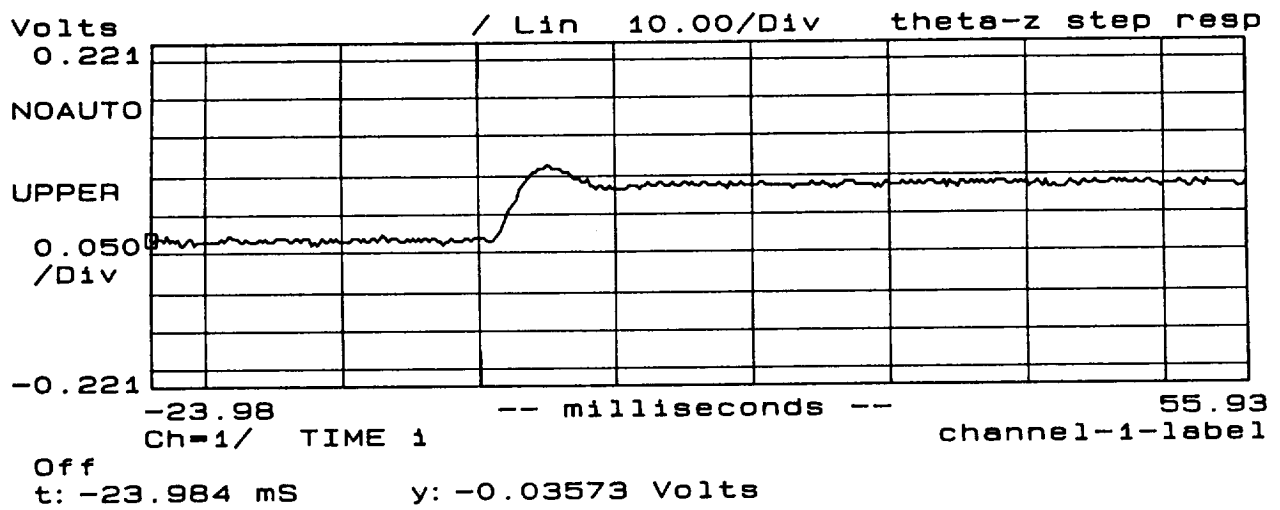


Figure 9-17.  $\theta_z$  Step Response

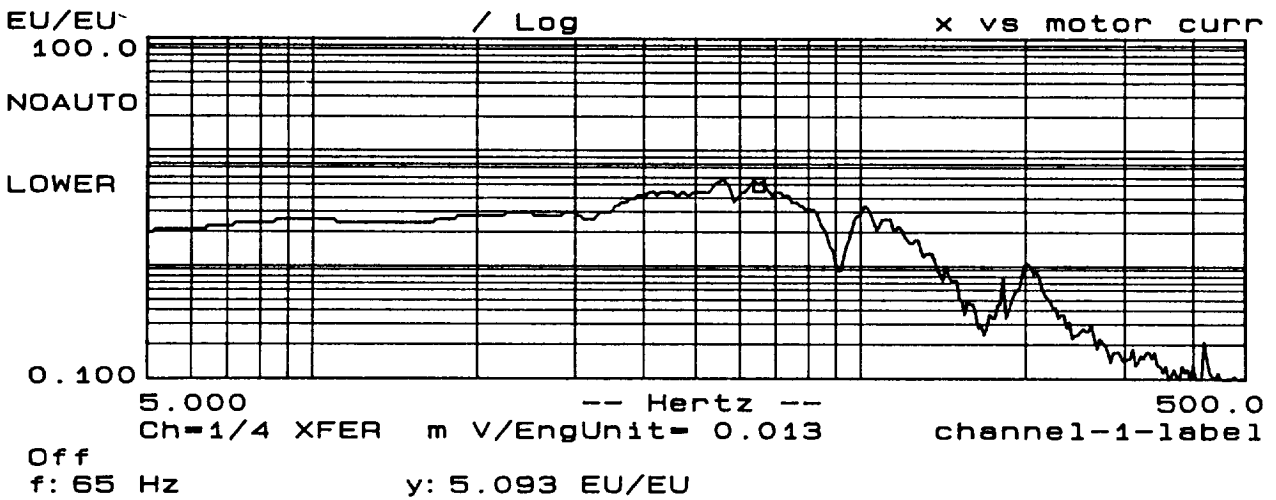
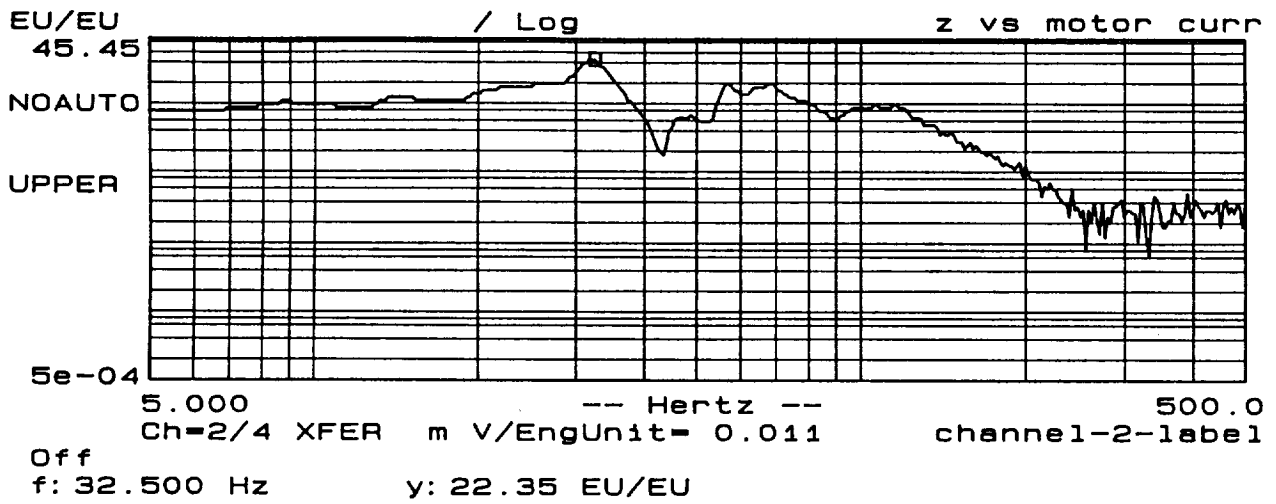


Figure 9-18. Displacement Sensitivity

The bench-top "bang" results are displayed by the displacement signals in the X and Z position loops in Figures 9-21 through 9-24. The range of the vertical axes on these plots represents the complete mechanical gap available for motion of the translator; thus, these plots show numerous collisions with the frame in the X axis. In all cases the loops recovered gracefully without significant overshoot.

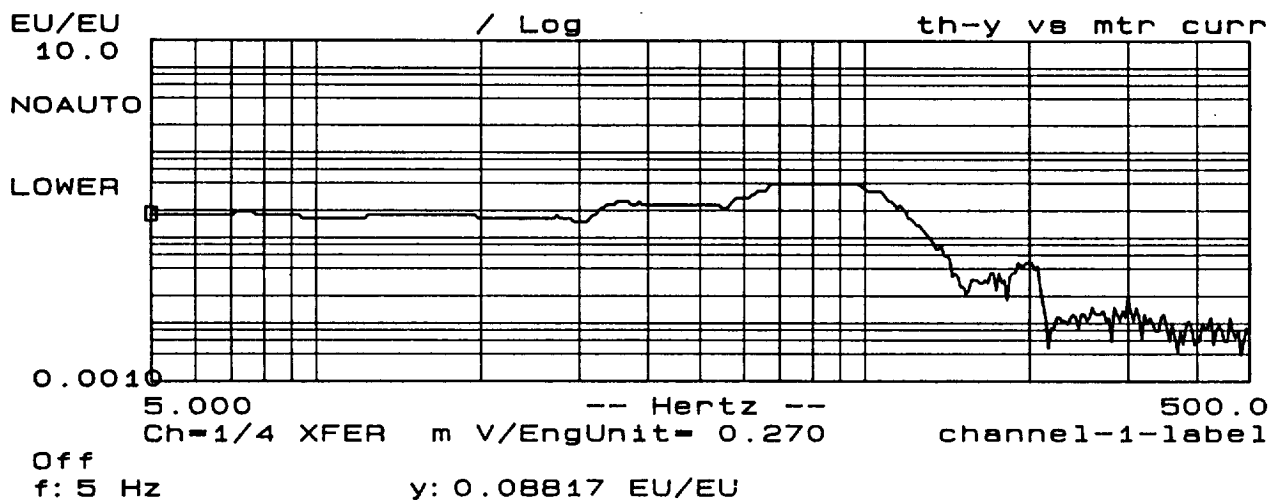
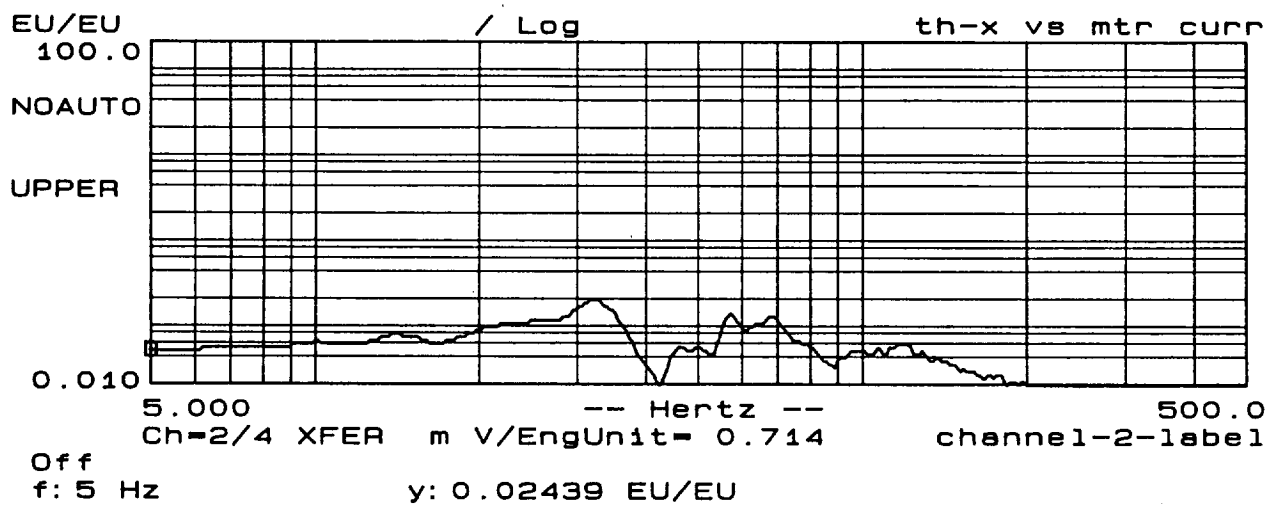


Figure 9-19. Rotation Sensitivity

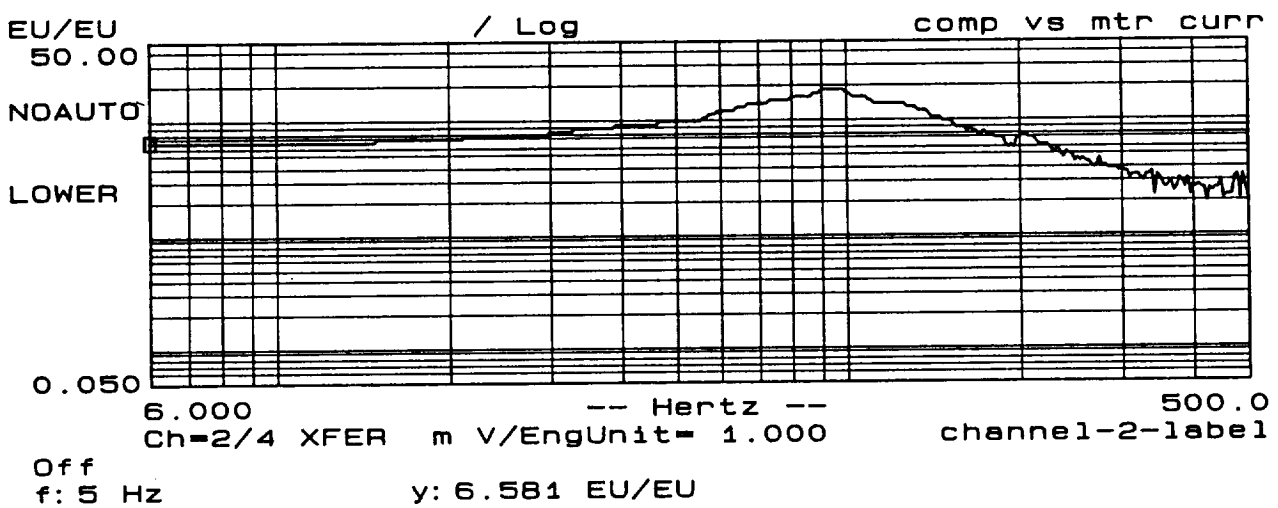
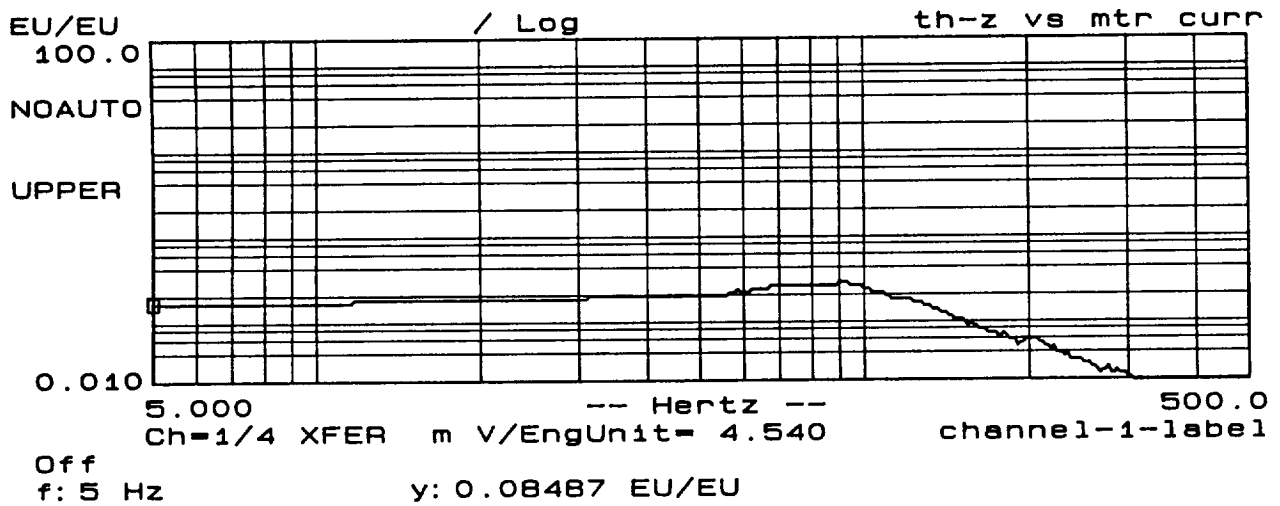


Figure 9-20.  $\theta_z$  Rotation and Effort Sensitivity

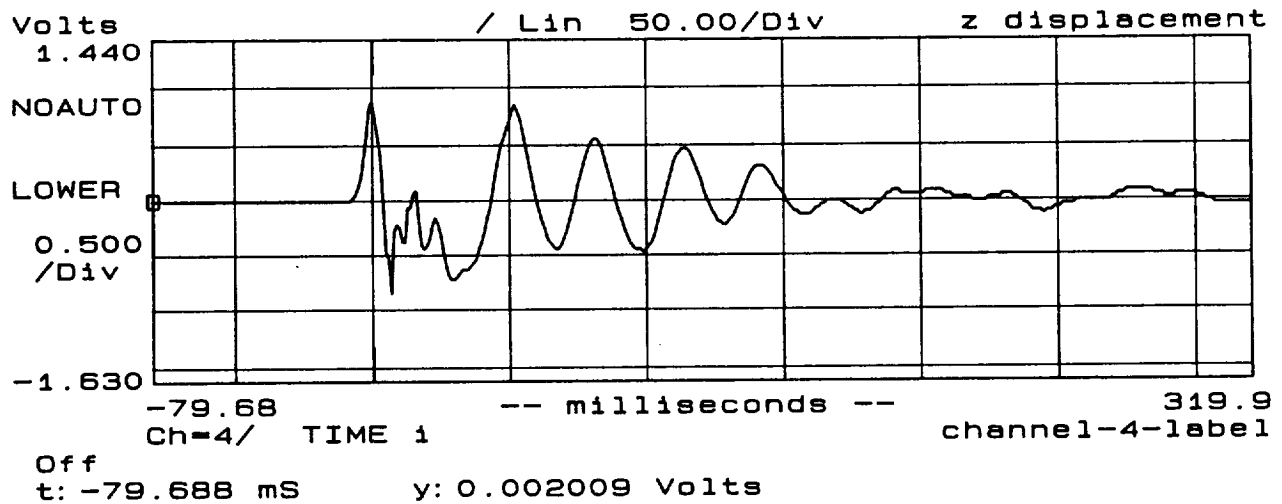
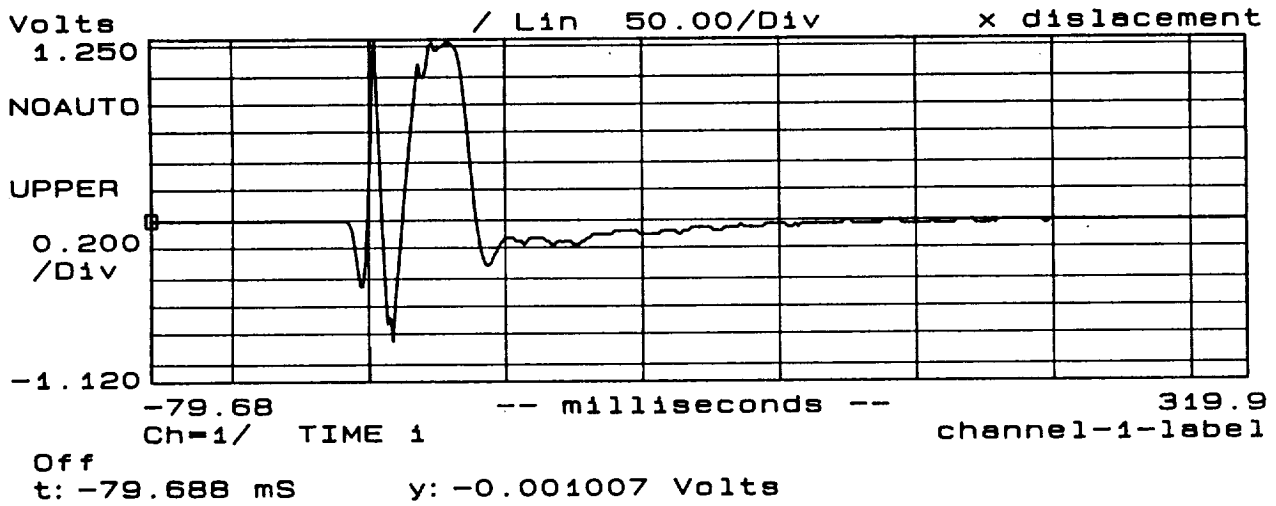


Figure 9-21. Bench-top "Bang" Transients

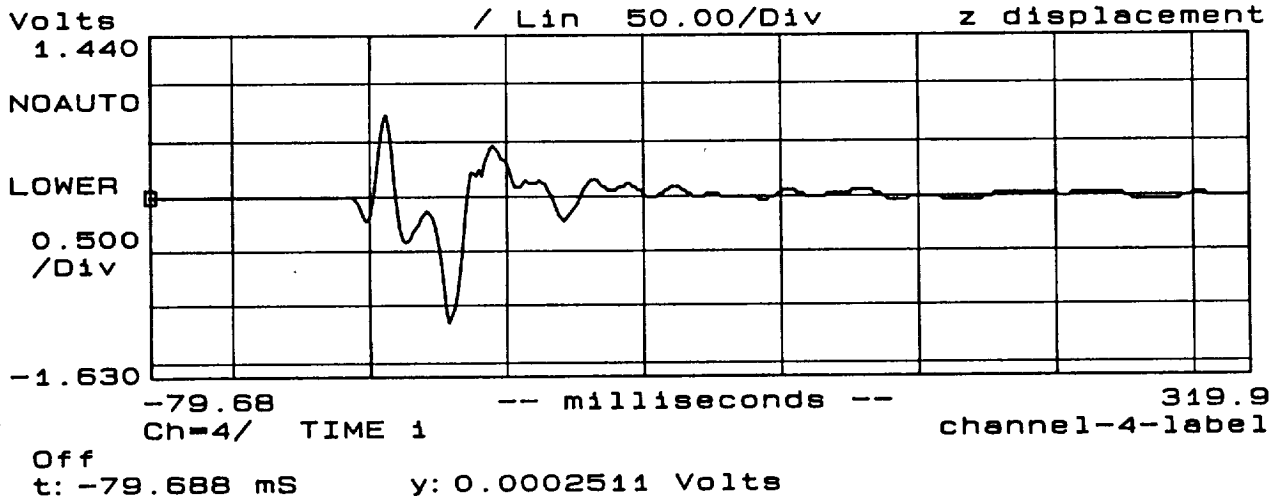
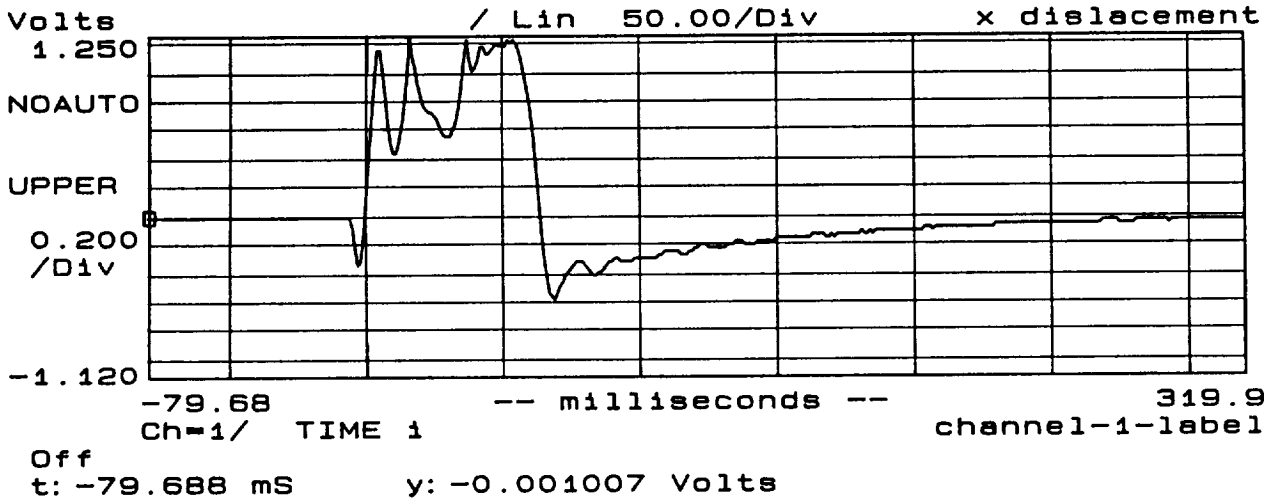


Figure 9-22. Bench-top "Bang" Transients

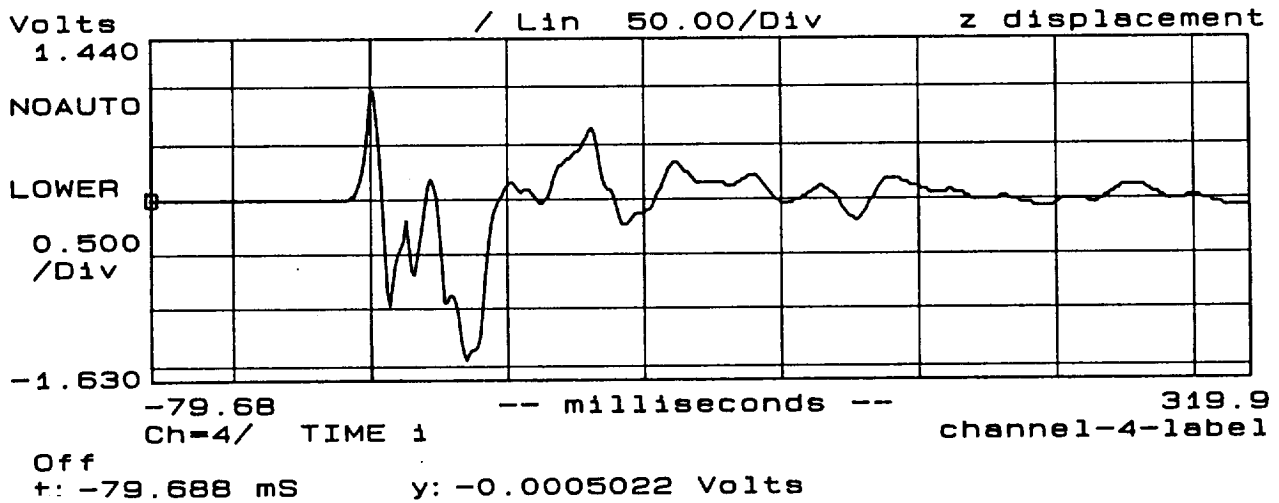
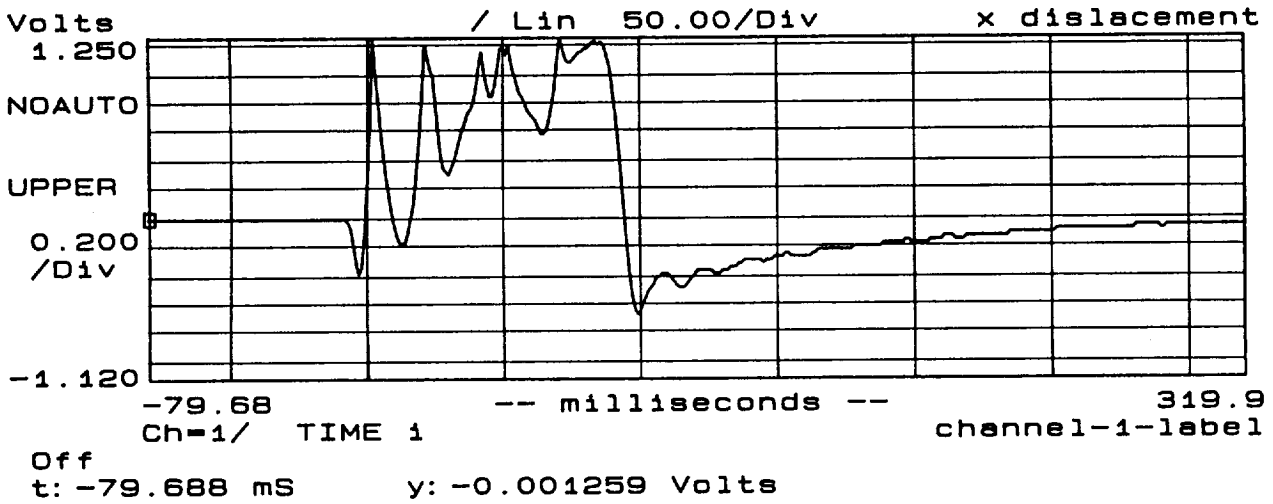


Figure 9-23. Bench-top "Bang" Transients

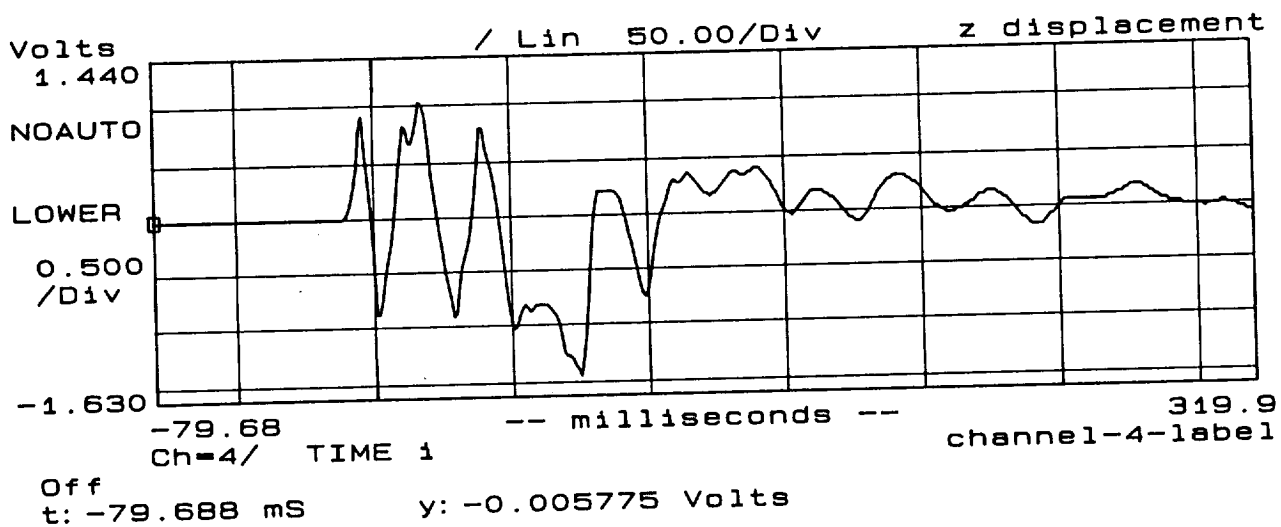
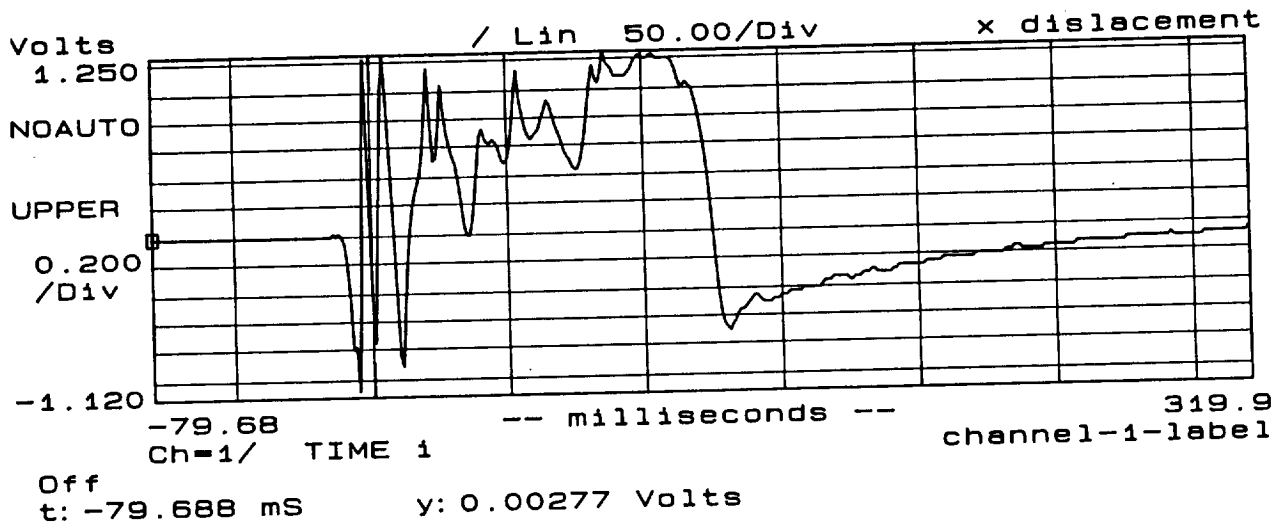


Figure 9-24. Bench-top "Bang" Transients

## 10. CONCLUSIONS AND RECOMMENDATIONS

### 10.1 Performance Summary

The magnetic bearing control loops perform well, achieving 100 Hz nominal bandwidth with phase margins between 37 and 63 degrees. The lag in the actuator response from current to force produced by eddy-current losses introduces only 10 degrees of phase lag in the loop response at 100 Hz. The worst-case position resolution is  $0.02 \mu$  in the displacement loops and  $1 \mu$ rad in the rotation loops. The system is very robust to shock disturbances, recovering smoothly even when collisions occur between the translator and frame. The start-up/shut-down circuit has proven very effective both in achieving initial levitation and in minimizing the "clunk" during turn-off.

The potential problem which exists is the sensitivity of the  $\theta_z$  rotation loop to disturbance from the linear motor. Lack of knowledge of the current waveform in the linear motor during a slew transient makes the severity of this problem, which is discussed below, impossible to assess.

### 10.2 Problem Areas

During the course of initial testing, it was discovered that some of the actuators were being driven into partial saturation by the current noise that was applied to them. This large current noise was simply sensor noise amplified by the gain of the control loop, including the actuator-current driver with its 2 kHz closed-loop bandwidth. The source of the problem was found to be the  $\theta_z$  control loop because it has 10 times the open-loop gain of all the other loops. The higher loop-gain requirement is produced by the mismatch between the moment arms of both the position sensors and actuators, and the "moment arm" of the mass moment-of-inertia. This is due to the fact that both the sensors which measure  $\theta_z$ , and the actuators which produce the torque about the z axis had to be mounted along one of the short axes of the translator while the inertia about the  $\theta_z$  axis is along the long axis. The noise problem was solved by reducing the noise of the sensor electronics by a factor of five as described in detail in Section 7.4, but the mismatch does result in a significantly reduced torque capability in the  $\theta_z$  loop.

As mentioned above, and presented in detail in Section 9.4.3, this reduction in torque capability is the source of the most significant potential problem in the system, i.e., the sensitivity of the  $\theta_z$  position-loop to disturbance from the linear motor. While the magnitude of this sensitivity is very frequency dependent, for the worst-case scenario of 100 Hz sinusoidal excitation, the linear motor current would have to be restricted to 1.3 amp peak-to-peak to avoid saturating the loop-compensation stage. At lower or higher frequencies the

sensitivity decreases, allowing 4 amps peak-to-peak at both 10 Hz and 200 Hz. Since the linear motor current profile during slew is not known, the impact of this sensitivity on system performance cannot be assessed. The two-pronged impact of the moment-arm mismatch does however present an interesting lesson for the design of future magnet bearing systems.

It was originally intended to mount a Linear-Variable Differential Transformer (LVDT) on the translator and use its output to close a coarse position loop which would be controlled from the front panel for demonstration purposes. The part of the LVDT which actually mounted to the translator was the magnetic core of the LVDT cantilevered on a threaded rod. This system was omitted from the final design for two reasons. First, the long moment arm of the magnetic core resulted in a significantly displaced center-of-mass for the translator assembly making decoupling the five degrees-of-freedom very difficult. Second, this problem was also complicated by the flexible mode of the core/rod structure which had a high-Q resonance at 36 Hz. This frequency is close enough to crossover that it was impacting the closed-loop performance of some of the position loops.

The final problem uncovered during system testing was that occasionally the  $\pm 15$  volt power supply would go into current limit during power-up and latchup with outputs of +5 volts and zero volts. This was found to be caused by the use of "fold-back" current limiting in the power supply, a method which reduces the output current limit as the output voltage decreases in response to the current limiter. While fold-back limiting works well with resistive loads, it can latch-up with the type of non-linear load which this system presents during power-up. The solution to this problem was to place a switch between the  $\pm 15$  volt output and the Magnetic Bearing Controller board, such that the supply is at full voltage before the current load is applied. This switch was mounted on the front panel along with an indicator light for DC power.

### **10.3 Areas for Improvement**

The predominant shortcoming of the present system design is the gross mismatch between the center-of-mass of the translator and the center-of-effort of the magnetic actuators. This mismatch means that, in order to decouple the rotation loops from the displacement loops, some of the actuators must produce virtually no force. This restriction severely limits both the gain and the total force capability of the displacement loops. In addition, the large differences in actuator gains makes the process of adjusting the loop-decoupling very difficult. A system in which the center-of-mass was located close to the center-of-effort would be nearly inherently decoupled making any slight adjustment a trivial process. These effects should be considered in future system designs.

#### 10.4 Future Work

The possibilities for future work which builds upon the success of this program are threefold. First, and most obvious, is the integration of this magnetic bearing retrofitted read/write head translator into the existing optical disk system test-bed. The impact of the position resolution of the bearings should be measured. In addition, the interaction of the magnetic bearing control loops with the linear motor and both the focus and tracking servos should be checked. The second possibility for future work is the application of this magnetic bearing configuration to other linear motion applications such as interferometers, cryo-coolers, etc. Since the fundamental concept has been proven, extending it to other such uses should prove a straightforward exercise.

Finally, while magnetic bearings have been developed by NASA for many various applications, no magnetic bearing has ever been flown in space by the United States. The availability of GAS-cans aboard the STS as a vehicle for space experimentation presents a unique opportunity to gain valuable experience and data from a magnetic bearing in the space environment.

## APPENDIX A

### Finite Element Model

Finite element analyses were performed using the Maxwell software by Ansoft Corp. to verify the lumped parameter design. Though the two-dimensional software was not able to capture the complete three dimensional magnetic structure, the control coils and their gap fields could be modeled. Shown in Figure A.1, the cross section includes the X and Z axis pole faces, the shaft, and the control coils.

The finite element software approximates the solution of Maxwell's equations on a mesh in the regions of interest given field sources (coils and/or permanent magnets) and material properties. The mesh, shown in Figure A.2, was adaptively generated over several iterations by estimating the solution error and refining the mesh in regions of large error. Saturation effects may also be modeled with the inclusion of material magnetization curves.

Field solutions for the X and Z coils are shown in Figures A.3 and A.4 which include lines of constant magnetic potential,  $A$ , and scaled field vectors. The X and Z axis field gains were 0.27 tesla/amp and 0.47 tesla/amp. This shows good agreement with 0.27 and 0.43 tesla/amp for the lumped parameter approximation, and 0.35 and 0.49 tesla/amp experimentally.

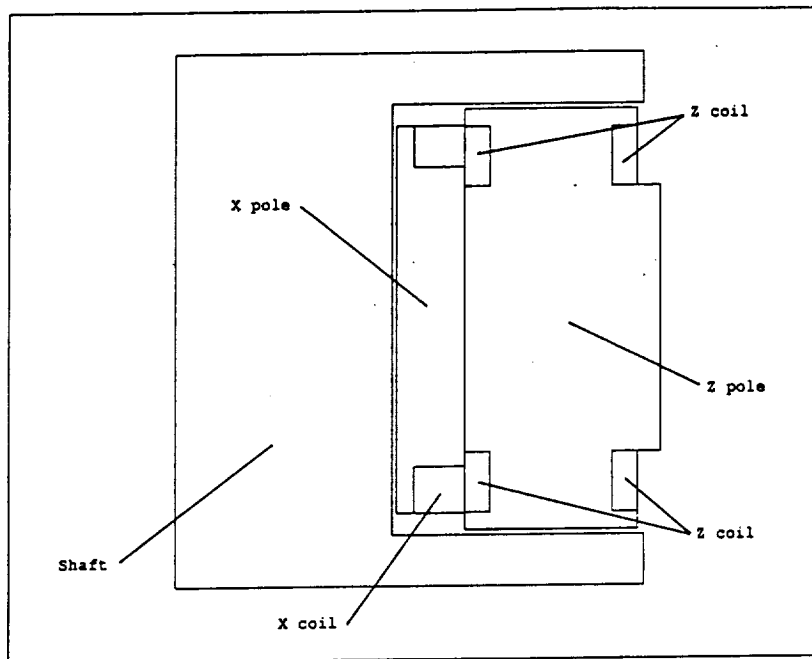


Figure A-1. Finite Element Model

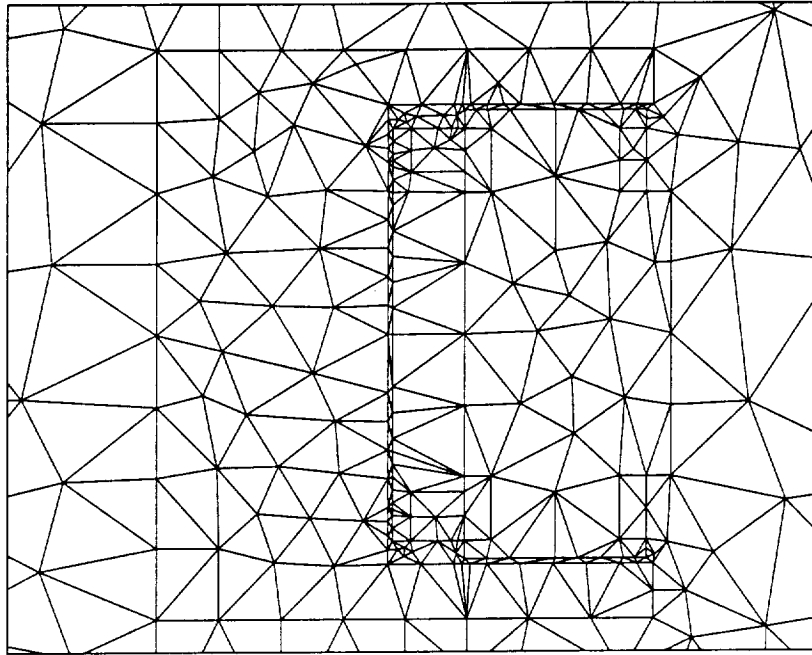


Figure A-2. Finite Element Mesh

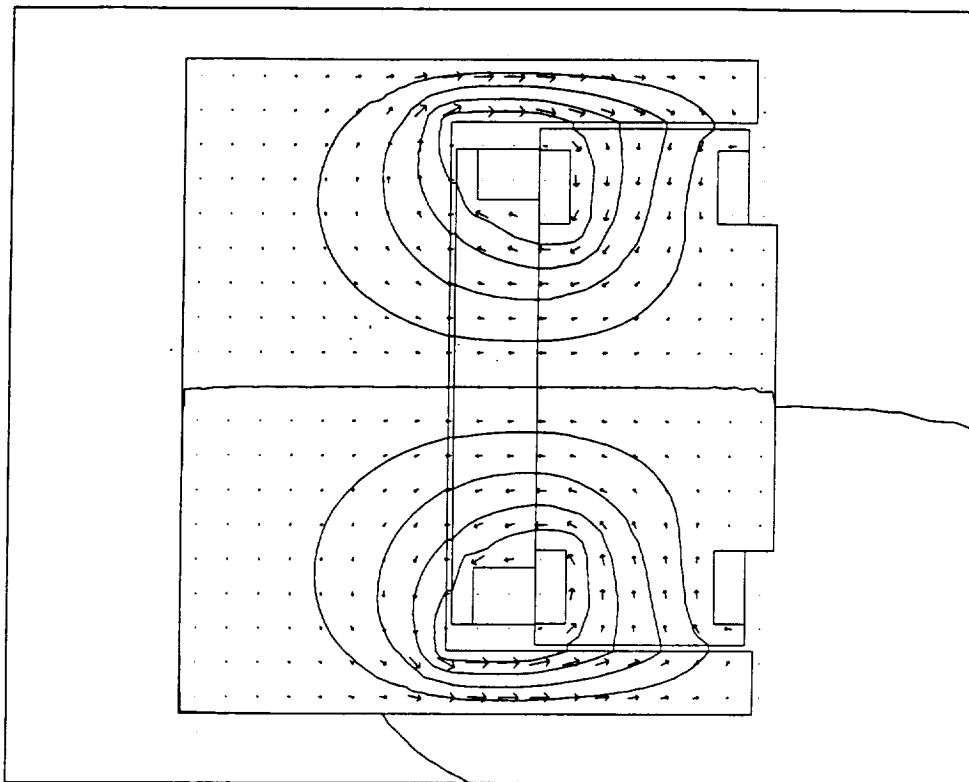
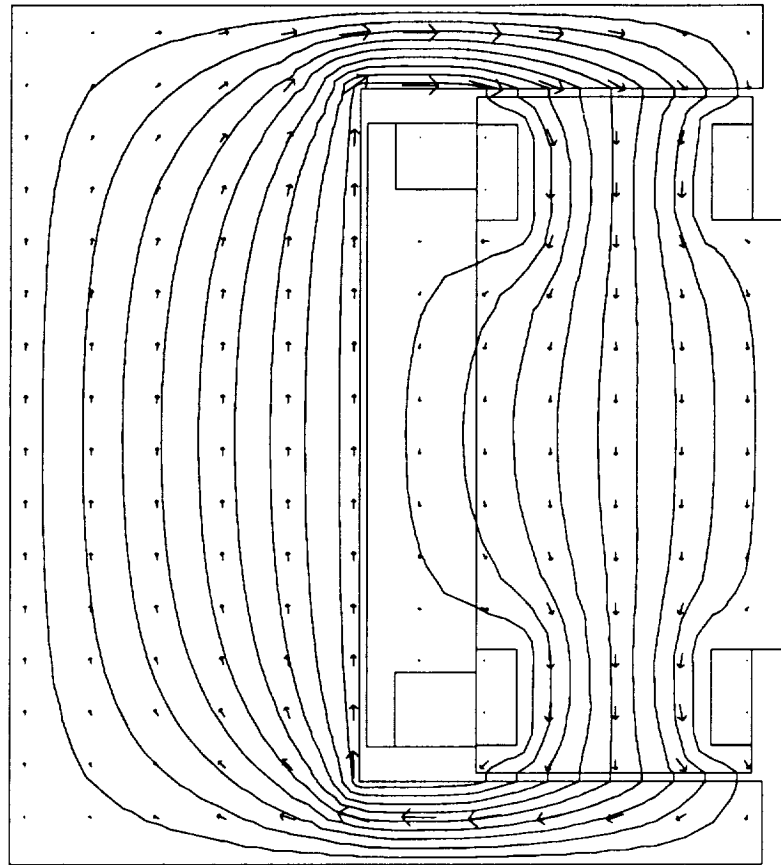


Figure A-3. X Axis Coil Solution



**Figure A-4. Z Axis Coil Solution**

## APPENDIX B

### Eddy-Current Analysis and Testing

This appendix presents a linear analysis of eddy currents in unlaminated magnetic circuits. The purpose of performing this analysis is to provide an understanding of the dynamics which become important at frequencies higher than those associated by the instability. These effects reduce the stability (phase and gain) margins of closed-loop magnetic bearing systems.

In order to develop an adequate conceptual model, the analysis begins by considering the gapped toroid shown in Figure B.1. This result was verified by experimentation. The results are readily extended to the case of an actual magnetic bearing.

#### B.1 Toroid Analysis

The analysis assumes a linear relation between flux density and field strength. Provided that operation is on the linear portion of the magnetization curve, this assumption is not a bad one. In general, however, the relationship between field strength and flux density is highly nonlinear. The following section lists the restrictive assumptions, that were needed to make the problem tractable. Nevertheless, this theory provides a conceptual understanding of the physics of eddy currents shielding in magnetic circuits and leads to an equivalent circuit model that can be used to make rough quantitative calculations.

##### B.1.1 Assumptions

The eddy current analysis is carried out in cartesian coordinates for a toroid of rectangular cross-section, with an air gap (shown in Figure B.1). To make the problem more tractable, the following simplifications are made:

- (1) The material is linear, meaning that flux density (B) varies linearly with field strength (H).

$$B = \mu H \quad (B.01)$$

- (2) Permeability ( $\mu$ ) and conductivity ( $\sigma$ ) are uniform throughout the cross-section.
- (3) The flux density has only one component (in the x direction in Figure B.1) and varies in the two directions orthogonal to this component (z and y).

$$B = i_x B(y, z) \quad (B.02)$$

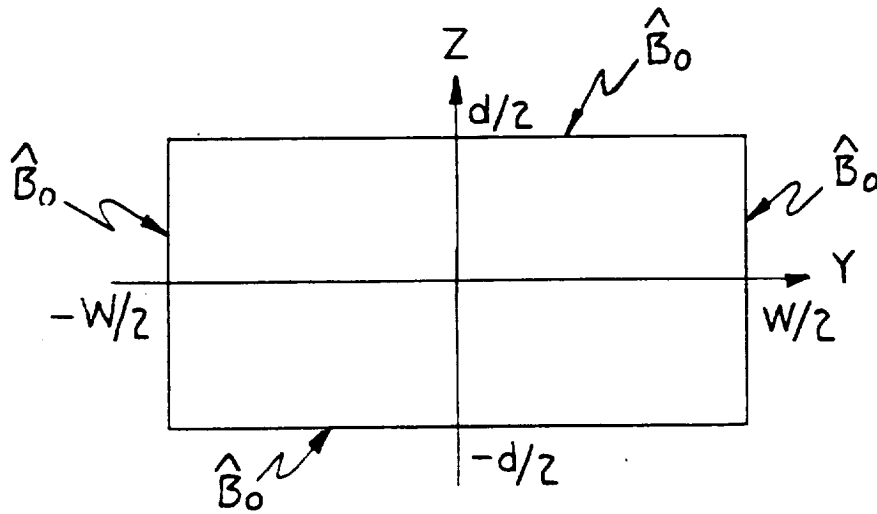
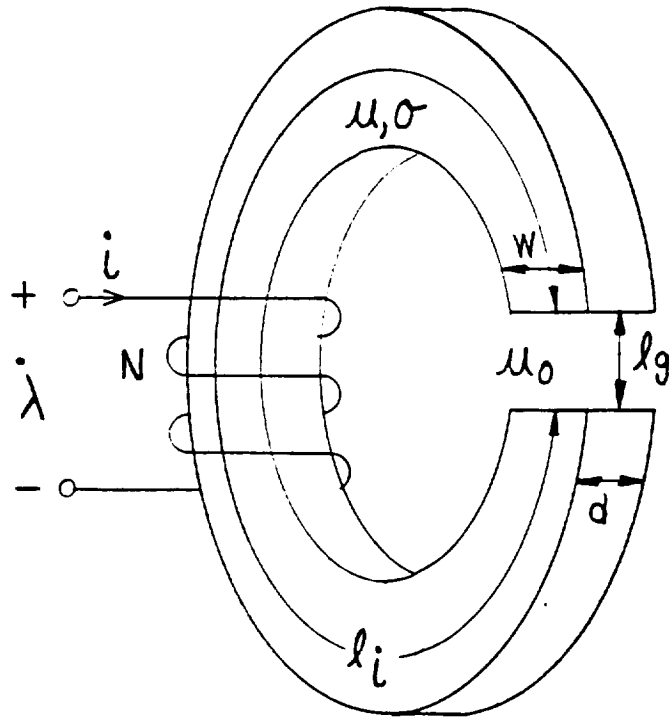


Figure B-1. Toroid and Cross-Section

- (4) The cross-section is rectangular and the fields are symmetric about both axes (z and y).
- (5) The boundary condition along the perimeter of the rectangle is one of uniform flux density.
- (6) Sinusoidal steady state, meaning all excitations and fields can be written as the real part of a complex quantity times  $e^{j\omega t}$ . In particular, the flux density is written as:

$$B(y,z) = i_x \operatorname{Re} \{ B(y,z) e^{j\omega t} \} \quad (\text{B.03})$$

- (7) There is no motion.

### B.1.2 Flux Density

For the remainder of the analysis, the line under complex quantities will be omitted. With the above conditions, the flux density satisfies the two-dimensional diffusion equation:

$$\frac{\partial^2 B}{\partial y^2} + \frac{\partial^2 B}{\partial z^2} = j\omega\mu\sigma B \quad (\text{B.04})$$

Using the method of separation of variables, the flux density can be written as:

$$B = Y(y)Z(z) \quad (\text{B.05})$$

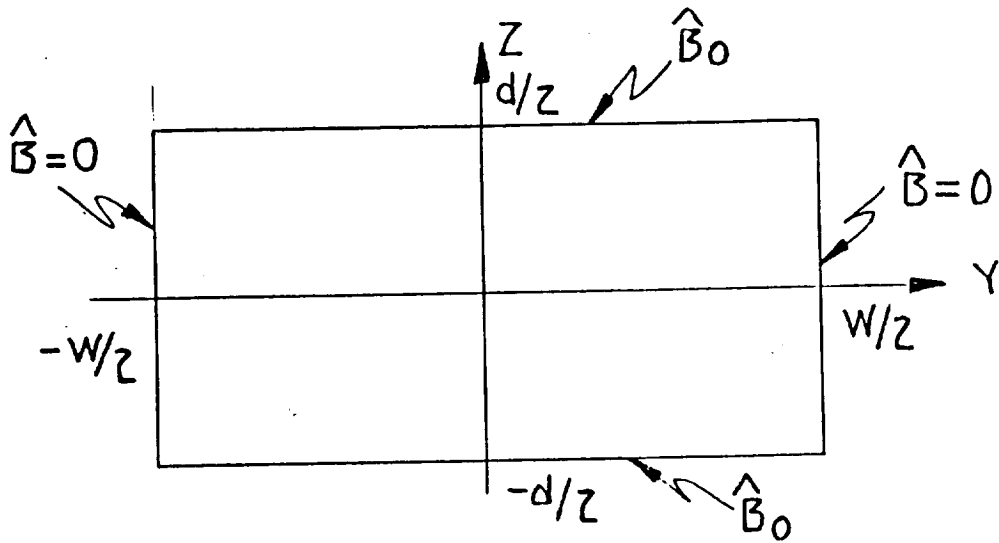
Substituting Equation B.05 into Equation B.04 yields the following.

$$\frac{Y_{yy}}{Y} + \frac{Z_{zz}}{Z} = j\omega\mu\sigma \quad (\text{B.06})$$

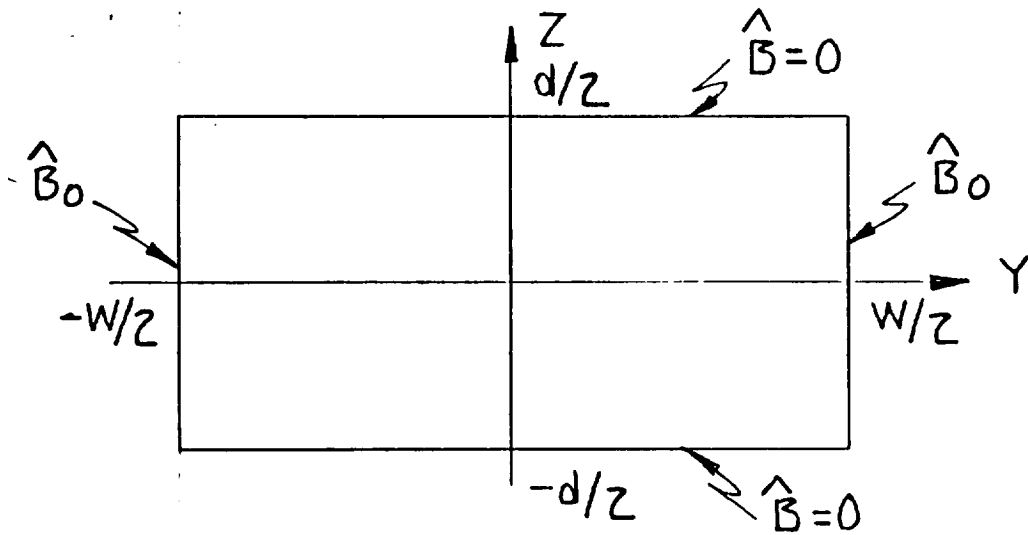
Equation B.06 is true for all y and z only if each term on the left is equal to a constant.

The problem can now be split into two similar problems, each with homogeneous conditions on two of the boundaries and a constant uniform field on the other two boundaries as shown in Figure B.2. For example, with homogeneous conditions on the two boundaries parallel to the z-axis, the constants are chosen to be:

$$\begin{aligned} Y_{yy} &= -k_y^2 Y \\ Z_{zz} &= k_z^2 Z \end{aligned} \quad (\text{B.07})$$



(a) Zero Boundary Conditions Parallel to Z-axis



(b) Zero Boundary Conditions Parallel to Y-axis

**Figure B-2. Boundary Conditions**

A negative sign is used in front of  $k_y$  because cosines will satisfy the  $y$ -related boundary conditions. Due to the symmetry of the problem, hyperbolic cosines are appropriate for the  $z$ -dependent solution.  $Y$  and  $Z$  then satisfy:

$$\begin{aligned} Y &= Y_n = A_n \cos(k_{yn}Y) \\ Z &= Z_n = B_n \cosh(k_{zn}z) \end{aligned} \quad (\text{B.08})$$

where:

$$k_y = k_{yn} = \frac{(2n+1)\pi}{W} \quad n = 1, 2, 3, \dots \quad (\text{B.09})$$

In order to satisfy the other two boundary conditions, a series solution must be used:

$$B_1 = \sum_{n=0}^{\infty} a_n \cos\left[(2n+1)\left(\frac{\pi Y}{W}\right)\right] \cosh(k_{zn}z) \quad n = 0, 1, 2, \dots \quad (\text{B.10})$$

where  $k_{zn}$  is a wave number which will later be determined by plugging the total solution back into the original Equation B.04. The  $a_n$ 's are found in the standard way - using the boundary conditions and the orthogonality of cosines:

$$a_n = B_0 \frac{4}{\pi} \frac{(-1)^n}{(2n+1) \cosh\left(\frac{k_{zn}d}{2}\right)} \quad (\text{B.11})$$

The second problem has a similar solution, with  $y$  and  $z$  interchanged and  $k_{yn}$  and  $k_{zn}$  interchanged. The total solution is then found by superposition of the two solutions.

$$\begin{aligned} B &= B_0 \frac{4}{\pi} \sum_{n=0}^{\infty} \frac{(-1)^n}{(2n+1)} \left[ \cos\left[(2n+1)\left(\frac{\pi Y}{W}\right)\right] \frac{\cosh(k_{zn}z)}{\cosh\left(\frac{k_{zn}d}{2}\right)} \right. \\ &\quad \left. + \cos\left[(2n+1)\left(\frac{\pi Z}{d}\right)\right] \frac{\cosh(k_{yn}Y)}{\cosh\left(\frac{k_{yn}W}{2}\right)} \right] \end{aligned} \quad (\text{B.12})$$

$k_{zn}$  and  $k_{yn}$  are found by substituting Equation B.12 into Equation B.04:

$$k_{zn}^2 = j\omega\mu\sigma + \left[ (2n+1) \frac{\pi}{w} \right]^2 \quad (B.13)$$

$$k_{yn}^2 = j\omega\mu\sigma + \left[ (2n+1) \frac{\pi}{d} \right]^2$$

### B.1.3 Flux

The flux through the metal is found by integrating the flux density over the cross-sectional area of the toroid. The flux ( $\Phi_m$ ) can be expressed as the product of the uniform surface flux density ( $B_o$ ) and a frequency-dependent expression that will be defined as the effective area. The flux can now be visualized as a constant flux density ( $B_o$ ) penetrating a frequency varying area. As the frequency increases, the effective penetration area shrinks while the flux density remains the same.

$$\Phi_m(\omega) = B_o A_m(\omega) \quad (B.14)$$

$$A_m(\omega) = A_o \left( \frac{4}{\pi} \right)^2 \sum_{n=0}^{\infty} \frac{1}{(2n+1)^2} \left[ \frac{\frac{\tanh(k_{zn}d)}{2}}{k_{zn}d} + \frac{\tanh\left(\frac{k_{yn}W}{2}\right)}{k_{yn}W} \right] \quad (B.15)$$

$$A_m(\omega) \equiv A_o f(\omega)$$

where

$$A_o = \text{toroid cross-sectional area} \\ = Wd$$

As expected, in the dc limit the effective area approaches the actual toroid cross-sectional area.

### B.1.4 Electrical Circuit Model

The strategy is to define a frequency-dependent effective area. By expressing the flux through the metal as a constant flux density times a frequency-varying area, rather than a constant area times a frequency-varying flux density, it is now a simple matter to derive equivalent permeances.

The flux through the metal ( $\Phi_g(\omega)$ ) must equal the flux through the air gap ( $\Phi_g(\omega)$ ):

$$\Phi(\omega) = \Phi_m(\omega) = B_o A_m(\omega) = \Phi_g(\omega) = B_g(\omega) A_g \quad (B.16)$$

where

$A_g$  = air-gap area  
=  $A_o$  (for the toroid)  
 $B_g$  = air-gap flux density

Using Ampere's law along a path through the iron and air gap:

$$Ni = H_m l_c + H_g l_g = \frac{B_o}{\mu} l_c + \frac{B_g(\omega)}{\mu_o} l_g \quad (\text{B.17})$$

Combining Equations B.16 and B.17:

$$Ni = \Phi(\omega) \left[ \frac{l_c}{\mu A_m(\omega)} + \frac{l_g}{\mu_o A_g} \right] \quad (\text{B.18})$$

The form of Equation B.18 implies a gap permeance in parallel with an iron permeance, as shown in Figure B.3. The permeances are:

$$\begin{aligned} P_g &= \frac{\mu_o A_g}{l_g} \\ P_m(\omega) &= P_{m0} f(\omega) \\ P_{m0} &= \frac{\mu A_o}{l_c} \end{aligned} \quad (\text{B.19})$$

The terminal voltage (V) is the sum of the voltage drop across the dc resistor (R) and the time derivative of the total flux through the windings ( $\lambda$ ):

$$V = iR + j\omega N\Phi(\omega) = iR + j\omega(L_m//L_g) i \quad (\text{B.20})$$

where // means "in parallel with". The inductances of the metal ( $L_m$ ) and the gap ( $L_g$ ) are  $N^2$  times the respective permeance.

Equation B.20 can be cast in the form of an electrical circuit, but before doing so the circuit will be further refined by splitting the complex metal inductor ( $L_m$ ) into a purely real iron inductor ( $L_i$ ) in parallel with a purely real eddy current induced resistor ( $r_i$ ):

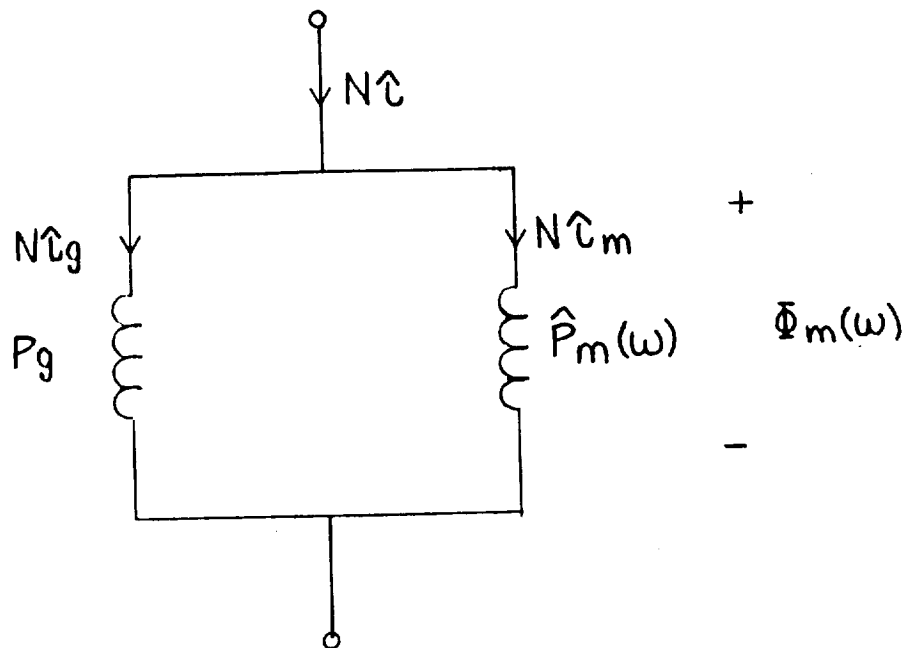


Figure B-3. Equivalent Permeances

$$L_i(\omega) = L_{m0} \frac{|\hat{f}|^2}{\hat{f}_R}$$

$$r_i(\omega) = -\omega L_{m0} \frac{|\hat{f}|^2}{\hat{f}_I} \quad (\text{B.21})$$

$$L_{m0} = N^2 P_{m0} = N^2 \frac{\mu A_0}{l_c}$$

where  $|\hat{f}|$  means "magnitude of" and  $f_R$  and  $f_I$  are the real and imaginary parts of  $f$ , respectively.  $L_{m0}$  is the inductance of the iron in the absence of eddy current effects. The equivalent circuit is shown in Figure B.4. The gap inductor is constant; the iron inductor and resistor are frequency dependent.

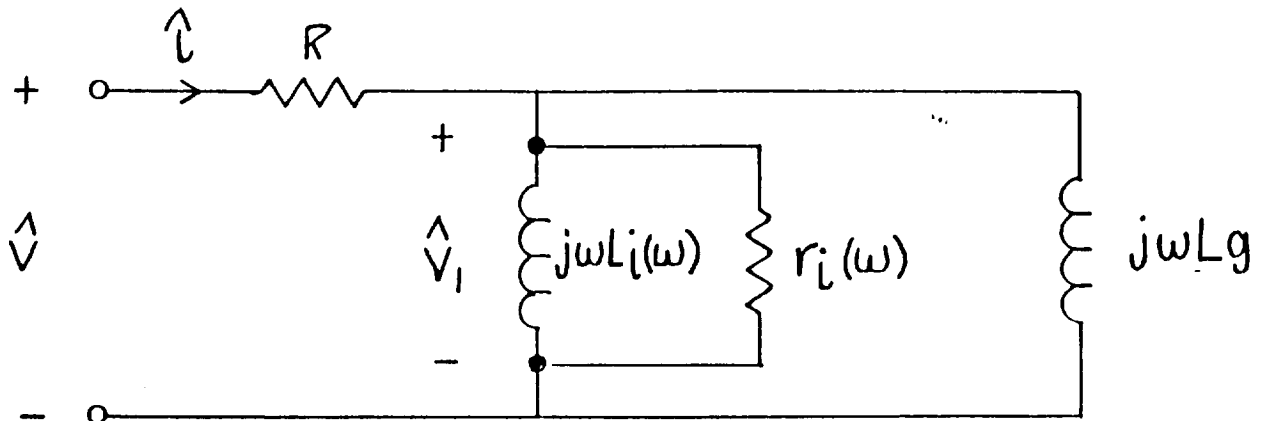


Figure B-4. Equivalent Circuit

#### B.1.5 Power Dissipation Caused by Eddy Currents

The equivalent circuit of Figure B.4 provides a straightforward method for calculating the time average power dissipated by eddy currents; it is simply the square of the voltage drop across  $r_i$ , divided by  $r_i$ :

$$\langle P_{\text{diss}} \rangle_t = \frac{1}{2} \frac{|\hat{V}_1|^2}{r_i} \quad (\text{B.22})$$

The  $1/2$  results from taking the time average of complex quantities.

The power can be normalized by the dc resistance ( $R$ , an unknown quantity) by dividing by the dc power:

$$\frac{\langle P_{\text{diss}} \rangle_t}{P_{\text{dc}}} = \frac{1}{2} \left( \frac{|\hat{V}|^2}{V_{\text{dc}}^2} \right) \frac{\left( \frac{\omega}{\omega_c} \right) (-f_T) L_g (L_{\text{no}} + L_g)}{\left| (f L_{\text{no}} + L_g) + j \left( \frac{\omega}{\omega_c} \right) f (L_{\text{no}} + L_g) \right|^2} \quad (\text{B.23})$$

$V_{\text{dc}}$  is the dc voltage, a known quantity, and  $\omega_c$  is the coil break frequency, also a known quantity:

$$\omega_c = \frac{R}{L_0} \quad (\text{B.24})$$

$$L_0 = L_{\text{to}} // L_g$$

## B.2 Extension to Magnetic Bearing

To apply the above analysis to the magnetic bearing, the same assumptions listed in Section B.1.1 must be made.

- (1) The flux density has only a single component and varies only in the directions orthogonal to that direction.
- (2) The flux density is symmetric about the center line of the magnetic circuit. This implies that flux densities at surfaces equidistant from the center line are equal.
- (3) The flux density is uniform along the boundary of the rectangle. This assumption has shortcomings similar to the last.
- (4) There is no motion. This assumption is valid at relatively low rotational speed and at high closed-loop bandwidth.

The inductances are found in the same manner they were found for the toroid - using Ampere's law along the center line of the magnetic circuit which has a path length ( $l_c$ ). The flux in the metal is assumed equal to the flux in the gap (no leakage). The inductances are:

$$L_g = \frac{1}{2} \frac{(2N)^2 \mu_0 A_g}{l_g}$$

$$L_{\text{to}} = \frac{(2N)^2 \mu A_0}{l_c} \quad (\text{B.25})$$

$$L_{\text{to}} = L_{\text{to}} f(\omega)$$

The path length through the iron was taken to be the sum of the axial paths through the rotor and stator and the radial paths through the poles.

## APPENDIX C

### Collision Modelling

The following is a derivation relating conditions just before a collision to conditions immediately after a collision.

In the following derivation

$M_s$	Mass of the slide
$J_x$	Moment of Inertia of the slide
$J_y$	Moment of Inertia of the slide
$J_z$	Moment of Inertia of the slide
$M_f$	Mass of the frame
$\dot{X}_{fo}$	Initial frame velocity in the X direction
$\dot{Z}_{fo}$	Initial frame velocity in the Z direction
$\dot{X}_{so}$	Initial slide velocity in the X direction
$\dot{Z}_{so}$	Initial slide velocity in the Z direction
$\dot{\theta}_{xo}$	Initial slide velocity in the $\theta_x$ direction
$\dot{\theta}_{yo}$	Initial slide velocity in the $\theta_y$ direction
$\dot{\theta}_{zo}$	Initial slide velocity in the $\theta_z$ direction
$\Delta\dot{X}_f$	Change in the frame velocity
$\Delta\dot{Z}_f$	Change in the frame velocity
$\Delta\dot{X}_s$	Change in the slide velocity
$\Delta\dot{Z}_s$	Change in the slide velocity
$\Delta\dot{\theta}_x$	Change in the slide velocity
$\Delta\dot{\theta}_y$	Change in the slide velocity
$\Delta\dot{\theta}_z$	Change in the slide velocity

Considering a collision along the Z axis, and assuming an elastic collision conserving both energy and linear/angular momentum, the following can be stated

$$\begin{aligned} \frac{1}{2}M_s*(\dot{Z}_{so})^2 + \frac{1}{2}J_x*(\dot{\theta}_{xo})^2 + \frac{1}{2}J_y*(\dot{\theta}_{yo})^2 & \quad \text{Eq.} \\ & = \frac{1}{2}M_s*(\dot{Z}_{so} + \Delta\dot{Z}_s)^2 + \frac{1}{2}M_f*(\dot{Z}_{fo} + \Delta\dot{Z}_f)^2 & \text{(C.1)} \end{aligned}$$

$$\begin{aligned} \frac{1}{2}M_s*(\dot{Z}_{so})^2 + \frac{1}{2}M_f*(\dot{Z}_{fo}) + \frac{1}{2}J_x*(\dot{\theta}_{xo})^2 + \frac{1}{2}J_y*(\dot{\theta}_{yo})^2 & \\ & = \frac{1}{2}M_s*(\dot{Z}_{so} + \Delta\dot{Z}_s)^2 + \frac{1}{2}M_f*(\dot{Z}_{fo} + \Delta\dot{Z}_f)^2 & \text{Eq.} \\ & + \frac{1}{2}J_x*(\dot{\theta}_{xo} + \Delta\dot{\theta}_x)^2 + \frac{1}{2}J_y*(\dot{\theta}_{yo} + \Delta\dot{\theta}_y)^2 & \text{(C.2)} \end{aligned}$$

$$Ms*(\dot{Z}_{s0}) + Mf*(\dot{Z}_{f0}) = Ms*(\dot{Z}_{s0} + \Delta\dot{Z}_s) + Mf*(\dot{Z}_{f0} + \Delta\dot{Z}_f) \quad \text{Eq. (C.3)}$$

$$Jx*(\dot{\theta}_{x0}) + Ly*Mf*(\dot{Z}_{f0}) = Jx*(\dot{\theta}_{x0} + \Delta\dot{\theta}_x) + Ly*Mf*(\dot{Z}_{f0} + \Delta\dot{Z}_f) \quad \text{Eq. (C.4)}$$

$$Jy*(\dot{\theta}_{y0}) - Lx*Mf*(\dot{Z}_{f0}) = Jy*(\dot{\theta}_{y0} + \Delta\dot{\theta}_y) - Lx*Mf*(\dot{Z}_{f0} + \Delta\dot{Z}_f) \quad \text{Eq. (C.5)}$$

The body axis of the slide at its mass center is taken as the point of reference to calculate the moments. Lx and Ly are the coordinates of the point of collision with respect to this reference and the moments of inertia of the point mass Mf are, as a consequence, (Lx)<sup>2</sup>\*Mf and (Ly)<sup>2</sup>\*Mf around the y and x axis respectively.

From Eq. (C.3 to C.5) we have

$$\Delta\dot{Z}_f = -\left(\frac{Ms}{Mf}\right) \Delta\dot{Z}_s$$

$$\Delta\dot{\theta}_x = Ly\left(\frac{Ms}{Jx}\right) \Delta\dot{Z}_s \quad \text{Eq. (C.6)}$$

$$\Delta\dot{\theta}_y = -Lx\left(\frac{Ms}{Jy}\right) \Delta\dot{Z}_s$$

Expanding Eq. (C.2) and canceling common terms

$$Ms*(\Delta\dot{Z}_s^2 + 2*\dot{Z}_{s0}*\Delta\dot{Z}_s) + Mf*(\Delta\dot{Z}_f^2 + 2*\dot{Z}_{f0}*\Delta\dot{Z}_f) + Jx*(\Delta\dot{\theta}_x^2 + 2*\dot{\theta}_{x0}*\Delta\dot{\theta}_x) + Jy*(\Delta\dot{\theta}_y^2 + 2*\dot{\theta}_{y0}*\Delta\dot{\theta}_y) = 0.0 \quad \text{Eq. (C.7)}$$

Substituting from Eq. (C.6) for  $\Delta\dot{Z}_f$ ,  $\Delta\dot{\theta}_x$  and  $\Delta\dot{\theta}_y$

$$Ms*(\Delta\dot{Z}_s^2 + 2*\dot{Z}_{s0}*\Delta\dot{Z}_s) + Mf*(Ms^2/Mf^2*\Delta\dot{Z}_s^2 - 2*\dot{Z}_{f0}*Ms/Mf*\Delta\dot{Z}_s) + Jx*(Ly^2*Ms^2/Jx^2*\Delta\dot{Z}_s^2 + 2*\dot{\theta}_{x0}*Ly*Ms/Jx*\Delta\dot{Z}_s) + Jy*(Lx^2*Ms^2/Jy^2*\Delta\dot{Z}_s^2 - 2*\dot{\theta}_{y0}*Lx*Ms/Jy*\Delta\dot{Z}_s) = 0.0 \quad \text{Eq. (C.8)}$$

Canceling out the  $\Delta\dot{Z}_s$ , Ms

$$(\Delta\dot{Z}_s + 2*\dot{Z}_{s0}) + (Ms/Mf*\Delta\dot{Z}_s - 2*\dot{Z}_{f0}) + (Ly^2*Ms/Jx*\Delta\dot{Z}_s + 2*\dot{\theta}_{x0}*Ly) + (Lx^2*Ms/Jy*\Delta\dot{Z}_s - 2*\dot{\theta}_{y0}*Lx) = 0.0$$

$$\Delta\dot{Z}_s*(1.0 + Ms/Mf + Ly^2*Ms/Jx + Lx^2*Ms/Jy) = -(2*\dot{Z}_{s0} - 2*\dot{Z}_{f0} + 2*\dot{\theta}_{x0}*Ly - 2*\dot{\theta}_{y0}*Lx)$$

$$\Delta \dot{Z}_s = \frac{(2*\dot{Z}_{s0} - 2*\dot{Z}_{f0} + 2*\theta_{x0}*Ly - 2*\theta_{y0}*Lx)}{(1.0 + \frac{Ms}{Mf} + Ly^2*\frac{Ms}{Jx} + Lx^2*\frac{Ms}{Jy})} \quad \text{Eq. (C.9)}$$

The term Ms/Mf can be neglected if Mf >> Ms  
Substituting into Eq. (C.6)

$$\Delta \theta_x = \frac{-Ly*\frac{Ms}{Jx}*(2*\dot{Z}_{s0} - 2*\dot{Z}_{f0} + 2*\theta_{x0}*Ly - 2*\theta_{y0}*Lx)}{(1.0 + \frac{Ms}{Mf} + Ly^2*\frac{Ms}{Jx} + Lx^2*\frac{Ms}{Jy})} \quad \text{Eq. (C.10)}$$

$$\Delta \theta_y = \frac{Lx*\frac{Ms}{Jy}*(2*\dot{Z}_{s0} - 2*\dot{Z}_{f0} + 2*\theta_{x0}*Ly - 2*\theta_{y0}*Lx)}{46}$$

$$(1.0 + \frac{Ms}{Mf} + Ly^2*\frac{Ms}{Jx} + Lx^2*\frac{Ms}{Jy}) \quad \text{Eq. (C.11)}$$

Considering a collision along the X axis, and assuming an elastic collision conserving both energy and linear/angular momentum, the following can be stated

$$\begin{aligned} \frac{1}{2}Ms*(X_{s0})^2 + \frac{1}{2}Mf*(X_{f0})^2 + \frac{1}{s}Jz*(\theta_{z0})^2 + \frac{1}{2}Jy*(\theta_{y0})^2 \\ = \frac{1}{2}Ms*(X_{s0} + \Delta X_s)^2 + \frac{1}{2}Mf*(X_{f0} + \Delta X_f)^2 \\ + \frac{1}{2}Jz*(\theta_{z0} + \Delta \theta_z)^2 + \frac{1}{2}Jy*(\theta_{y0} + \Delta \theta_y)^2 \end{aligned} \quad \text{Eq. (C.12)}$$

$$Ms*(X_{s0}) + Mf*(X_{f0}) = Ms*(X_{s0} + \Delta X_s) + Mf*(X_{f0} + \Delta X_f) \quad \text{Eq. (C.13)}$$

$$Jz*(\dot{\theta}_{z0}) - Ly*Mf*(X_{f0}) = Jz*(\dot{\theta}_{z0} + \Delta \dot{\theta}_z) - Ly*Mf*(X_{f0} + \Delta X_f) \quad \text{Eq. (C.14)}$$

$$Jy*(\dot{\theta}_{y0}) + Lz*Mf*(X_{f0}) = Jy*(\dot{\theta}_{y0} + \Delta \dot{\theta}_y) + Lz*Mf*(X_{f0} + \Delta X_f) \quad \text{Eq. (C.15)}$$

The body axis of the slide at its mass center is taken as the point of reference to calculate the moments. Lz and Ly are the coordinates of the point of collision with respect to this

reference and the moments of inertia of the point mass  $M_f$  are, as a consequence,  $(L_z)^2 * M_f$  and  $(L_y)^2 * M_f$  around the y and x axis respectively.

From Eq. (C.13 to 15) we have

$$\Delta X_f = - M_s / M_f * \Delta X_s \quad \text{Eq. (C.16)}$$

$$\Delta \dot{\theta}_z = - L_y * M_s / J_y * \Delta X_s \quad \text{Eq. (C.17)}$$

$$\Delta \dot{\theta}_y = L_z * M_s / J_z * \Delta X_s \quad \text{Eq. (C.18)}$$

Expanding Eq. (C.12) and canceling common terms

$$\begin{aligned} M_s * (\Delta X_s^2 + 2 * X_{s0} * \Delta X_s) + M_f * (\Delta X_f^2 + 2 * X_{f0} * \Delta X_f) \\ + J_z * (\Delta \dot{\theta}_z^2 + 2 * \dot{\theta}_{z0} * \Delta \dot{\theta}_z) + J_y * (\Delta \dot{\theta}_y^2 + 2 * \dot{\theta}_{y0} * \Delta \dot{\theta}_y) = 0.0 \end{aligned} \quad \text{Eq. (C.19)}$$

Substituting from Eq. (C.16-18) for  $\Delta X_f$ ,  $\Delta \dot{\theta}_z$  and  $\Delta \dot{\theta}_y$

$$\begin{aligned} M_s * (\Delta X_s^2 + 2 * X_{s0} * \Delta X_s) + M_f * (M_s^2 / M_f^2 * \Delta X_s^2 - 2 * X_{f0} * M_s / M_f * \Delta X_s) \\ + J_z * (L_y^2 * M_s^2 / J_z^2 * \Delta X_s^2 - 2 * \dot{\theta}_{z0} * L_y * M_s / J_z * \Delta X_s) \\ + J_y * (L_z^2 * M_s^2 / J_y^2 * \Delta X_s^2 + 2 * \dot{\theta}_{y0} * L_z * M_s / J_y * \Delta X_s) = 0.0 \end{aligned} \quad \text{Eq. (C.20)}$$

Canceling out the  $\Delta X_s$ ,  $M_s$

$$\begin{aligned} (\Delta X_s + 2 * X_{s0}) + (M_s / M_f * \Delta X_s - 2 * X_{f0}) + (L_y^2 * M_s / J_z * \Delta X_s - 2 * \dot{\theta}_{z0} * L_y) \\ + (L_z^2 * M_s / J_y * \Delta X_s + 2 * \dot{\theta}_{y0} * L_z) = 0.0 \end{aligned}$$

$$\begin{aligned} \Delta X_s * (1.0 + M_s / M_f + L_y^2 * M_s / J_z + L_z^2 * M_s / J_y) \\ = -(2 * X_{s0} - 2 * X_{f0} - 2 * \dot{\theta}_{z0} * L_y + 2 * \dot{\theta}_{y0} * L_z) \end{aligned}$$

$$\Delta X_s = \frac{-(2 * X_{s0} - 2 * X_{f0} - 2 * \dot{\theta}_{z0} * L_y + 2 * \dot{\theta}_{y0} * L_z)}{(1.0 + \frac{M_s}{M_f} + L_y^2 * \frac{M_s}{J_z} + L_z^2 * \frac{M_s}{J_y})} \quad \text{Eq. (C.21)}$$

The term  $M_s / M_f$  can be neglected if  $M_f \gg M_s$   
Substituting into Eq. (C.17) and (C.18)

$$\Delta\theta_x = \frac{-Ly * \frac{Ms}{Jx} * (2 * \dot{z}_{s0} - 2 * \dot{z}_{f0} + 2 * \theta_{x0} * Ly - 2 * \theta_{y0} * Lx)}{(1.0 + \frac{Ms}{Mf} + Ly^2 * \frac{Ms}{Jx} + Lx^2 * \frac{Ms}{Jy})} \quad \text{Eq. (C.22)}$$

$$\Delta\theta_y = \frac{Lx * \frac{Ms}{Jy} * (2 * \dot{z}_{s0} - 2 * \dot{z}_{f0} + 2 * \theta_{x0} * Ly - 2 * \theta_{y0} * Lx)}{(1.0 + \frac{Ms}{Mf} + Ly^2 * \frac{Ms}{Jx} + Lx^2 * \frac{Ms}{Jy})} \quad \text{Eq. (C.23)}$$

These equations are used in the dynamic simulation to model collisions. The equations have been extended to allow for collisions along the edges of the bearing slide.

## REFERENCES

1. Hockney, R., and Hawkey, T. Magnetic Bearings for an Optical-Disk Buffer, SBIR Phase I Final Report. SatCon Technology Corp., R08-87, September 1987.
2. Summary Report, Task 7-1 Free-Travel Budget. GE Aerospace, RCA Government Communications Systems Division (letter). August 1989.
3. Eds. Baumeister, T., Avallone, E., Baumeister III, T. Mark's Standard Handbook for Mechanical Engineers, Eighth Edition, McGraw-Hill Book Co., 1978.
4. Materials Selector 1986, "Materials Engineering." Penton/IPC (Publ.) 1985, p. 144.



# Report Documentation Page

1. Report No.		2. Government Accession No.		3. Recipient's Catalog No.	
4. Title and Subtitle  Magnetic Bearings for a High-Performance Optical Disk Buffer				5. Report Date  May 1990	
				6. Performing Organization Code	
7. Author(s)  Richard Hockney, George Anastas, Jr., James Downer, Frederick Flynn, James Goldie, Vijay Gondhalekar, Bruce Johnson, Timothy Hawkey				8. Performing Organization Report No.  R05-90	
				10. Work Unit No.	
9. Performing Organization Name and Address  SatCon Technology Corporation 12 Emily Street Cambridge, MA 02139-4507				11. Contract or Grant No.  NAS5-30309	
				13. Type of Report and Period Covered  Final 5/88 - 2/90	
12. Sponsoring Agency Name and Address  National Aeronautics and Space Administration Washington, DC 20546-0001  Goddard Space Flight Center Greenbelt, MD 20771				14. Sponsoring Agency Code	
				15. Supplementary Notes	
16. Abstract <p>The innovation investigated in this project was the application of magnetic bearing technology to the translator head of an optical-disk data storage device. Both the capability for space-based applications and improved performance are expected to result. The principal objective of Phase II was the design, fabrication, assembly, and test of the magnetic bearing system for the translator head. The scope of work included: (1) mechanical design of each of the required components, (2) electrical design of the required circuitry, (3) fabrication of the component parts and bread-board electronics, (4) generation of a test plan, and (5) integration of the prototype unit and performance testing.</p> <p>The project has confirmed the applicability of magnetic bearing technology to suspension of the translator head of the optical disk device, and demonstrated the achievement of all performance objectives. The magnetic bearing control loops perform well, achieving 100 Hz nominal bandwidth with phase margins between 37 and 63 degrees. The worst-case position resolution is 0.02 <math>\mu</math> in the displacement loops and 1 <math>\mu</math>Rad in the rotation loops. The system is very robust to shock disturbances, recovering smoothly even when collisions occur between the translator and frame. The unique start-up/shut-down circuit has also proven very effective.</p>					
17. Key Words (Suggested by Author(s))  Magnetic bearings Optical data storage Data buffer			18. Distribution Statement  See attached SBIR Rights notice.		
19. Security Classif. (of this report)  Unclassified		20. Security Classif. (of this page)  Unclassified		21. No. of pages  184	22. Price

